

Role of interlayer and interfacial electric field generated during simultaneous HER and OER over Li intercalated $g - C_3N_4$ for efficient photocatalytic activity

Brajesh Rajesh Bhagat, Alpa Dashora *

Department of Physics, Faculty of Science, The Maharaja Sayajirao University of Baroda, Sayajigunj, Vadodara, 390002, Gujarat, India

ARTICLE INFO

Keywords:

Photocatalysis
Interlayer charge transfer
Density functional theory

ABSTRACT

Substantial variation in the photocatalytic activity on the interaction of reaction intermediates with the surface of the catalyst is governed by the charge transfer mechanism. Charge transfer within a stacked layer of photocatalyst and across the reactant-photocatalyst interface alters photocatalytic activity due to the generation of an electric field. This work addresses the synergistic effect of interlayer (\vec{E}_{il}) and interfacial (\vec{E}_{if}) electric field on the photocatalytic activity of Li-intercalated $g - C_3N_4$ (Li – CN) through the study of electronic and optical properties using density functional theory. Charge transfer analysis for simultaneous oxygen evolution reaction (OER) and hydrogen evolution reaction (HER) in the presence of two water molecules shows variation in built-in \vec{E}_{il} of Li – CN as the surface reaction proceeds via the induced \vec{E}_{if} generated by the reactants on Li – CN. This change in \vec{E}_{il} alters the energy barrier of the next reaction step through directional charge transfer. The present study reveals the mutual interplay of \vec{E}_{il} , \vec{E}_{if} and adsorption energy of reaction adsorbates for improved photocatalytic activity of Li – CN for efficient OER and HER.

1. Introduction

Establishing and strengthening interlayer van der Waals (VDW) interaction between chemically inert layers of photocatalyst promotes photo-generated charge carriers migration and reduces recombination rate [1]. Formation of the bilayer involving interlayer orbital overlap [2], intercalation of alkali/alkaline earth metals for directional charge delivery, and formation of heterostructures following s/z-scheme [3] of electron transfer have been adopted for efficient photocatalyst design [4,5]. Charge separation, mobility enhancement, the larger lifetime of photogenerated charge carrier, and reduction of their recombination have been achieved by variety of functionalization techniques. Dong's group has exclusively enhanced the efficiency of graphitic carbon nitride ($g - C_3N_4$) for NO removal via intercalation/decoration of Cs, Rb, K [6,7], K/O [8], Ca [9], Ba [10], and Sr [11] which is governed by vertical electron transfer, established by extending π -conjugation, activating reactants, localizing electron around a metal atom, and formation of reactive oxygen species. On the contrary, Na exhibits shortened lifetime of charge carriers resulting from increased electron concentration in the planar region and suppressed catalytic performance [12].

In search of atom/s capable of bridging stacked layers, Li [4,13,14], Li/Na/K [15], and Li/Cl [16] show significant enhancement in photocatalytic N_2 fixation [17], dye degradation, and H_2 production in the

$g - C_3N_4$ bilayer (BL – CN) assembly, experimentally and theoretically. Li because of its small ionic radii holds the potential to bridge stacked layers without distorting ring geometry of $g - C_3N_4$ [15,16]. Parameters leading to the increased catalytic activity of $g - C_3N_4$ include narrowed band gap (E_g), valence band shift, and varied interlayer spacing for co-intercalation which boosts electron migration between the layers. Substitutional doping [18,19] and adsorption [20,21] of Li over triazine moiety projects the role of Li in increasing electron affinity or reducing work function of $g - C_3N_4$, whereas Li-N interaction governs the electron transfer channel for adsorbent activation. Charge transportation and separation capabilities attributing due to Li's urge for releasing its outer electron which is complimented with enhanced optical absorbance and red shift demonstrate potential photocatalytic suitability of Li associated $g - C_3N_4$.

Potential gradient across stacked layers in K, Rb, and Cs bridged $g - C_3N_4$ induces interlayer electric field (\vec{E}_{il}) which directs electron migration vertically [6,7], this is similar to the \vec{E}_{il} set between heterostructures due to difference in work function (Φ) [3,22]. \vec{E}_{il} across the semiconductor–metal junction and semiconductor–semiconductor junction [23] complemented with band edges alignment controls the charge dynamics [24] within the photocatalyst. Further, to balance the interlayer and intralayer electron distribution, co-doping of S/K- [25], halogen atoms/K- [26], B/K- [27], and Zn/K [28] within $g -$

* Corresponding author.

E-mail address: dashoralpa@gmail.com (A. Dashora).

C_3N_4 have shown enhanced H_2 evolution and CO/CH_4 production. Formation of internal VDW heterostructure (IVDWH) by combining “surface decoration” and “intercalation” showed that O incorporation in K-functionalized $g-C_3N_4$ [8] enhanced charge transfer channel by electron localization around O and strengthening internal VDW interaction leading to spatial separation of photogenerated charge carriers. Whereas, the synergistic effect of interfacial electric field (E_{if}) formed at the reactant-photocatalyst interface and polarizability of interacting molecules regulates the chemical kinetics of reaction/s occurring at the surface of photocatalyst [29–31]. Formation of an electric field at the $\pi-\pi$ conjugated hetero-interface governs the charge migration within the heterostructure of covalent organic framework-TpPa-1 and $g-C_3N_4$ [32], whereas Ag-Pt decorated over defective C_3N_x nanosheets shows decreased peak intensity of XRD at 27.6° and enhanced hydrogen production with an apparent quantum efficiency of 3.3% at 420 nm due to localized surface plasmon resonance effect is seen [33].

In order to understand IVDWH formed by the adsorption of various intermediates adsorbed during the reaction, we have studied the independent oxygen evolution reaction (OER) and hydrogen evolution reaction (HER) using a traditional computational hydrogen electrode (CHE) method [34,35] over Li intercalated $g-C_3N_4$ bilayer (Li-CN) along with electronic and optical properties using density functional theory (DFT). Despite the reported work on the enhancement of certain photocatalytic activity by the inclusion of Li-atom in the $g-C_3N_4$ network, its water-splitting capabilities are yet untouched. A complete theoretical study of the role of Li-intercalation in $g-C_3N_4$ for OER and HER will further explain the existing experimental results and will verify its suitability for photocatalytic activity. To study the interplay and mutual dependence of \vec{E}_{il} and \vec{E}_{if} which is also an unexplored topic since the introduction of homo- and hetero-layered structures along with its importance on tailoring surface properties, we have also computed simultaneous OER and HER in the presence of two water molecules on the surface of Li-CN. $\vec{E}_{il}/\vec{E}_{if}$ formation in Li-CN governs the charge transfer mechanism across the whole reaction which is unraveled and being addressed through step-by-step charge analysis and verified by the study of activation barrier (E_a) which is calculated using nudge elastic band (NEB) approach [36,37].

2. Methodology

2.1. Computational details

An *ab-initio* based DFT calculations [38–40] with in-built Kohn Sham formulation for plane wave-based approach as implemented in the Quantum Espresso Package [41] is considered for structural relaxation and computation of HER and OER reaction study of Li-CN. For the computation, a kinetic energy cut-off of 60 Ry is used along with optimized norm-conserving Vanderbilt pseudopotential (ONCV) [42] for core correction. Grimme-D2 dispersion correction is used to describe VDW interaction. Also to avoid periodic inter-slab interaction along the z -direction, 20 Å of vacuum space is considered. Coulomb interaction in the z -direction was truncated in order to keep the computational parameter similar to our earlier work [2]. All the structures are relaxed with an electronic convergence threshold of 10^{-6} a.u. Maximum force per atom less than 10^{-3} a.u./Å is considered for atomic position relaxation with k point grid of $5 \times 5 \times 2$ using Perdew–Burke–Ernzerhof [43] following generalized gradient approximation (GGA). Electronic properties including electrostatic potential profiles, Löwdin charges, and density of states (DOS) are computed using a self-consistent field cycle. Along with GGA, hybrid functional HSE06 [44,45] for accurate band gap calculation at $3 \times 3 \times 3$ k -point mesh is also considered followed by band structure computation using Maximally Localized Wannier Functions (MLWF) implemented in the Wannier90 package [46–48].

The electronic and optical properties like DOS, partial DOS (PDOS), local DOS (LDOS), band structure, absorption coefficient ($\alpha(\omega)$), and the imaginary part of dielectric function ($\epsilon_2(\omega)$) for BL-CN and Li-CN

have also been carried out using the full potential linearized augmented plane wave (FP-LAPW) method as implemented in WIEN2k code [49]. For a better estimation of the electronic band gap and optical properties, TB-mBJ (Tran-Blaha modified Becke–Johnson) potential [50] has been used. For Li-CN, the muffin-tin radii for carbon, nitrogen, and lithium atoms are 1.18, 1.25, and 1.75 a.u., respectively to produce smooth variation between the core spherical harmonics and interstitial augmented plane waves at the boundaries defined by these radii. For BL-CN, the muffin-tin radii for carbon and nitrogen atoms are 1.22 and 1.29 a.u., respectively. The value of $R_{mt}K_{max}$ was set to be 7.0, here, R_{mt} is the smallest value of the muffin-tin radius, and K_{max} is the largest K for the plane waves used in the calculations. The maximum value of the charge density Fourier expansion (G_{max}) is kept as 12, while the expansion of the wavefunctions was done with the highest value of angular momentum $l_{max} = 10$. All the calculations were performed on a k -mesh grid of $3 \times 3 \times 1$.

2.2. Reaction kinetics

OER and HER studies on 29 atoms Li-CN system is subjected to both conventional [34,35,51] and simultaneous OER and HER (with two water molecules), where respective intermediates were adsorbed and relaxed sequentially for OER whereas HER requires single atom/molecule optimization. For simultaneous OER and HER, two H_2O molecules were relaxed since it is enough for complete simultaneous OER & HER with $\sim 4 \times 10^{14}$ H_2O / cm^2 interacting with the surface. To calculate the activation barrier for each step of simultaneous OER & HER and to study the reaction kinetics, the climbing image-nudged elastic band (CI-NEB) [36,37] method was also utilized. Optimized structures from DFT were used as the initial and final structures in the CI-NEB calculations. CI-NEB calculations converged with a path threshold of 0.05 eV Å⁻¹ with 12 images for all four steps each.

To understand each reaction step and the charge transfer mechanism, from the calculated Löwdin charges, interlayer (ΔQ_{il}) and interfacial (ΔQ_{if}) charge difference is calculated using the following formulas:

$$\Delta Q_{il} = Q_{LL}^{system} - Q_{UL}^{system} \quad (1)$$

$$\Delta Q_{if} = Q_{adsorbate}^{system} - Q_{adsorbate}^{VEC} \quad (2)$$

Here, VEC: Valence electron count; LL: Lower layer; UL: Upper layer

In order to simplify the charge transfer mechanism, instead of tabulating the total charge we have calculated the charge difference, $\Delta Q_{UL/LL} = Q_{UL/LL}^{system} - Q_{UL/LL}^{VEC}$. Since VEC is constant ($Q_{LL/UL}^{VEC} = 64$), on increasing the total charge of system ΔQ will decrease, for example for $Q_{UL/LL}^{Li-CN}$ of 63.5078/63.6386 e^- and $Q_{UL/LL}^{Li-CN-H_2O}$ of 63.208/63.8837 e^- we calculate $|\Delta Q_{UL/LL}^{Li-CN}|$ of 0.4922/0.3614 e^- (Table S1) and $|\Delta Q_{UL/LL}^{Li-CN-H_2O}|$ of 0.792/0.1163 e^- , respectively. The charge of the Li atom and H_2O molecule is not considered for calculations of $\Delta Q_{Li-CN/Li-CN-H_2O}$. Where a decrease (increase) on LL (UL) of $Q_{Li-CN/Li-CN-H_2O}$ leads to an increase (decrease) on LL (UL) of $\Delta Q_{Li-CN/Li-CN-H_2O}$ from pristine to H_2O adsorbed Li-CN as tabulated in Table S2.

OER is a four e^- transfer reaction starting from the H_2O molecule adsorption over the surface. The dipole moment of H_2O [52,53] drives itself towards the most electronegative site leading to weak H-bonding between electropositive (H_2O) and electronegative (substrate) region. The second step involves hydrogen and hydroxyl dissociation leading to hydroxyl drift towards the corresponding e^- donating site. Further deprotonation of hydroxyl leading to $*O$ due to e^- transfer owns the second step of OER. Dissociation of another H_2O into hydrogen and hydroxyl is followed by OH & $*O$ association into $*OOH$ completes the third step reported majorly as the rate-determining step (RDS) [35] due to complex dissociation and association route. Finally, this $*OOH$ after

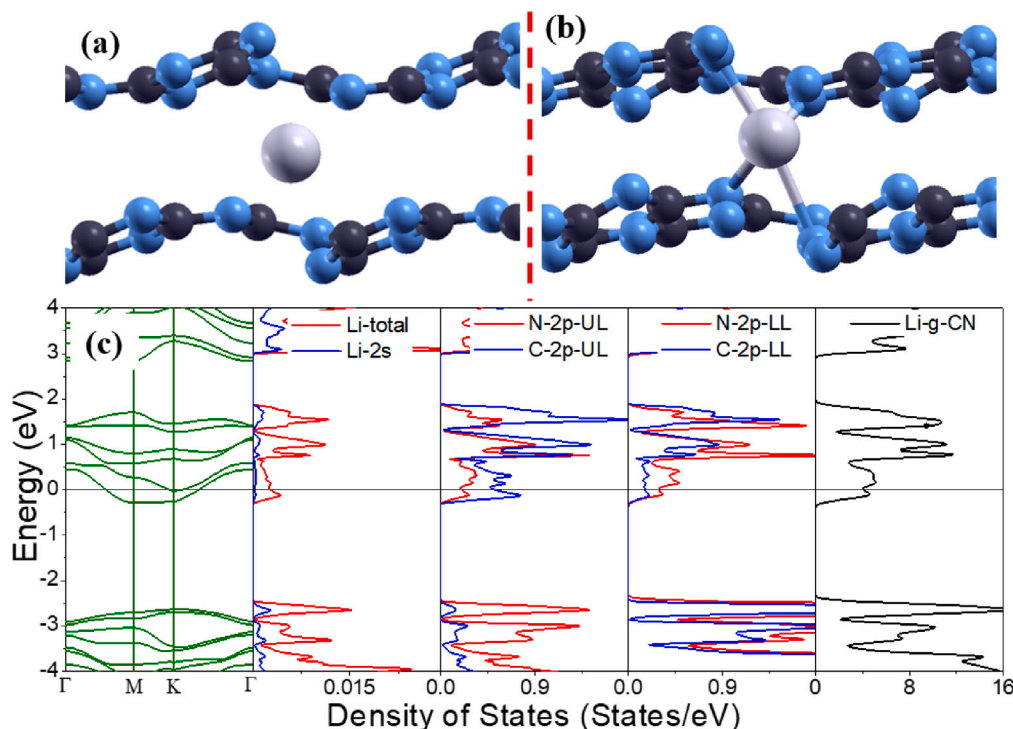
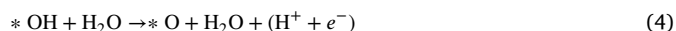
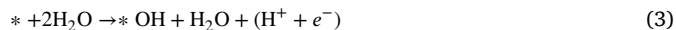


Fig. 1. Side view of (a) initial and, (b) Optimized crystal structure of Li – CN; (c) bands, total, the sum of the partial density of states for all atoms of upper and lower layer for Li – CN, with Fermi energy shifted to zero.

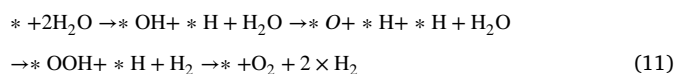
deprotonation leads to oxygen molecule desorption, this method has been followed according to Eqs. (3)–(6).



The hydrogen atom is adsorbed over the surface at a high electronegative region, following the conventional way of calculating ΔG^H using the $\Delta E^{*H/H_2O}$ has been undertaken. The energy barrier required to overcome, for feasible HER is considered to be derived from the $\Delta E^{*H/H_2O}$. The extra water molecule plays two-part roles in understanding the HER: (i) dipole moment of H_2O drives the adsorption of the H atom, and (ii) formation of H bond between surface- H_2O would redistribute the charges over the surface affecting the feasibility of reaction (see Eqs. (7) to (10)).



In order to study simultaneous OER & HER over the surface, adsorption of two H_2O is an initial step and follows Eq. (11) and Fig. 5:



Here, one of the two H_2O will initiate its dissociation leading to OER & HER together with the formation of hydroxyl & hydrogen,

respectively while another will participate in influencing (i) former H_2O , (ii) charge conjugation over the surface, and (iii) create an E_{if} (electric double layer) [54], as catalyst surface interacts with the water layer an electric field at the interface is formed which plays an essential role in modifying reaction kinetics. Hydroxyl/hydrogen will bond to their respective sites for oxidation/reduction, this $* \text{OH}$ will initiate the next step leading into $* \text{O}$ conversion by releasing H. This H now is capable of the formation of H_2 either by the Heyrovsky mechanism, else following the Tafel mechanism it will bond on another electronegative site. Formation of $* \text{O}$, $2* \text{H}$ will be followed by another H_2O dissociation while cyclically third H_2O will take place of the second to maintain the E_{if} . H_2O dissociation as the third step will result in H^+ & OH^- , this hydroxyl leads to $* \text{OOH}$ while third H^+ again can form H_2 through Heyrovsky or Tafel (if Heyrovsky did not take place in the previous step). After successful H_2 desorption the surface is left with $* \text{OOH}$ and $* \text{H}$, leading to another H_2 , and O_2 desorption completes the whole reaction.

The reasons behind simultaneous HER and OER simulation with two water molecules are (i) to investigate the charge transfer during the whole reaction as the number of atoms will remain same unlike, conventional OER/HER, (ii) to understand the effect of surface terminations within the process on the respective reaction, and (iii) the effect of adsorbate–adsorbent charge transfer and the effect of H_2O in the generation of an electric field across the junction.

3. Results and discussion

3.1. Electronic and optical properties

Structural variation is the depiction of the change in electronic properties, here Li intercalation in BL – CN further corrugates the initial structure. As seen from Fig. 1(a–b) Li atom initially positioned at the center of BL – CN interacts with N^{edge} [2] atoms of the upper and lower layer (UL and LL) with bond lengths of 2.01, 2.28, 2.14, and 2.58 Å as shown in Fig. 3(a). This bilayer bridging reduces average interlayer separation by 0.286 Å in addition to spatial displacement of

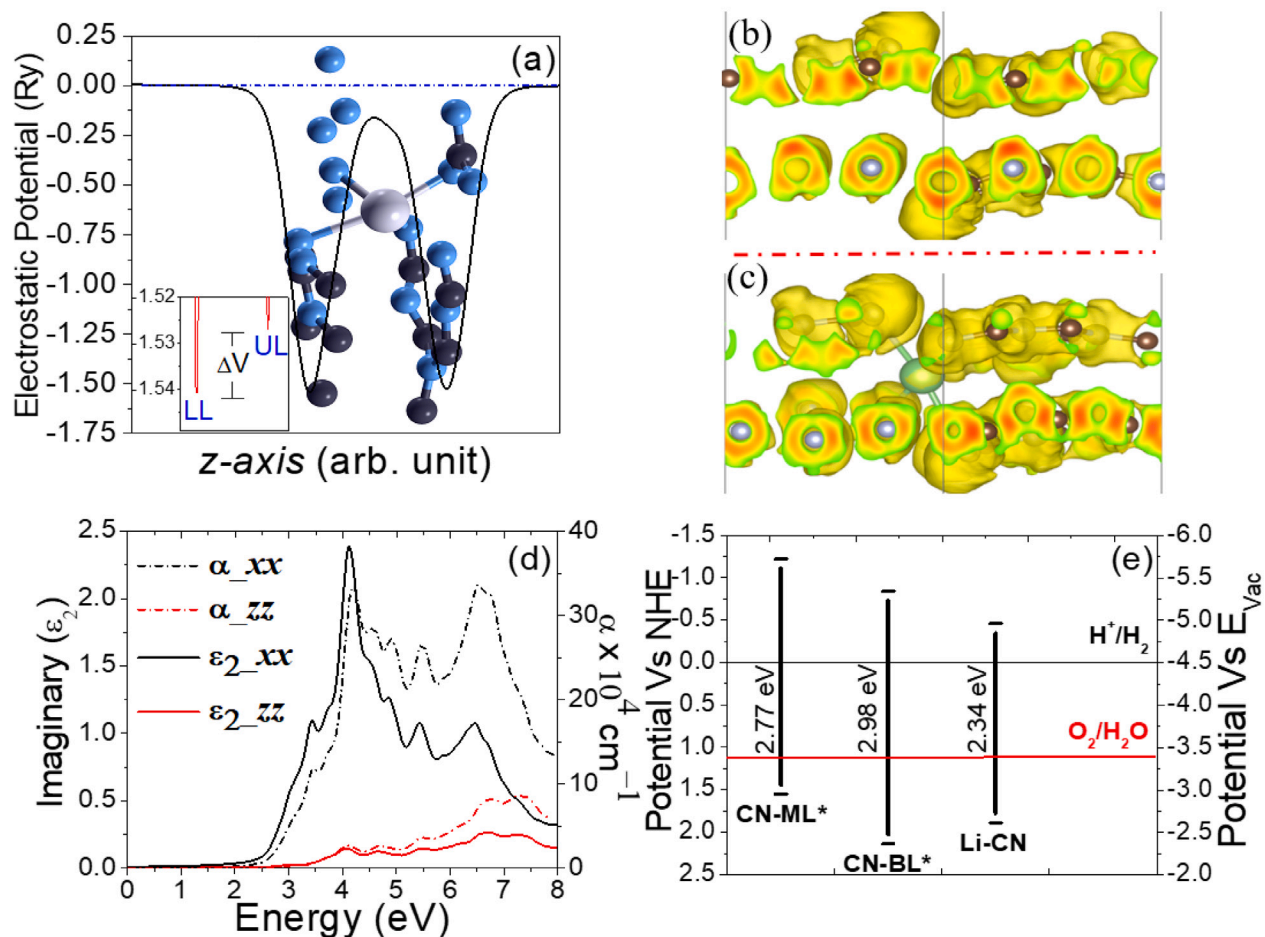


Fig. 2. (a) Electrostatic potential profile for potential variance against cell length (z-axis), inset highlights the variation in peak positions of LL and UL. Isosurface depicts the side view for (b) BL - CN, and (c) Li - CN electron localization functions. (d) Absorption coefficient (α) & imaginary part of dielectric function ($\epsilon_2(\omega)$) vs energy for Li - CN, where inset highlights the energy range 2.6–3.8 eV, and (e) Reduction-Oxidation potential for NHE/Vacuum energy for g - C_3N_4 monolayer, BL - CN, and Li - CN. *Represents the Ref. [2].

layers across xy -plane. Substantial variation in the layer alignment due to the Li-intercalation is governed by the modified orbital interaction between the layers. Interlayer bridging of alkali metal intercalated g - C_3N_4 is a result of the interaction of alkali metal with N^{edge} , as seen in previous reports [8,9,11,12]. Based on the electronegative character of N^{edge} , interlayer orbital interaction, and bent lone pair of the N^{edge} atom over/within interlayer tend Li to interact with the N atom. Atom apart from N^{edge} does not possess a tendency to strongly bond with an alkali element due to their suppressed electronegative nature compared to N^{edge} . Charge transfer from Li to $N_{UL/LL}$ leads to intralayer charge redistribution, as a result, corrugation is seen, although no distortion in the g - C_3N_4 network/ring is observed. The integrity of g - C_3N_4 tri-s-triazine structure is maintained experimentally as reported earlier signifying its feasible synthesis at the present concentration (3.57 at%) [16,17].

The electronic properties of Li - CN from energy bands and DOS reveal the formation of an n-type extrinsic semiconductor with a partially filled conduction band as shown in Fig. 1(c). Fermi energy (E_F) shift from -2.78 to -0.51 eV from BL - CN to Li - CN, attributed to the injection of electrons from Li-2s orbital to the system and contributes in the frontier orbital (FO) as a result of vertical interaction. With similar valence/conduction bands (VB/CB) states of UL/LL in BL - CN shown in Fig. S1, negligible interlayer charge transfer (Eq S1 and Table S1) [2] is seen. PDOS and LDOS plotted in Fig. 1(c) and S3, respectively highlight the contribution of $2p$ -orbital of N_{UL} , C_{UL} , N_{LL} ,

C_{LL} in CB, C_{LL} , N_{LL} in VB and origin of N_{UL}^{bridge} - $2p$ orbitals in the VB maxima signifying strong π -conjugation. The relative flatness of partially occupied CB and bending of VB maxima from $M \rightarrow K$ is the result of steep C_{UL} states and wide VB of Li, respectively. The indirect band gap (E_g) from $K \rightarrow M$ ($E_g = 2.34$ eV) and an almost similar direct band gap from $K \rightarrow K$ ($E_g = 2.36$ eV) are calculated. Similar features are observed from the energy band calculated using the Wannier function (Fig. S3). Highly curved CB minima attributing to high electron mobility and low curvature of VB maxima due to heavy holes in Li - CN challenges BL - CN due to its sharp CB and VB on the scale of effective mass variance ($\beta = m_e^*/m_h^*$; where m_e^*/m_h^* is the effective mass of electron/hole), inferring ~ 2.2 times decrement in recombination rate of photogenerated carriers [2]. Increase of occupied orbitals of C_{LL} , unoccupied orbitals of N_{LL} , and localization of FOs compared to BL - CN is significant and governs interlayer charge redistribution. Li intercalation result in ΔQ_{il} of $-0.131 e^-$, while interlayer orbital charge transfer $\Delta Q_{il}^{p_x}$, $\Delta Q_{il}^{p_y}$ and $\Delta Q_{il}^{p_z}$ of 0.035, -0.064 and $-0.115 e^-$, respectively (Table S1). LDOS (Fig. S2) and electrostatic potential plot (EPP) (Fig. 2(a)) verify the Löwdin charges, where the influence of LL atoms in VB is far superior to the contribution of UL atoms resulting in the formation of \bar{E}_{il} from LL \rightarrow UL, this \bar{E}_{il} is also favored by the position of Li atom which is tending towards UL. Orbital categorization seen from Fig. S2(c,d) further verifies activation of p_z -states for vertical charge transfer, as it shows intense states in CB as compared to p_x/p_y -orbitals. Significant changes in VB due to p_x , p_y ,

p_z , and s -orbitals of C/N in LL direct towards surface activation which is beneficial for high reactivity towards OER/HER. Fig. 2(b,c) depicts the electron localization function (ELF) supporting the reduced inter-layer separation, localization of electrons around Li-atom, enhancement of interlayer orbital interaction, and increment of charge difference between UL and LL (Table S1) after Li incorporation.

The synergistic effect of visible light absorbance, band edge straddling across reduction-oxidation (redox) potential, and reaction feasibility over the surface determine the potential of a photocatalyst. Fig. 2(d) shows the parallel, perpendicular component of α and ϵ_2 . Red-shifting of α due to narrowed E_g of Li – CN and higher absorption of visible photons is seen as compared to BL – CN [2]. The curve distortion in $\text{im}(\epsilon_2)$ is around 3.0 eV (shown in inset) attributing to interlayer orbital overlap as reported earlier in our work [2]. This orbital overlap is not visible in the monolayer (ML) [2], where it signifies the activation of the forbidden transition providing a broad energy range of photons to excite from VB to CB. Multiple peaks denote transition possibilities within the visible region of the spectrum, providing its capability to utilize the whole visible region. The band edges crossing redox potential seen from Fig. 2(e), display the capability of Li – CN for OER and HER.

3.2. HER and OER study

With structural relaxation on Li intercalation, the head-on orbital overlap between the interlayer atoms persisted, and bond formation creating a bridge as seen in Fig. 3(a) and Fig. 2(b, c). In order to study the OER/HER over different sites and to check the overall activity of the Li-CN photocatalyst, established fact reported previously [2,34] denoting most electronegative atom as a best suitable site for OER and highest e^- donating atom for HER is considered. As seen from Fig. 3(a) among such sites, N_1 with ΔQ of $-0.362 e^-$ considered as Site 1, N_3 with ΔQ of $-0.315 e^-$ as Site 2, N_2 with ΔQ of $-0.341 e^-$ as Site 3, C_4 with ΔQ of $0.371 e^-$ as Site 4, C_5 with ΔQ of $0.380 e^-$ as Site 5, and N_5 with ΔQ of $-0.351 e^-$ as Site 6 with Site 1,3,4/Site 2,5,6 are in UL/LL of Li-CN structure were considered as adsorption sites. In order to check the site selectivity for adsorption of water molecule over both the surface of Li – CN, sites have been screened on the basis of the charges accumulated/depleted over each which is the basis of the electronegative nature of the sites. From either of the layer, three different sites with 2 N and 1 C, N^{edge} and C^{corner} atom, respectively has been considered.

For OER, H_2O relaxation on Li – CN shows an average hydrogen bond (H-bond) of 1.892 \AA for $H - N^{\text{edge}}$, the average adsorption energy of H_2O molecule ($\Delta E_{\text{ads}}^{H_2O}$) of -0.613 eV over Sites-2, 3, 5, 6, inferring strong physisorption; and chemisorption over Sites-1, 4 with $\Delta E_{\text{ads}}^{H_2O}$ of $\sim -1.01 \text{ eV}$, which is differentiated on basis of charge donated by H_2O molecule as shown in Table S2 and 3 for comparison between Li – CN and BL – CN, respectively. Energetically stable *OH was computed for the next step, 1.644 \AA of C-OH average bond length and 2.218 \AA H-bond ($^*OH - N^{\text{edge}}$) for Sites-1,2,3,4,6 justify *OH interaction with Li – CN. Moreover, $\Delta E_{\text{ads}}^{OH}$ of -0.079 and 0.608 eV for Sites-1,3,4,5 and 2,6, respectively is attributed [55] to variation of ΔQ_{il} and ΔQ_{Li} as shown in Table S4. With H detachment from *OH , C-O bond length reduces to $\sim 1.296 \text{ \AA}$, while the addition of H_2O and release of e^-/H^+ pair leads to the formation of *OOH showing $\sim 1.508 \text{ \AA}$ average C-OOH bond length. *OOH on Site-1,3,4,6 have H-bond between $H - N^{\text{edge}}$ of $\sim 1.823 \text{ \AA}$, and no H-bond for Sites-2,5 is observed. *OOH at Site-2 shows $\Delta E_{\text{ads}}^{OOH}$ of 4.569 eV due to interlayer N-C bonding. Reactant adsorption is governed by electron transfer either by molecular orbital interaction or by the formation of the chemical bond, BL – CN/Li – CN evidently justify $\Delta E_{\text{ads}}^{\text{reactant}}$ as a function of $\Delta Q_{\text{if}}^{\text{reactant}}$. The surface interaction with adsorbate creates a unique interfacial charge redistribution based on the adsorption type, the type of bonding between them, and the molecule's polar nature, affecting further charge and reaction kinetics. This $\Delta E_{\text{ads}}^{\text{reactant}}$ further affects change in Gibbs free energy ($\Delta G^{\text{reactant}}$)

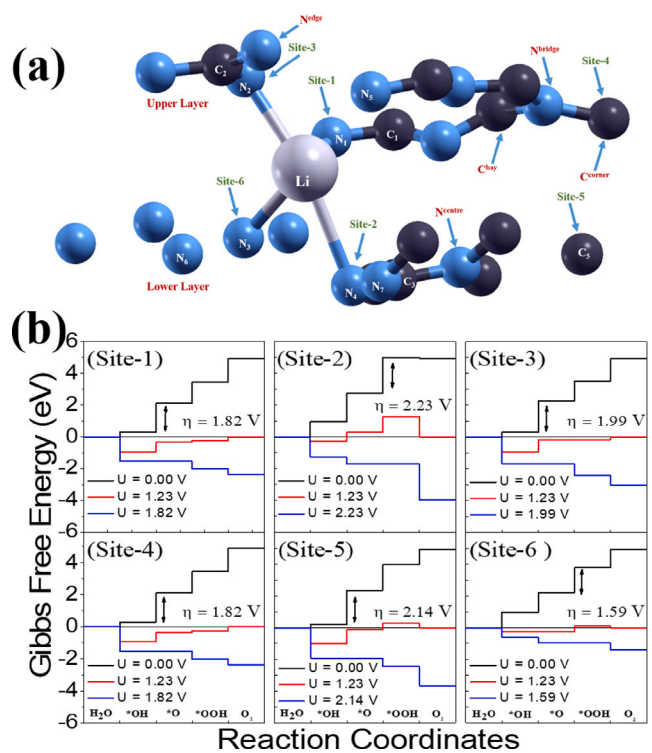


Fig. 3. (a) Optimized structure (unit cell) with highlighted sites for adsorption of intermediates, (b) Gibbs free energy profile for oxygen evolution reaction including Sites 1–6 over Li – CN.

hence overpotential ($\Delta\eta^{\text{OER/HER}}$). With exothermic nature for *OH adsorption Sites-1,3,4,5 have $^*OH \rightarrow ^*O$ as the rate-determining step (RDS) whereas, Sites-2,6 show *OOH formation step as RDS attributing to least $\Delta Q_{\text{if}}^{OH}$ and $\Delta Q_{\text{pe}}^{OH}$ from Table S4 and 5, respectively. $\Delta\eta^{\text{OER}}$ values of 0.59, 1.00, 0.76, 0.59, 0.91, and 0.35 V for Sites-1 to 6 show prominent results as an efficient photocatalyst as seen from Fig. 3(b).

Li – N^{edge} bonding in Li – CN facilitates H adsorption to C^{corner} and C^{bay} for Site-1,4,5,6 and Site-2,3, respectively with average C-H bond of 1.111 \AA and ΔE_{ads}^H of -0.797 and -0.732 eV respectively for Site-1,4,5 and 2,3. Site-6 shows the highest ΔE_{ads}^H of -1.043 eV attributing to the lowest charge transfer from Li to BL – CN assembly. In order to consider the effect of the dipole moment of an extra water molecule on ΔE_{ads}^H , H_3O^+ molecule is adsorbed over similar positions. Sites-1,5,6 show $\Delta E_{\text{ads}}^{H_3O^+}$ of -0.552 , -0.701 , -0.397 eV , respectively attributing to $\sim 1.051 \text{ \AA}$ N-H bond while no H-bond between H_2O molecule and Li – CN is seen. Strong chemisorption ($\Delta E_{\text{ads}}^{H_3O^+} - 1.148 \text{ eV}$) for Site-2,3,4 is a result of H-bond between H_2O and Li – CN along with $\Delta Q_{\text{if}}^{H_3O^+}$ of $0.382 e^-$ which is $0.065 e^-$ more than the other sites. $\Delta\eta_H^{\text{HER}}$ and $\Delta\eta_{H_3O^+}^{\text{HER}}$ of -0.49 V (Site-2/3) and -0.037 V (Site-6) lies within conduction band edge of Li – CN promoting it as efficient HER catalyst also seen from Fig. 4 (a,b).

The effect of ΔQ_{il} on the ΔE_{ads} of the next adsorbate can be visualized from Table S2, with low(high) $|\Delta Q_{\text{il}}^{H_2O}|$ corresponding low(high) $\Delta E_{\text{ads}}^{OH}$ is seen. Whereas, ΔE_{ads}^O is inversely proportional to $|\Delta Q_{\text{il}}^{OH}|$ for Site-1,2,3,4,5 with the exception of Site-6 due to interlayer Li bridging (Li settle in LL on *OOH adsorption), followed by linear proportionality between $\Delta E_{\text{ads}}^{OOH}$ and $|\Delta Q_{\text{il}}^O|$. From previous study [2,53] it is evident that charge transfer between adsorbate and adsorbent leads to interface modification, which thereafter will govern the next step of the reaction. ΔE_{ads} is governed by ΔQ_{if} occurring at the interface of reactant and Li – CN. Further, it governs the ΔG of reactant which tailors $\Delta\eta^{\text{OER/HER}}$. Thus, two major conclusions drawn here can be stated as, (a) interlayer bridging during the reaction favors isolation of

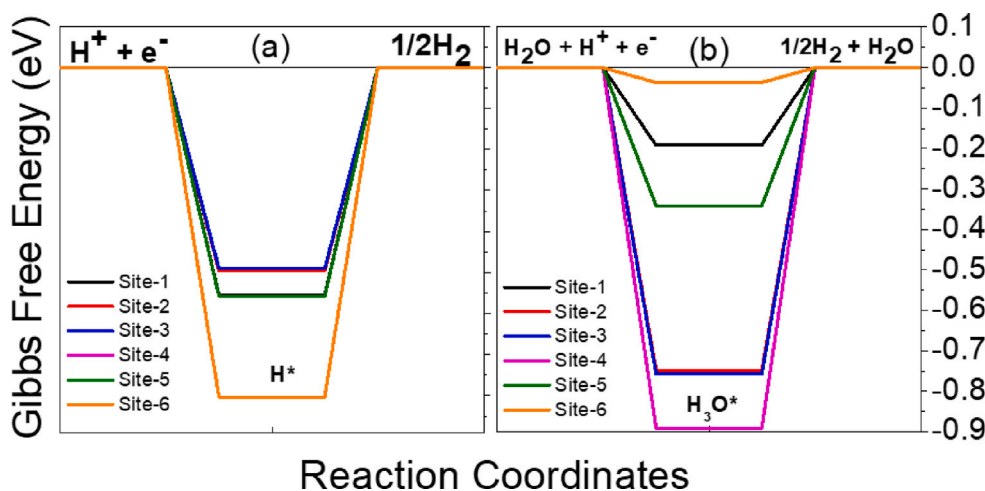


Fig. 4. Gibbs free energy profile for hydrogen evolution reaction including Sites 1–6 over Li – CN.

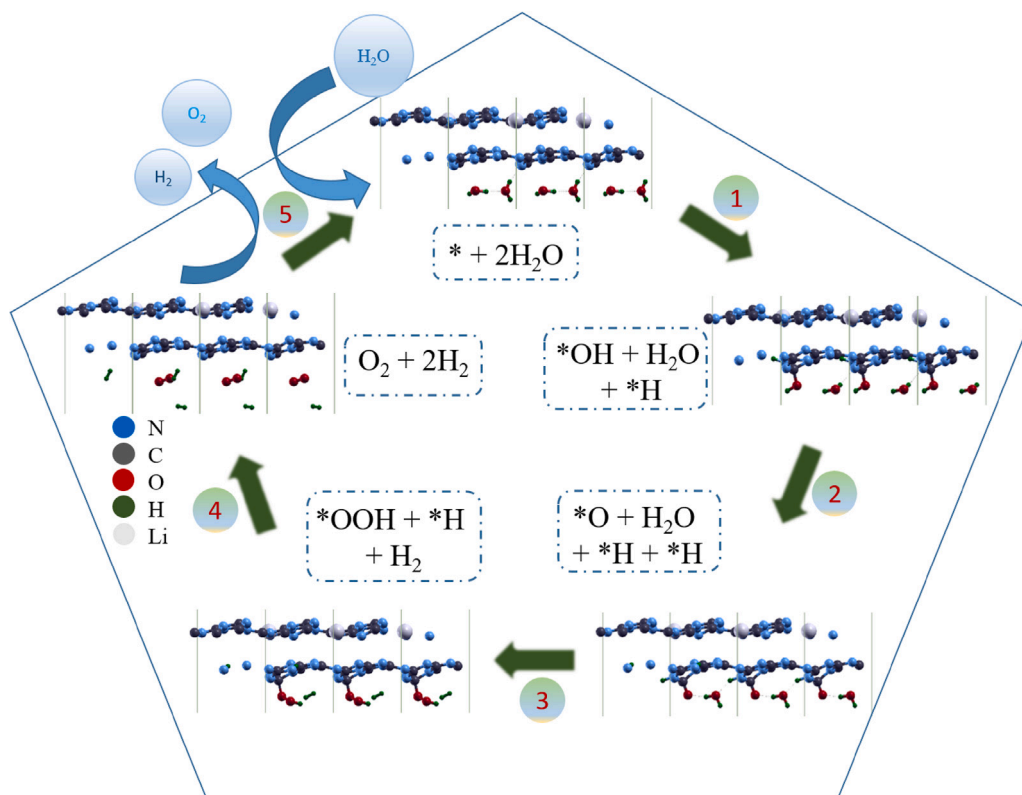


Fig. 5. Cyclic process for simultaneous oxygen evolution reaction & hydrogen evolution reaction over Li – CN.

Li-atom in the void of either layer of BL – CN and, (b) $\Delta Q_{il} / \vec{E}_{il}$ highly affects ΔE_{ads} of forthcoming reactant which itself is dependent on ΔQ_{if} therefore, coupling between ΔQ_{il} & ΔQ_{if} will inherently regulate adsorption of reactants.

Lack of study of simultaneous OER and HER, charge transfer analysis with a number of atoms consistent throughout the reaction (as in CHE method, atoms vary within the reaction due to different intermediates hence in that case CI-NEB could not be performed), and effect of intermolecular hydrogen bonding over the adsorption energy, whereas, the role of surface termination caused due to OER/HER over the corresponding HER/OER, respectively directed us to devise and simulate simultaneous oxygen and hydrogen production. Over a photocatalyst's surface formation of photoanodic (photocathodic), sites will lead to oxidation (reduction) resulting in oxygen (hydrogen) production

in the presence of two water molecules. The mechanism (Eq. (11) and shown in Fig. 5) is investigated here mainly to understand (i) structural variation based on the charge transfer on reactant adsorption and $E_{ads}^{reactant}$, (ii) correlation between \vec{E}_{il} & \vec{E}_{if} derived from the EPP and respective ELF analysis. In the simultaneous OER/HER, the structural integrity is maintained during the reaction, as in the earlier section where CHE has performed with no distortion on adsorbate interaction. Adsorption of two water molecules initiates the OER and HER, simultaneously resulting in the $\Delta E_{ads}^{H_2O}$ for single H_2O , two H_2O , and H_2O in the presence of another H_2O molecule to be -0.635 , -0.535 and -0.585 eV (calculated using Eqs S2-S4 to understand the variation on basis of termination), respectively. ΔQ_{il} on $2H_2O$ adsorption result in $-0.676 e^-$ attributing to decrement(increment) of electrons over LL(UL) and increment over $2H_2O$ as seen from Table S6. Owing to ΔQ_{il}

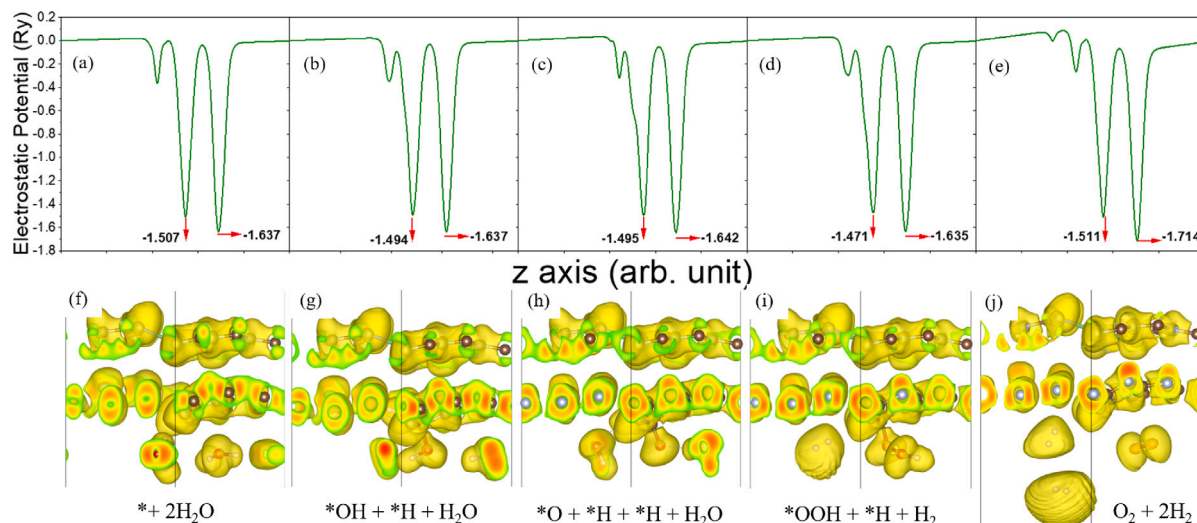


Fig. 6. (a–e) Electrostatic potential profile and, (f–j) electron localization function for simultaneous OER and HER.

and ΔQ_{if} , \vec{E}_{il} should be generated from $LL \rightarrow UL$ and \vec{E}_{if} between $2H_2O \rightarrow Li - CN$, conventionally. Since $2H_2O$ adsorption pushes Li into the void of CN_{UL} , the resulting magnitude and direction of \vec{E}_{il} can be seen from EPP. Although, potential difference ($\Delta V = V_{LL} - V_{UL}$) shows \vec{E}_{il} from $Li - CN_{UL} \rightarrow 2H_2O + CN_{LL}$ since the direction of \vec{E}_{il} (seen from ΔQ_{il}) is from LL to UL which is opposite to the direction of \vec{E}_{il} seen from EPP, it clearly indicated that the effect of $2H_2O$ adsorbed over $Li - CN$ is governing the effect of \vec{E}_{il} . The change in the direction of the electric field on water adsorption over the surface has modified the interfacial properties which directs us to consider the role of the newly formed interface over the modification of existing interlayer properties. With the large interlayer separation of the corresponding ELF as compared to pristine, the change in the shape of the isosurface to an ellipse for LL and N^{edge} lone pair directing towards the H_2O molecule shows a substantial effect of H_2O on interlayer orbital interaction. Extra H_2O on one hand interacts with already adsorbed H_2O while on the other hand, it maintains the formed \vec{E}_{il} when adsorbed H_2O molecule dissociates in forthcoming reaction [53]. In Step 1 the formation and adsorption of $*OH$, $*H$, and H_2O over respective sites resemble the site selectivity mentioned formerly. Isolated H_2O after N-H, C-OH bonding gains $0.031 e^-$ due to HOH-N H-bond resulting in a change of ΔQ_{if} due to and in favor of \vec{E}_{if} [55]. This ΔQ_{if} leads to the formation of $H_2O + (H, OH) - CN_{LL}/Li - CN_{UL}$ (Fig. 5, step-1) resulting in a reduction of an interfacial barrier for rapid charge movement and variation in \vec{E}_{il} [52]. This variation attributes to the increment (decrement) of total charge over LL (UL) from the prior step. ΔE_{ads}^{*OH} and $\Delta E_{ads}^{*H^1}$ (Eq S13) are -0.493 and -1.618 eV, respectively demonstrating the role of \vec{E}_{il} on ΔE_{ads}^{*OH} . This improves the interlayer orbital interaction as seen from Fig. 6(b, g) here, ΔV increases to 0.143 Ry, interfacial potential height decreases, and interlayer distance (potential height) decreases (increases). Reduction in the separation of interlayer distance and increased interlayer orbital interaction present the system as surface modified/surface decorated ((OH, H) - $CN_{LL}/Li - CN_{UL}$) heterojunction favorable for further deprotonation [8]. This surface modification/decoration forms an IVDWH [8], which clarifies the role of surface termination in the variation of interlayer properties. As the surface termination (adsorbates) changes so does the \vec{E}_{il} , and variation of \vec{E}_{il} governs the photoactivity by suppressing the energy barrier for the forthcoming intermediate adsorption.

The calculated value of ΔE_{ads}^{*O} and $\Delta E_{ads}^{*H^2}$ (Eq S14) from the next step (Fig. 5, step-2) calculated as -0.621 and -1.543 eV justify the case where coupled \vec{E}_{il} & \vec{E}_{if} reduces barrier height for next reaction. Second H release while $*O$ formation will determine whether HER will take place using Heyrovsky or Tafel mechanism, H instead of knocking

out adsorbed H from the H bonded N^{edge} , chooses to bond with N^{edge} changing the termination to $(2H, O) - CN_{LL}$. ΔQ_{il} of $-0.617 e^-$ for $(2H, O) - CN_{LL}/Li - CN_{UL}$ (Fig. 5, step-2) system strengthen the \vec{E}_{il} providing potential for water dissociation and feasible H_2 desorption through Heyrovsky or Tafel mechanism. Step 2 further shows an increased ΔV to 0.147 Ry as a result of $*OH$ dissociation into $*O$ & $*H$ and their respective adsorption. Interlayer distance increases while orbital interaction reduces as seen from Fig. 6(c, h) but the \vec{E}_{if} improves with potential dip reduction while an overall difference between the potential at either surface (over adsorbate and over $Li - CN_{UL}$) increasing as a result of electric field coupling. Here next water dissociation leads to the formation of C-OOH and H knocks bonded H and produces a hydrogen molecule (Fig. 5, step-3). The high ΔE_{ads}^{*OOH} of 3.186 eV attributes to the vanishing of \vec{E}_{if} and desorption of H_2 , resulting in a reduction in \vec{E}_{il} also seen from the reduced difference of electric potential from Fig. 6(d). $*OOH$ dip width increases along with ΔV in Fig. 6(d, i), and ELF shows reduced interlayer separation. Further increase (decrease) of total charge of LL (UL) and reduction in ΔQ_{il} (Table. S6) is responsible for the desorption of O_2 and H_2 molecules resulting in ΔQ_{il} of $-0.606 e^-$ attracting a large number of H_2O for OER/HER. With the highest ΔV of 0.203 Ry in Step 4, the formation of H_2 & O_2 takes place successfully while the resulting ELF shows similar features as for pristine. Huge variation in overall \vec{E} is seen due to dispersion of H_2 and O_2 away from the surface directing towards (i) no molecule accumulation over the surface for H_2O adsorption blocking, and (b) no reverse reaction which includes oxygen reduction reaction.

NEB formulation for E_a using minimum energy path and free energy change method for potential barrier ($\eta^{OER/HER}$) calculation resulted in similar findings despite the unresolved complexity (limitation of NEB in calculating the E_a for simultaneous OER and HER) of NEB as shown in Fig. 7. Computation of ΔG or E_a for two reactions taking place simultaneously is still an untouched phenomenon, using our devised method ΔG^{*OH} , ΔG^{*O} and ΔG^{*OOH} are found to be -0.143 , -0.571 and 3.586 eV, respectively for $U = 0.0$ eV. The calculated values of $\Delta \eta^{OER}(\eta^{OER})$ and lowest $\Delta \eta^{HER}$ are found to be 2.927 V (4.157 V) and 1.303 V, respectively. NEB on other hand provide E_a of 1.994 eV for $2H_2O \rightarrow N - H, C - OH, H_2O$ (Fig. 5, step-1); 2.4227 eV for $N - H, C - OH, H_2O \rightarrow N - H, C - O, N - H, H_2O$ (Fig. 5, step-2); 4.588 eV for $N - H, C - O, N - H, H_2O \rightarrow N - H, C - OOH, H_2$ (Fig. 5, step-3) and 3.721 eV for $N - H, C - OOH, H_2 \rightarrow 2H_2 + O_2$ (Fig. 5, step-4) verifying $*OOH$ formation to be rate determining step. Variations of E_a and $\eta^{OER/HER}$ along the whole water-splitting reaction follow the same path as that of Site-6 attributing to a direct relationship between the $\Delta E_{ads}^{reactant}$ and \vec{E}_{il} (ΔQ_{il}) of its previous step, which is regulated due

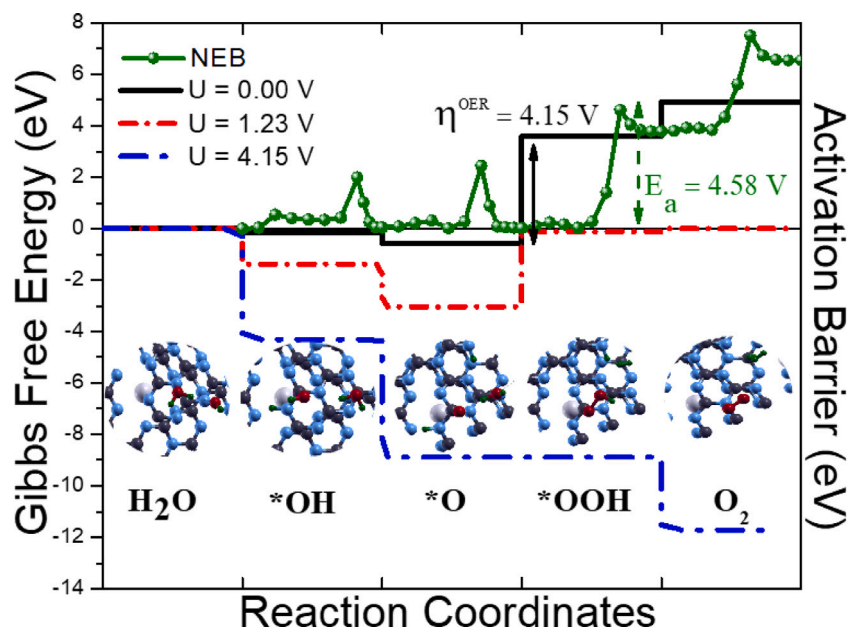


Fig. 7. Free energy change for OER and activation barrier for OER+HER performed over Li-CN surface.

to the \vec{E}_{if} (ΔQ_{if}) caused via adsorption of reactant. Site-6, with its lowest overpotential value dominates site reactivity for OER, therefore Site-6 will be preferred for extra water molecule adsorption signifying the importance of the electronegative region for suitable adsorption of molecules.

3.3. Charge transfer mechanism

While the reaction proceeds with different reaction intermediates the charge transfer within the interface of adsorbate-adsorbent is a governing factor to study the rate-determining step. The charge transfer mechanism depends on the type of adsorbate, its interaction with the surface, the polarity of the molecule, and the synergistic effect of a surface with its stacked layers, hence charge transfer investigation from the pristine step is crucial to understand the parameters required to enhance the photocatalytic activity. Li-intercalation is similar to alkali atom intercalation [6,8,11] and establish a potential difference across the stacked layers, and this potential difference leads to the generation of the interlayer electric field. Formation of IVDWH is understood on the basis of potential differences on the adsorption of various reaction intermediates, where band alignment will only decide the charge transfer channel, potential difference has explained the interfacial and interlayer charge transfer mechanism. With yellow, and blue regions denoting charge gain, and charge loss, respectively Figs. S4, S5, S6, and S7 show the charge density difference ($\Delta\rho$) of Li-CN, intermediate adsorbed Li-CN. Traditional formalism involving the difference between the charge density of the final system (Li-CN) and its component (Li & BL-CN) has been considered for pristine, while for adsorbed system three approaches for determination of interfacial and interlayer $\Delta\rho$ have been used (formalism is in the respective figures S4-S7). Pristine Li-CN from Fig. S4 (a, c) represents charge loss from Li and gained by the Li-N bond shown by blue and yellow regions, respectively. The surface of BL-CN shows interlayer charge gain as per the yellow region perpendicular to the surface, while intralayer charge depletion is seen from the blue region around the atoms. Charge gained by OH bond and lost by H atom over H_2O bonded with H-bond is seen on $2H_2O$ adsorption, while dipole over the other H_2O is seen. Here, the surface closer to H_2O shows the charge gained while the respective charge is lost over the dipole. Along with \vec{E}_{if} , ρ_2 show charge lost over the UL while gain over the LL signifying \vec{E}_{il} previously discussed (EPP part). Change in $\Delta\rho$ as the reaction proceeds shows

the variation of accumulation and depletion region of charges, in Step 1 $*OH$ and $*H$ shifts the charge loss region towards the N^{edges}_{void} with the reduced dipole of extra H_2O and redistribution of $\Delta\rho$ regions for ρ_2 . The dense charge difference on $*O$ and $*H$ formation in Step-2 increases charge loss over the N^{edge} of the void, this affects the $\Delta\rho$ on either side of the surface as seen from Fig. S6. Detachment of H_2 vanish $\Delta\rho$ around it, localizing its effect between the surface and $*OOH$ molecule with reduced magnitude. Although, the \vec{E}_{il} gains its strength in Step 3 due to a large difference. Finally, in Step 4, O_2 with large charge gain desorbed along with H_2 leaving CN_{LL} with charge depletion region and for ρ_2 clear charge accumulation/depletion pairing at both the interface justify the coupling between \vec{E}_{if} and \vec{E}_{il} . With an overpotential of 2.32 V, and 1.15 V over ML -, and BL -CN, respectively for oxygen evolution reaction, Li-CN shows 0.56 V which is ~ 4.1 , and ~ 2.05 times reduction respectively. Meanwhile, for the overpotential of hydrogen evolution reaction Li-CN shows ~ 3.4 times reduction, ~ 4 times increment from ML , BL -CN, respectively. Li-CN unlike ML -, BL -CN shows overpotential within the band edges directing potential for overall water splitting, hence showing superiority to the pure surface of pristine $g-C_3N_4$.

4. Conclusion

In the present work, the effect of Li intercalation in $g-C_3N_4$ bilayer is studied. Li intercalation affects the charge transfer mechanism of the system and the formation of a charge transfer channel between the layers of $g-C_3N_4$. Intercalation of Li generates an interlayer electric field (\vec{E}_{il}) between the upper and lower layers of $g-C_3N_4$, while as the reaction proceeds, interaction of reactant with photocatalyst surface generates an interfacial electric field (\vec{E}_{if}). This generated \vec{E}_{il} couples with the \vec{E}_{if} and assists efficient reactant adsorption. Bridging of $g-C_3N_4$ bilayer via Li affects the electronic and optical properties. Hence, high absorbance in the visible region, band edge straddling of reduction-oxidation potential, variation of \vec{E}_{il} , \vec{E}_{if} and $\Delta E_{ads}^{reactant}$ as the reaction proceeds reduce the overpotential of OER and HER over Li-CN as compared to BL -CN and promote Li-CN as an efficient photocatalyst. The present work also highlights the importance of two H_2O molecules to understand the simultaneous HER and OER reaction mechanism and charge transfer channel during the reaction. Li-CN is a potential material for water splitting, hydrogen production, and oxygen evolution, therefore it should be further explored experimentally.

Declaration of competing interest

The authors declare that they have no known competing financial interests or personal relationships that could have appeared to influence the work reported in this paper.

Data availability

Data will be made available on request.

Acknowledgments

AD is grateful to The M.S.U. Baroda for University Supported Research Project (2021–22) and University Grant Commission, New Delhi for Assistant Professorship under Faculty Recharge Program. AD would also like to acknowledge National Supercomputing Mission (NSM) for providing computing resources of ‘PARAM Ananta’ at IIT Gandhinagar, which is implemented by C-DAC and supported by the Ministry of Electronics and Information Technology (MeitY) and Department of Science and Technology (DST), Government of India. BRB is grateful to Pratik Lakhani for valuable discussions.

Appendix A. Supplementary data

Supplementary material related to this article can be found online at <https://doi.org/10.1016/j.surf.2023.103124>.

References

- [1] J. Wen, J. Xie, X. Chen, X. Li, Appl. Surf. Sci. 391 (2017) 72–123, <http://dx.doi.org/10.1016/j.apsusc.2016.07.030>.
- [2] B.R. Bhagat, K.H. Mali, A. Dashora, J. Phys. Chem. C 126 (5) (2022) 2573–2586, <http://dx.doi.org/10.1021/acs.jpcc.1c09973>.
- [3] Q. Xu, L. Zhang, B. Cheng, J. Fan, J. Yu, Chem 6 (7) (2020) 1543–1559, <http://dx.doi.org/10.1016/j.chempr.2020.06.010>.
- [4] R. Yang, X.-H. Lv, Y.-T. Ren, Y.-J. Zhang, H. Zhang, C.-D. Jin, R.-Q. Lian, R.-N. Wang, P.-L. Gong, X.-Q. Shi, J.-L. Wang, Phys. Rev. Mater. 6 (2022) 094011, <http://dx.doi.org/10.1103/PhysRevMaterials.6.094011>.
- [5] Q. Cao, F. Grote, M. Hußmann, S. Eigler, Nanoscale Adv. 3 (2021) 963–982, <http://dx.doi.org/10.1039/D0NA00987C>.
- [6] J. Li, W. Cui, Y. Sun, Y. Chu, W. Cen, F. Dong, J. Mater. Chem. A 5 (2017) 9358–9364, <http://dx.doi.org/10.1039/C7TA02183F>.
- [7] T. Xiong, W. Cen, Y. Zhang, F. Dong, ACS Catal. 6 (4) (2016) 2462–2472, <http://dx.doi.org/10.1021/acscatal.5b02922>.
- [8] J. Li, Z. Zhang, W. Cui, H. Wang, W. Cen, G. Johnson, G. Jiang, S. Zhang, F. Dong, ACS Catal. 8 (9) (2018) 8376–8385, <http://dx.doi.org/10.1021/acscatal.8b02459>.
- [9] X. Dong, J. Li, Q. Xing, Y. Zhou, H. Huang, F. Dong, Appl. Catal. B 232 (2018) 69–76, <http://dx.doi.org/10.1016/j.apcatb.2018.03.054>.
- [10] T.S. Bui, P. Bansal, B.-K. Lee, T. Mahvelati-Shamsabadi, T. Soltani, Appl. Surf. Sci. 506 (2020) 144184, <http://dx.doi.org/10.1016/j.apsusc.2019.144184>.
- [11] J. Li, X. Dong, Y. Sun, G. Jiang, Y. Chu, S. Lee, F. Dong, Appl. Catal. B 239 (2018) 187–195, <http://dx.doi.org/10.1016/j.apcatb.2018.08.019>.
- [12] W. Cui, P. Chen, L. Chen, J. Li, Y. Zhou, F. Dong, J. Phys. Energy 3 (3) (2021) 032008, <http://dx.doi.org/10.1088/2515-7655/abda9>.
- [13] P. Habibi, T.H. Saji, T.J. Vlught, O.A. Moulto, P. Dey, Appl. Surf. Sci. 603 (2022) 154323, <http://dx.doi.org/10.1016/j.apsusc.2022.154323>.
- [14] W. Zhang, Z. Zhang, S.H. Choi, W. Yang, Catal. Today. 321–322 (2019) 67–73, <http://dx.doi.org/10.1016/j.cattod.2017.12.012>.
- [15] Z. Zeng, X. Quan, H. Yu, S. Chen, W. Choi, B. Kim, S. Zhang, J. Catal. 377 (2019) 72–80, <http://dx.doi.org/10.1016/j.jcat.2019.07.018>.
- [16] B. Niu, J. Xiao, Z. Xu, J. Mater. Chem. A 9 (2021) 472–481, <http://dx.doi.org/10.1039/D0TA10881B>.
- [17] G. Gu, K. Wang, N. Xiong, Z. Li, Z. Fan, S. Hu, X. Zou, Dalton Trans. 48 (2019) 5083–5089, <http://dx.doi.org/10.1039/C9DT00013E>.
- [18] Z. Ge, A. Yu, R. Lu, Mater. Lett. 250 (2019) 9–11, <http://dx.doi.org/10.1016/j.matlet.2019.04.099>.
- [19] L. Ruan, G. Xu, L. Gu, C. Li, Y. Zhu, Y. Lu, Mater. Res. Bull. 66 (2015) 156–162, <http://dx.doi.org/10.1016/j.materresbull.2015.02.044>.
- [20] K. Bai, Z. Cui, E. Li, Y. Ding, J. Zheng, Y. Zheng, C. Liu, Modern Phys. Lett. B 34 (32) (2020) 2050361, <http://dx.doi.org/10.1142/S0217984920503613>.
- [21] T.T.H. Nguyen, M.C. Le, N.N. Ha, Mol. Simul. 47 (1) (2021) 10–17, <http://dx.doi.org/10.1080/08927022.2020.1858078>.
- [22] Y. Zhao, Y. Lin, G. Wang, Z. Jiang, R. Zhang, C. Zhu, Appl. Surf. Sci. 463 (2019) 809–819, <http://dx.doi.org/10.1016/j.apsusc.2018.08.013>.
- [23] J. Liu, J. Phys. Chem. C 119 (51) (2015) 28417–28423, <http://dx.doi.org/10.1021/acs.jpcc.5b09092>.
- [24] P.V. Kamat, J. Phys. Chem. Lett. 35 (2012) 663–672.
- [25] J. Bi, L. Zhu, J. Wu, Y. Xu, Z. Wang, X. Zhang, Y. Han, Appl. Organomet. Chem. 33 (10) (2019) e5163, <http://dx.doi.org/10.1002/aoc.5163>.
- [26] Q.-H. Zhu, Z. Chen, L.-N. Tang, Y. Zhong, X.-F. Zhao, L.-Z. Zhang, J.-H. Li, Int. J. Hydrog. Energy 44 (51) (2019) 27704–27712, <http://dx.doi.org/10.1016/j.ijhydene.2019.09.013>.
- [27] K. Wang, J. Fu, Y. Zheng, Appl. Catal. B: Environ. 254 (2019) 270–282, <http://dx.doi.org/10.1016/j.apcatb.2019.05.002>.
- [28] Y. Wu, D. Yang, W. Xu, R. Song, M. Li, Y. Wang, B. Zhou, N. Wu, W. Zhong, H. Ling Cai, J. Tu, D. Zhang, X. Wu, Appl. Catal. B. 269 (2020) 118848, <http://dx.doi.org/10.1016/j.apcatb.2020.118848>.
- [29] I.B. Stone, R.L. Starr, N. Hoffmann, X. Wang, A.M. Evans, C. Nuckolls, T.H. Lambert, M.L. Steigerwald, T.C. Berkelbach, X. Roy, L. Venkataraman, Chem. Sci. 13 (2022) 10798–10805, <http://dx.doi.org/10.1039/D2SC03780G>.
- [30] Z.K. Goldsmith, M. Secor, S. Hammes-Schiffer, ACS Cent. Sci. 6 (2) (2020) 304–311, <http://dx.doi.org/10.1021/acscentsci.9b01297>.
- [31] E. Skúlason, G.S. Karlberg, J. Rossmeisl, T. Bligaard, J. Greeley, H. Jónsson, J.K. Nørskov, Phys. Chem. Chem. Phys. 9 (2007) 3241–3250, <http://dx.doi.org/10.1039/B700099E>.
- [32] P. Dong, A. Zhang, T. Cheng, J. Pan, J. Song, L. Zhang, R. Guan, X. Xi, J. Zhang, Chinese J. Catal. 43 (10) (2022) 2592–2605, [http://dx.doi.org/10.1016/S1872-2067\(22\)64094-4](http://dx.doi.org/10.1016/S1872-2067(22)64094-4).
- [33] P. Dong, C. Meng, Y. Yan, B. Zhang, W. Wang, X. Xi, J. Zhang, Int. J. Hydrog. Energy 48 (49) (2023) 18670–18684, <http://dx.doi.org/10.1016/j.ijhydene.2023.01.357>.
- [34] J.K. Nørskov, J. Rossmeisl, A. Logadottir, L. Lindqvist, J.R. Kitchin, T. Bligaard, H. Jónsson, J. Phys. Chem. B 108 (46) (2004) 17886–17892, <http://dx.doi.org/10.1021/jp047349j>.
- [35] J. Rossmeisl, Z.-W. Qu, H. Zhu, G.-J. Kroes, J. and Nørskov, J. Electroanal. Chem. 607 (1) (2007) 83–89, <http://dx.doi.org/10.1016/j.jelechem.2006.11.008>.
- [36] G. Henkelman, H. Jónsson, Chem. Phys. 111 (15) (1999) 7010–7022, <http://dx.doi.org/10.1063/1.480097>.
- [37] G. Henkelman, B.P. Uberuaga, H. Jónsson, Chem. Phys. 113 (22) (2000) 9901–9904, <http://dx.doi.org/10.1063/1.1329672>.
- [38] W. Kohn, L.J. Sham, Phys. Rev. 140 (1965) A1133–A1138, <http://dx.doi.org/10.1103/PhysRev.140.A1133>.
- [39] P. Hohenberg, W. Kohn, Phys. Rev. 136 (1964) B864–B871, <http://dx.doi.org/10.1103/PhysRev.136.B864>.
- [40] R.O. Jones, Rev. Modern Phys. 87 (2015) 897–923, <http://dx.doi.org/10.1103/RevModPhys.87.897>.
- [41] P. Giannozzi, S. Baroni, N. Bonini, M. Calandra, R. Car, C. Cavazzoni, D. Ceresoli, G.L. Chiarotti, M. Cococcioni, I.D., et al., J. Condens. Matter Phys. 21 (39) (2009) 395502, <http://dx.doi.org/10.1088/0953-8984/21/39/395502>.
- [42] D.R. Hamann, Phys. Rev. B 88 (2013) 085117, <http://dx.doi.org/10.1103/PhysRevB.88.085117>.
- [43] J.P. Perdew, K. Burke, M. Ernzerhof, Phys. Rev. Lett. 77 (1996) 3865–3868, <http://dx.doi.org/10.1103/PhysRevLett.77.3865>.
- [44] J. Heyd, G.E. Scuseria, M. Ernzerhof, J. Chem. Phys. 118 (18) (2003) 8207–8215, <http://dx.doi.org/10.1063/1.1564060>.
- [45] J. Heyd, G.E. Scuseria, M. Ernzerhof, J. Chem. Phys. 124 (21) (2006) 219906, <http://dx.doi.org/10.1063/1.2204597>.
- [46] A.A. Mostofi, J.R. Yates, Y.-S. Lee, I. Souza, D. Vanderbilt, N. Marzari, Comput. Phys. Comm. 178 (9) (2008) 685–699, <http://dx.doi.org/10.1016/j.cpc.2007.11.016>.
- [47] N. Marzari, D. Vanderbilt, Phys. Rev. B 56 (1997) 12847–12865, <http://dx.doi.org/10.1103/PhysRevB.56.12847>.
- [48] I. Souza, N. Marzari, D. Vanderbilt, Phys. Rev. B 65 (2001) 035109, <http://dx.doi.org/10.1103/PhysRevB.65.035109>.
- [49] P. Blaha, K. Schwarz, F. Tran, R. Laskowski, G.K.H. Madsen, L.D. Marks, Chem. Phys. 152 (7) (2020) 074101, <http://dx.doi.org/10.1063/1.5143061>.
- [50] F. Tran, P. Blaha, Phys. Rev. Lett. 102 (2009) 226401, <http://dx.doi.org/10.1103/PhysRevLett.102.226401>.
- [51] J.K. Nørskov, T. Bligaard, A. Logadottir, J.R. Kitchin, J.G. Chen, S. Pandalov, U. Stimming, J. Electrochem. Soc. 152 (3) (2005) J23, <http://dx.doi.org/10.1149/1.1856988>.
- [52] D.D. Kemp, M.S. Gordon, J. Phys. Chem. A 112 (22) (2008) 4885–4894, <http://dx.doi.org/10.1021/jp801921f>.
- [53] H.-Z. Wu, L.-M. Liu, S.-J. Zhao, Phys. Chem. Chem. Phys. 16 (2014) 3299–3304, <http://dx.doi.org/10.1039/C3CP54333A>.
- [54] Electrochim. Acta 389 (2021) 138720, <http://dx.doi.org/10.1016/j.electacta.2021.138720>.
- [55] Y. Yang, A.K. Narayanan Nair, S. Sun, ACS Earth Space Chem. 3 (11) (2019) 2635–2645, <http://dx.doi.org/10.1021/acsearthspacechem.9b00236>.

Surface Activation of the g-C₃N₄ Bilayer by π -Conjugation and Interlayer Orbital Interaction to Promote OER and HER

Brajesh Rajesh Bhagat, Kishan H. Mali, and Alpa Dashora*

Cite This: <https://doi.org/10.1021/acs.jpcc.1c09973>

Read Online

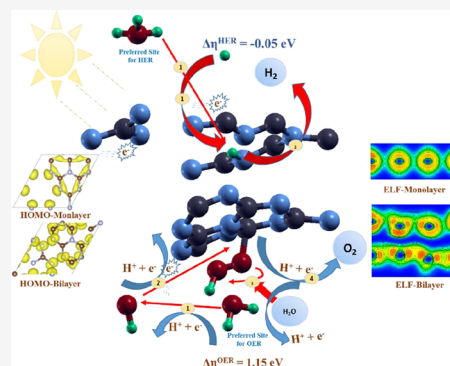
ACCESS |

Metrics & More

Article Recommendations

Supporting Information

ABSTRACT: A novel, eco-friendly, polymorphic graphitic carbon nitride (g-C₃N₄) bilayer with its potential application in photoresponsive and physicochemical properties enhanced due to interlayer coupling lacks investigation of different stacking configurations, interlayer atomic superposition, and their effect on photoactive reaction sites. Using the hybrid density functional theory, structural, electronic, optical, and photocatalytic properties of nine spatially modified bilayers referred to as S₀–S₈, together with site-dependent oxygen/hydrogen evolution reactions (OER/HER) on the most photoactive bilayer (S₃), have been explored in this work. vdW bilayers arranged considering all possibilities of interlayer atom–atom/atom–bond alignment along with the upper layer rotated by 0° (AA) and 180° (AB) on energy and force minimization are classified into planar (corrugated) geometry with band gap decrement (increment) compared to the monolayer, indicating the role of π -delocalization. Increased mobility, feasible surface migration, and reduced rate of recombination for photogenerated charge carriers in S₃ along with the highest optical absorbance indicated its importance over monolayer and other bilayer configurations. Among the different active reaction sites, the best suitable site on S₃ reveals 2 and 3 (20) times drop in value of overpotential for OER and HER (with an additional H₂O molecule), respectively, against the monolayer. Current analysis displays efficient charge carrier separation, in which charge transfer within the bilayer on intermediate adsorption and formation of an interfacial electric field illustrates the stepwise reaction mechanism and proclaims the synergistic effect of π -conjugation and interlayer orbital interaction for surface activation and improved photocatalytic activity of the g-C₃N₄ bilayer as compared to the monolayer.



1. INTRODUCTION

A change in the global demand from nonrenewable energy resources, which are at the edge of extinction, to reusable energy-generating resources calls for cooperation among technologists, industrialists, and scientists. Regarding applications of solar energy in terms of photocatalysts and photovoltaics, technology has been developed through research, but exposure to heavy metals and their excess exploration have put the environment at risk. The quest for nontoxic materials with properties better than those of metal oxides and sulfides brought us to graphitic carbon nitride (g-C₃N₄), a polymorphic lamellar structure with a broad band gap of 2.7 eV^{1–5} with suitable band edges for simultaneous reduction and oxidation reactions.⁶ The abundance of constituent elements in nature, active sites for doping/loading of the anion/cation or both, and cost-effective, easy synthesis method make g-C₃N₄ a prospective flexible photocatalyst. Although the rapid rate of recombination of photogenerated charge carriers, lack of active surface sites for redox reaction, and prohibitive overpotential⁷ have restricted its practical use at the large scale, researchers have tried to eliminate these limitations via various techniques like structural modification,⁸ vacancy creation,⁹ doping and loading of metals and nonmetals¹⁰ for either introduction of the intermediate state

or formation of extrinsic semiconductors toward one of the two reactions of water splitting. Functionalization of g-C₃N₄ along with decreasing dimensionality has led to the enhancement in hydrogen production,¹¹ dye degradation, overall water splitting, nitrogen reduction, and carbon dioxide reduction to hydrocarbon fuel at an exponential rate.^{12,13} This path of lower dimensionality has led to new fields of interest including homojunction and different types of heterojunctions for enhancing not only the photocatalytic activity but also its multifunctional applications by synergistic effects through possible combinations of diverse materials.^{14–16}

Promising enhanced visible light absorption, high quantum yield, and rapid displacement of photogenerated charges collected over the surface as a result of dense stacking configuration¹⁷ encouraged formation of nanosheets and nanoflakes for exorbitant photocatalytic activity. As the

Received: November 22, 2021

Revised: January 12, 2022

material approaches lower dimensionality, on the one hand, the quantum confinement effect leads to increment in the forbidden energy gap, while on the other hand, bifurcation of the stacked layer results in charge redistribution and increases planar and interplanar charge carrier mobility.¹⁸ A study by Wei and Jacob¹⁹ on the g-C₃N₄ monolayer (ML) with quasi-particle correction indicates enhanced electron–electron correlation resulting in an improved solar energy conversion efficiency by band gap tuning setup by excitonic absorption, which accounts for the dimensionality of the material. Interstitial and substitutional doping alters the connectivity pattern, causing a topological change in g-C₃N₄²⁰ and leading to high activity, indicating the synergistic effect of dopant's property and structural modification. A similar advancement in the redox reactivity carried out by intercalation of various alkali metals^{21,22} in the g-C₃N₄ bilayer (BL) and heterostructure^{23,24} is reported.

Subsequent theoretical and experimental investigations on the stability and photocatalytic activity of structurally modified layered g-C₃N₄ based on the interlayer orbital coupling and energetically most stable configuration have confirmed the major role of tri-s-triazine-based materials in the race of metal-free photocatalysts. The initial study by Gracia and Kroll²⁵ using ab-initio molecular dynamics reported stability of the layered configuration by avoiding repulsive forces between the nitrogen lone pair (LP), resulting in the formation of a corrugated but low energy structure. Azofra et al.⁸ have investigated carbon dioxide reduction reaction by a planar and stabilized corrugated ML configuration with a nitrogen LP located over the structural holes to reduce the repulsion, enhancing the catalytic performance of CO/CH₃OH by distorted geometry.

The exploration of the BL in 16 different configurations provided deeper insights into interlayer coupling and its visible light response, including stacking of bridged, edge nitrogen over each other along with other different alignment structures. Because of its increased visible light absorption and band gap compared to the ML, it can be applied in photovoltaic materials,²⁶ while studies on the stable structure based on the excitonic effect with the stacking range from the ML to four layers have been done for hydrogen evolution reaction (HER) considering ABAB stacking only.²⁷ Wang et al.²⁸ and Zuluaga and co-workers²⁹ worked on polyfunctional materials in the bulk form and discussed the off-plane distortion and interlayer stacking configuration for discrepancy in experimental lattice parameters and band gap tuning. The hybridization and overlap of p_z states showed an indirect relationship between the synthesis temperature and band gap of g-C₃N₄.²⁹ An excitonic perspective showed broadening of the absorption region due to transformation of dark excitation to bright excitation, activation of the electronic transition channel around Fermi, and localization of an electron–hole pair at reactive sites resulting in weakening of the N–H bond for efficient HER.^{26,27} Finally, a synthesis method including two-step ultrasonication–calcination yielding carbon nitride nano-sheets proved the increased HER efficiency by electron transport through tunneling between a vertically aligned C–N pair.³⁰

For steering the behavior of photoexcited electron–hole pairs that result in efficient separation, high mobility of charge carriers, and increment in recovery time, the following methods have been reported by Li et al.³¹ (i) formation of the heterojunction, (ii) regulation of spin polarization in the

catalyst, (iii) design of a donor–acceptor system via doping/decoration, and (iv) generation of excitons by functionalization.^{31–33} Another strategy to design the photocatalysts with high active sites and the desired surface is composition and modification of g-C₃N₄ into a BL, which can help in overcoming the problem of photogenerated charge carrier separation and its transfer that leads to reduction of the rate of recombination, providing a broad time window for oxidation and reduction reaction.

The available literature studies show enhanced visible light absorption due to π -conjugation and increment in charge carrier mobility^{17–19} and the interlayer interaction provides stability to the structure and variation in the band gap and generates interlayer electric field for efficient adsorption of intermediates in reaction mechanisms.^{8,22,23,25} Therefore, the synergistic effect of π -conjugation and interlayer interaction will be useful for enhanced photocatalytic activity. Despite investigations on certain photocatalytic reaction mechanisms, the study of oxygen evolution reaction (OER), exploration of C–N interlayer interaction, and its significance on the change in HER efficiency with water molecules is still lacking for the g-C₃N₄ BL. Possibilities of stable structural modification and its effect on photogenerated charge carrier dynamics for further improvement and understanding at a macroscopic level for studying the mechanism are urgently required in the current scenario.³⁴

The current work focuses on the role of π -conjugation and interlayer orbital interaction in the formation of a stable g-C₃N₄ BL considering the possible pair of bi-/tri-bonded N–N, C–C, and N–C orbitals, their electronic and optical properties, and the formation of active reaction sites for photocatalytic OER and HER, which were observed to possess low Gibbs free energy and overpotential values; it was further explained on the basis of interfacial electric field generation resulting from charge transfer as the intermediate radicals are adsorbed over the surface and improving photocatalytic activity as compared to the ML of g-C₃N₄.

2. COMPUTATIONAL DETAILS AND MODELS

Hybrid density functional theory implemented in QUANTUM ESPRESSO³⁵ code has been used to determine electronic and optical properties of the system using HSE06 functional^{36,37} for accurate band gap calculations; it is a combination of Perdew–Burke–Ernzerhof (PBE)³⁸ functional following generalized gradient approximation (GGA) and Hartree–Fock (HF), whereas structural and thermodynamical properties were computed using PBE–GGA. The screening parameter within the limit ($\omega < 0.15 a_0^{-1}$) is considered to be $\omega = 0.046 a_0^{-1}$ for obtaining a band gap value similar to that reported in previous studies.^{7,10} To simulate all electron results with high accuracy, all calculations are done using optimized norm-conserving Vanderbilt pseudopotentials^{39–41} with a plane wave-based basis set cutoff for kinetic energy of 60 Ry considered after the systematic convergence test with respect to the total energy of the system. Dispersion correction to the total energy for vdW interaction within the BL has been included using Grimme-D2 correction.⁴² For structural and thermodynamic calculation, a Γ -centered $5 \times 5 \times 2$ Monkhorst–Pack K point grid^{43,44} was used, while costlier hybrid functional-based properties were computed by a uniform $3 \times 3 \times 3$ grid. An energy cutoff of 10^{-6} eV for electronic optimization and a force convergence threshold of 10^{-3} eV Å⁻¹ per atom for relaxation of atomic positions and

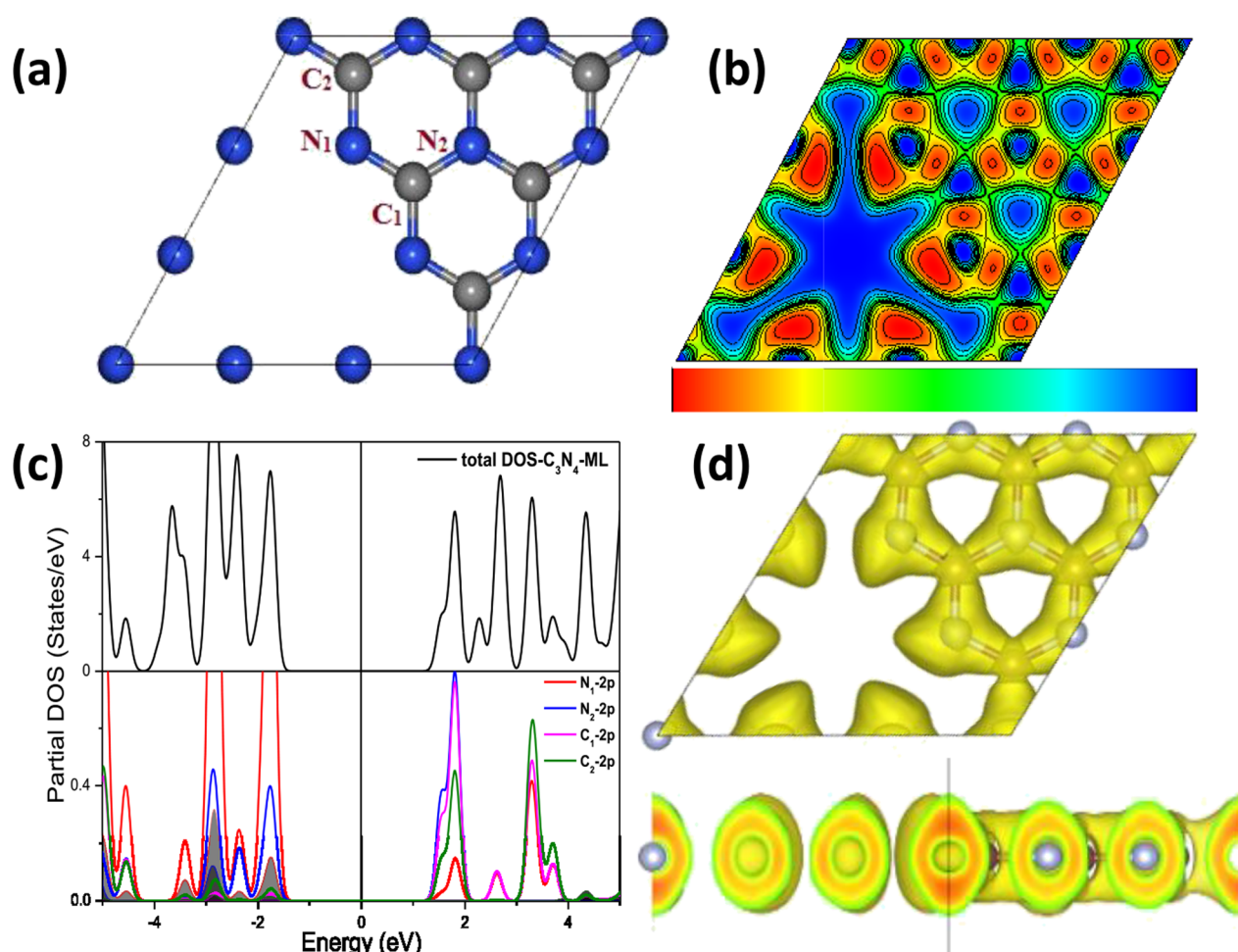


Figure 1. (a) Ball and stick model with marked N (blue) and C (gray) atoms, (b) electron localization function (ELF) contour (001), (c) total and partial density of states, and (d) 3D ELF isosurface of the g-C₃N₄ monolayer.

unit cells were used throughout self-consistent field iterations. For the visualization of different forms of the BL, XCrySDen⁴⁵ software is used.

Tri-*s*-triazine-based g-C₃N₄ with three triazine moieties bridged by a single N atom consisting of 8 N and 6 C atoms in the unit cell is studied in this work along with other allotropes for its stability and photocatalytic activity.^{46,47} Because the same chemical environment is provided due to periodicity, we have considered the unit cell of lattice parameter 7.14 Å for the ML and BL study, with a vacuum of ≈16 Å and an interlayer distance of 3.275 Å along with isolating layers in 2D to truncate the Coulomb interaction in the *z* direction, thereby eliminating any interaction with the next periodic layer in the case of BL structures, which consists of 28 atoms in total (16 N + 12 C).

The different BL structures, namely, S₀, S₁, S₂, S₃, S₄, S₅, S₆, S₇, and S₈, are considered on the basis of interlayer atomic/bond alignment to study the type of feasible atomic orbital alignment in vertical layer stacking. Here, structures S₀, S₁, S₂, and S₈ are AA (without rotation)-stacked, and S₀ represents the BL where the tri-*s*-triazine moieties are exactly over each other; for S₁, the upper layer (L_U) is displaced so as to align bay carbon (C₁) over the threefold coordinated (N₂) hybridized N of the lower layer (L_L); for S₂, the L_U is placed in such a way that the atoms of the L_U align over the bonds of L_L; and for S₈, N₂ lies over the void of the L_L and similar atoms

are placed over each other. The remaining structures S₃, S₄, S₅, S₆, and S₇ are AB-stacked, with the L_U rotated 180° with respect to the L_L; S₃ shows the position of N₂ of the L_U over the void of the L_L and C atoms align over N atoms; in S₄, the L_U is slightly displaced along the *xy* plane than S₃, but with atoms aligned over the bonds; S₅ consists of the least direct atomic alignment with N₁ of both layers aligned over each other; S₆ includes alignment of N atoms over the pore of hexagon, while C atoms are aligned with C of either layer; and S₇ shows the alignment of similar N atoms of both the layers over each other. To analyze the interlayer bonding strength and structural stability, cohesive energy is calculated for all the BLs (S₀–S₈) using

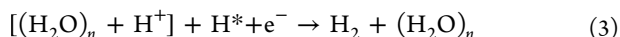
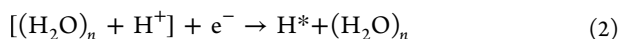
$$\Delta E_{\text{Coh}} = E_{\text{BL}} - 2 \times E_{\text{ML}} \quad (1)$$

where E_{BL} and E_{ML} are the total energy of the BL and ML, respectively.

To study the single-electron transfer step of HER and the four-electron transfer mechanism of OER, we have used the method developed by Nørskov and co-workers,^{48,49} which involved calculation of Gibbs free energy (ΔG) preceded by adsorption energy of intermediates, as mentioned in our previous work.¹⁰

The single-electron transfer step of Volmer–Heyrovsky for HER with $n = 0$ corresponding to the isolated hydrogen atom adsorbed over the surface and $n = 1$ implies the effect of extra

water molecules along with the corrected ΔG equation reported by Nørskov et al.,⁵⁰ which is given below:



$$\Delta G_{\text{H}^*} = \Delta E_{\text{H}^*} + 0.24 \quad (4)$$

$$\eta^{\text{OER}}(\eta^{\text{HER}}) = \max_i[\Delta G_i] - 1.23 \text{ (0.0) V} \quad (5)$$

(i denotes the intermediate)

Correction based on the effect of extra water molecule is followed accordingly for the calculation of ΔG .

3. RESULTS AND DISCUSSION

3.1. Structural Properties. The ball and stick model of the ML of $\text{g-C}_3\text{N}_4$ is shown in Figure 1, where blue balls correspond to N atoms and gray balls correspond to C atoms; on the basis of hybridization and position of the atoms in the cell, N has been divided into three and C into two different forms. In the present study, the nomenclature of the N and C atoms is as follows: N_1 and N_2 correspond to the bi- and tri-bonded form of the atom present at the edge and center of the mesh, respectively, with N_1 being highly electronegative as compared to other atoms because of high charge density; C atoms are labeled as C_1 and C_2 , and both are tri-bonded with C at the bay and corner position, respectively, of the triazine mesh. The unit cell of the ML containing eight N atoms, in which six atoms are type N_1 , one atom is type N_2 , and one is N atom, bridges three triazine moieties, while there are three C_1 and three C_2 atoms with six C atoms in total. The optimized lattice parameter and atomic position of the ML $\text{g-C}_3\text{N}_4$ ^{10,51} with vdW correction have been used to design the spatially modified BL with different layered alignments, as shown in the first column of Table S1, while the second column contains its corresponding optimized structure. Visible structural similarity and energy difference in nine BL configurations (S_0 – S_8) leads us to categorize them into three different sets: Set 1, which includes S_3 , S_4 , and S_6 , and Set 2, which includes S_1 and S_2 , where each set has an almost similar structure along with a similar cohesive energy, while all other dissimilar structures S_0 , S_5 , S_7 , and S_8 can be combined in Set 3. This classification shows the existence of only few stable structural orientations even if thousands of randomly arranged $\text{g-C}_3\text{N}_4$ layers were initially considered as reported by Wang et al.²⁸ and Zuluaga et al.²⁹ with experimental verification, which suggested that variation in the stacking configuration is dependent on the synthesis temperature.

As discussed in the previous section, initial models were classified into two categories: (1) layer displaced over each other without rotation and (2) the upper layer with 180° rotations with displacement. Furthermore, on the basis of atomic alignment, all optimized structures can be classified into two categories as planar (no distortion in the z -axis for the BL) $\{\text{S}_0, \text{S}_5, \text{S}_7, \text{and } \text{S}_8\}$ and corrugated (distortion in the z -axis) $\{\text{S}_1, \text{S}_2, \text{S}_3, \text{S}_4, \text{and } \text{S}_6\}$ geometry, as a result of the short-distance atomic orbital interaction. As was predicted, the interlayer orbital interaction among C–N, C–C, and N–N with an increasing strength of repulsion (decreasing strength of stability) was also seen from the final structures. The change in interlayer separation (ΔD), calculated as the difference between the initial (3.275 Å) and final average atomic

positions in the z -axis, is tabulated in Table 1, which clearly indicates the role of orbital interaction in the BL; in the case of

Table 1. Computed Value for Cohesive Energy (E_{coh}), Interlayer Distance Difference (ΔD), Band Gap (E_{g}), Fermi Energy (E_{F}), Vacuum Energy (E_{vac}), Work Function (Φ), and Band Gap Center (E_{BGC})

| structure | E_{coh} (eV) | ΔD (Å) | E_{g} (eV) | E_{F} (eV) | E_{vac} (eV) | Φ (eV) | E_{BGC} (eV) |
|--|--------------------------|-------------------|------------------------|------------------------|--------------------------|----------------|--------------------------|
| $\text{g-C}_3\text{N}_4$ - S_0 | −0.02 | −0.233 | 2.41 | −4.31 | 3.15 | 7.46 | −4.76 |
| $\text{g-C}_3\text{N}_4$ - S_1 | −0.11 | −0.569 | 2.95 | −4.56 | 3.47 | 8.03 | −5.06 |
| $\text{g-C}_3\text{N}_4$ - S_2 | −0.11 | −0.570 | 2.96 | −4.55 | 3.47 | 8.02 | −5.05 |
| $\text{g-C}_3\text{N}_4$ - S_3 | −0.13 | −0.390 | 2.98 | −4.52 | 3.48 | 8.00 | −5.09 |
| $\text{g-C}_3\text{N}_4$ - S_4 | −0.13 | −0.345 | 2.96 | −4.51 | 3.48 | 7.99 | −5.14 |
| $\text{g-C}_3\text{N}_4$ - S_5 | −0.05 | 0.006 | 2.68 | −4.29 | 3.14 | 7.43 | −4.62 |
| $\text{g-C}_3\text{N}_4$ - S_6 | −0.13 | −0.343 | 2.97 | −4.51 | 3.47 | 7.98 | −5.12 |
| $\text{g-C}_3\text{N}_4$ - S_7 | −0.02 | −0.039 | 2.61 | −4.33 | 3.15 | 7.48 | −4.65 |
| $\text{g-C}_3\text{N}_4$ - S_8 | −0.05 | 0.103 | 2.57 | −4.32 | 3.14 | 7.46 | −4.59 |

S_5/S_8 , the positive value points toward the presence of triazine moiety of one layer over the void of another and similar atoms (C–C and N–N) aligned over each other. For structures of Sets 1 and 2, the values are similar for each set, and a similar atomic configuration provides us the reason for the non-corrugated structures (S_0 , S_5 , S_7 , and S_8); on the other hand, atomic alignment of nonsimilar (C–N) atoms (S_1 , S_3 , S_4 , and S_6) or atoms over the bonds (S_2 , S_4) leads to corrugated geometry in the BL. The planar structures show an increase in lattice parameters a and b , whereas decrement is observed in corrugated structures, while c had a trivial visible change due to the isolation of the layer in 2D and suppression of interlayer Coulomb interaction due to the domination of s , p orbital in planar structures, as only an increase in bond length and a decrease in the angle are seen for atoms over each other, and the perpendicular p orbital governs corrugated structures.

Charge density of each atom generates an equipotential surface around the atoms in the ML of $\text{g-C}_3\text{N}_4$; on introducing another layer in the vicinity of the surface, respective atoms balance their forces based on the orbital interaction leading to structural changes, while this region around the atom promotes free movement of the atom present in both the layers, leading to an infinite number of possibilities of the position and orientation. However, due to the constrained degree of freedom caused by the presence of chemical bonds and LP, the number of possibilities is reduced, but remains high in the case of the multilayer system. Such a phenomenon give rise to energetically stable but visibly different structures. In our case, similar structures in Sets 1 and 2 show this property in terms of cohesive energy.

The exothermic nature of the reaction is indicated by the negative value of cohesive energy calculated using eq 1, while the magnitude determines the stability, making Set 1 most stable, followed by Set 2 and then Set 3. A similar stability study^{28,29} also concluded that the $\text{S}_3/\text{S}_4/\text{S}_6$ type structure is most stable in the bulk form of tri- s -triazine, which is proclaimed by the maximum dissimilar atomic orbital

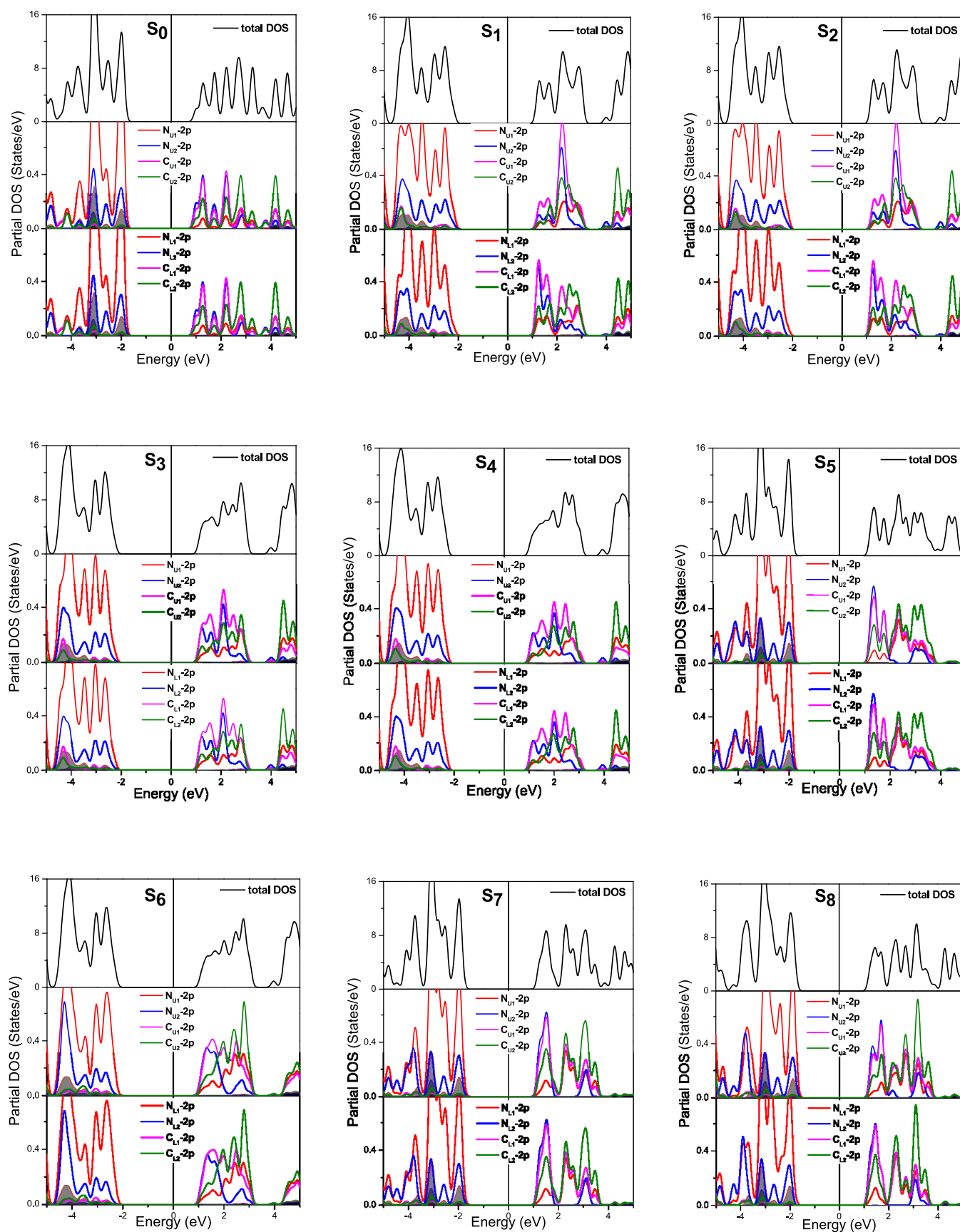


Figure 2. Total and partial density of states for the bilayer tri-s-triazine-based $g\text{-C}_3\text{N}_4\text{:S}_0\text{--S}_8$ structures; Fermi energy is shifted and is at 0.0 eV at the x -axis.

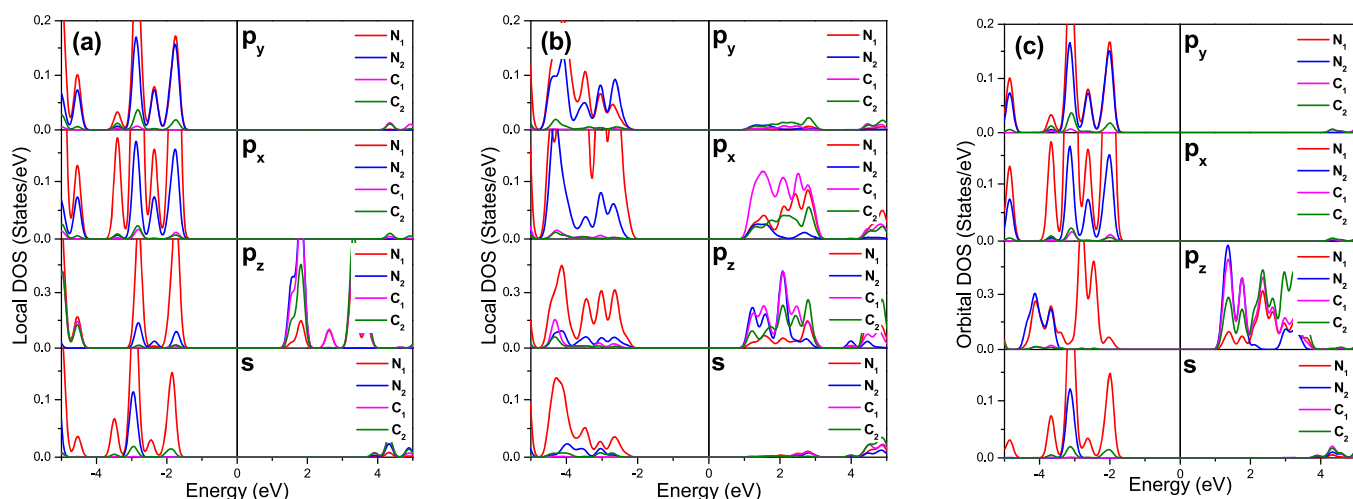


Figure 3. Local density of states for (a) monolayer and bilayer, (b) S_3 , and (c) S_5 g- C_3N_4 for s , p_z , p_x , and p_y orbitals.

interaction among all structures. Thus, a well-known design method for the most stable BL that includes avoiding N atom LP repulsion needs remodeling by inclusion of the highest number of interlayer C–N atomic orbital overlap to further decrease its energy. This minimization of forces due to interlayer orbital coupling leads layers to slide over each other along the x - y plane in a multilayered system, leaving us with a handful of possible stable structures. The multimedia file MMS1 explains the phenomenon of structural optimization of S_6 ; initial shifting of the layer and alignment of similar atoms over each other along with corrugation is seen, followed by increasing layer separation due to LP repulsion and finally displacement of both the layers over each other. As was reported earlier, when we move higher on the number of layers, the constraints increase, which decreases the free movement of the layer, and also π -localization decreases in the presence of a reactive surface. Thus, the system, instead of going to global minima potential, confines itself in local minima to restrain structural changes. Thus, the interplay of planar localization of electrons and interlayer orbital coupling will be most effective in the bi-layer form of heptazine g- C_3N_4 .

3.2. Electronic Properties. Hybrid DFT eliminates the underestimation of band gap caused by the GGA functional by adding a part of HF in the exchange correlation functional and thus is widely used for the study of photoresponsive materials and their applications. Here, electronic properties have been studied using HSE06^{36,37} functional, and the total density of states (DOS) has been computed for all the BLs (S_0 – S_8) and the ML system is presented in Figure S1. Also, the computed Fermi energy (E_F), band gap (E_g), vacuum energy (E_{vac}), band gap center (E_{BGC}), and the corresponding work function (Φ) of BLs are tabulated in Table 1. The electron localization function (ELF) for S_0 – S_8 has been tabulated in Table S1. The 2D ELF contour along the 001 plane for the ML is also presented in Figure 1b with its scale range from 0.0 to 1.0 in terms of bond strength, where $0.0 < \text{ELF} < 0.5$ (blue region) shows ionic bonding, ≈ 0.5 (green region) shows metallic bonding, and $1.0 > \text{ELF} > 0.5$ (red region) shows covalent bonding, whereas the highest electron density is presented in red, signifying the presence of LP/free electrons. Along with total DOS, projected DOS (PDOS) that includes the separate orbital states has also been computed, as shown in Figure 1c and 2, for the ML and BL, respectively. We have computed E_g

= 2.77 eV for the ML, which was also reported earlier^{10,51,52} with PDOS, presenting the dominating role of N_1 in the bonding and hybridization of N_2 , C_1 , and C_2 in the anti-bonding orbitals. The ELF plot shows the π -localization over the plane for rapid charge carrier mobility, and contour shows sp^2 bonding of C–N atoms in the presence of the LP at the edge N atom, making them most electronegative and suitable sites for intermediate adsorption for redox reaction.

The structural changes in the BLs can be verified by the ELF and DOS plot. From the 3D ELF images shown in Table S1, the uniformity in charge density perpendicular to the plane in planar S_0 , S_5 , S_7 , and S_8 BLs implies the balancing interlayer orbital interaction through symmetric distribution of spreading of the charge cloud in the x - y plane as the side glance of ELF shows spherical charge distribution, which was ellipsoid for the ML (Figure 1d). The corrugated structures display the repulsion of the charge clouds and felicitous arrangement between orbitals of C–N atoms across the z -axis of BLs. Figure 2 shows a decrease in E_g for planar BLs, which is associated with (a) the sharp and distinct peak formed in the valence band maxima (VBM) region around -2.0 eV due to the N_1 atom, (b) the sharp peaks in the conduction band minima (CBM) dominated by N_2/C_1 atoms in the region around 1.5 eV, which is shifted toward E_F , and (c) electronic states formed by the s orbital for C/N atoms shifting toward a lower energy region, implying the electron density confinement but slight delocalization in VB(CB) around -2.5 eV (2.0 eV) as compared to the ML. On the one hand, for corrugated BLs (S_1 , S_2 , S_3 , S_4 , and S_8), the structure of Set 2 shows almost the same features due to its structural similarity. On the other hand, we observe a slight difference in the VB for Set 1 and a large change in the CBM as a result of a change in ΔD (as mentioned in Table 1) of triazine moieties in the BL, which is also seen by the domination of N_2 2p-states in S_6 with respect to S_3/S_4 in CBM and domination of C_2 around 2.75 eV observed in Figure 2. The BLs with 0° -layer rotation (S_0 , S_1 , S_2 , and S_8) show a change in the PDOS of the L_U and L_L except in S_0 , but for BLs with 180° rotations (S_3 , S_4 , S_5 , S_6 , and S_7), PDOS is exactly the same for both the layers. In the upper layer of the Set 2 structure, C_1 dominates the CBM and L_L shows hybridization of C_1 and N_2 . On close examination, the difference in origin of CB in different BLs is attributed to the value of ΔD because the domination of CB by p_z orbital layer

separation plays a major role in the band gap arising from the combined properties of π -localization and interlayer orbital coupling.

The quantum confinement effects increase the band gap, as we move toward the ML. Thus, the BL should show a lower E_g value with respect to the ML, although corrugated BLs in this study show the increment of E_g , pointing toward the involvement of orbital contribution in the system. Local DOS (LDOS) for the ML and BL (S_3 and S_5 ; as representative structures from corrugated and planar class) is presented in Figure 3. Figure 3a,c shows the domination of VBM by N s , p_x , and p_y states, while C p_z states comprise CBM. Sharp peaks in the VB region around -1.9 eV for the ML and S_5 for N s , p_x , and p_y testify their planar geometry. LDOS of S_3 shows high contribution of the N p_x orbital, suppression of the existing C p_z states, and small contribution of anti-bonding states of C s and p_y in CBM resulting from delocalization of unoccupied states over the plane. By comparison of Figure 3a,b, it can be found that domination of p_x states for N_1 , quenching of N_1 's p_y states along with $2p$ and $2s$ orbitals, and merging and shifting toward the lower energy in VB lead to an increased band gap value, denoting the role of orbital interplay in the quantum confinement phenomenon for a more stable stacking configuration system, providing a conclusive proof for the experimental values.³⁰

The highest occupied molecular orbital (HOMO) and lowest unoccupied molecular orbital (LUMO) carry information about the possibility of the presence of charge carriers in the atomic orbitals, providing charge transfer and hybridization states. For the ML, from Figure 4a,b, localization of the HOMO over low coordinated N atoms and that of the LUMO over the C_1 , C_2 , and N_2 atoms (also verified by PDOS) not only show uniformity in the z -axis but also reduce the separation of the electron/hole (e^-/h^+) pair and the photocatalytic efficiency of the material. Therefore, to enhance the efficiency, we require a higher occupancy in the anti-bonding orbital to induce weaker binding strength. From Figure 4c,d, it can be found that for S_3 , the corrugation in the BL brings an increase in transition of e^- to N in its π^* anti-bonding orbitals from the LP states of the bonding orbital, and an increase in unoccupied states of C in CB resulting from π conjugation suggests the direction of the electron delivery toward the most suitable site for the redox reaction intermediate adsorption. Symmetric localization of charge density over the atoms in both the HOMO and LUMO is shown in Figure 4e,f as a result of interlayer interaction, where the HOMO shows LP bending due to the presence of voids. Vanishing charge density in the LUMO as compared to the ML signifies its decreased π -conjugation, leading to reduced surface sites for the reaction. ELF contour of the (100) plane for the ML is shown in Figure 4g. It presents the equipotential surface, and Figure 4h presents facilitation of partial hybridization in the S_3 BL between π -LP after shifting of LP downward contributes to system's stabilization due to on-site orbital resonance compensated by increased charge density and tilt angularity of both layers, which provide reactive sites on either side of the system for simultaneous reduction–oxidation reaction in BL (S_3) arrangement, which is not visible in S_5 (Figure 4i).

The band structure presented in Figure S2 computed along the Γ -M-K- Γ k -path of the Brillouin zone of the hexagonal cell structure for MLs and BLs shows the effect of structural changes on the bands along the k -path. The planar and

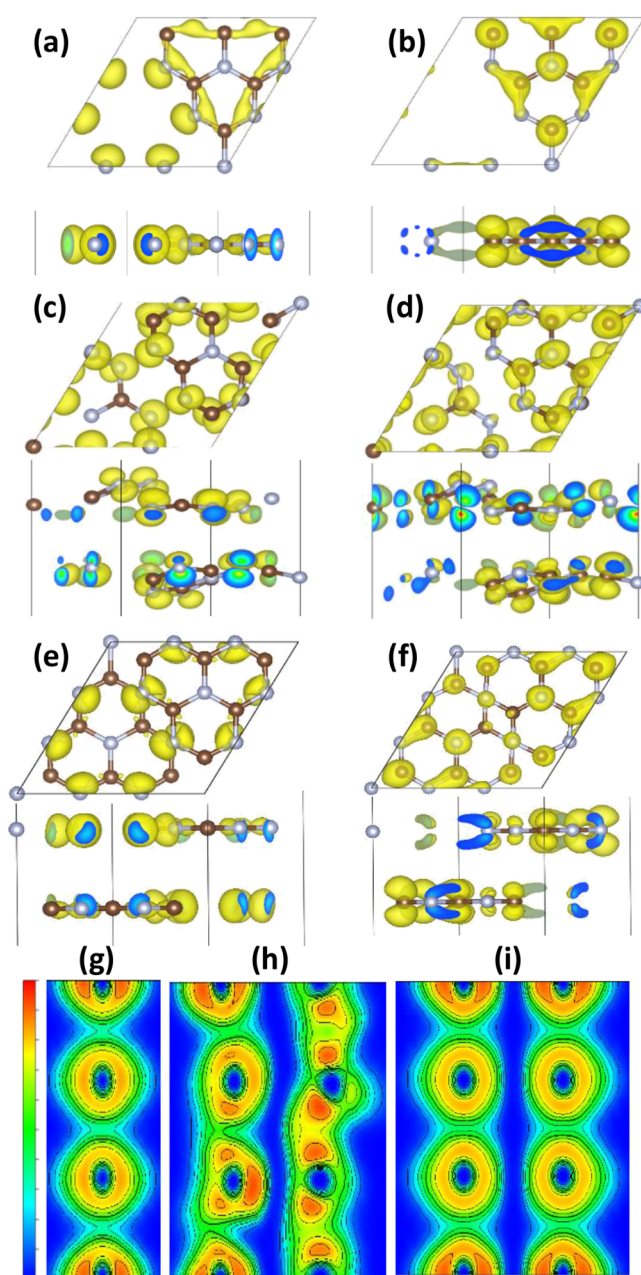


Figure 4. (a, c, e) Highest occupied molecular orbital (HOMO) and (b, d, f) lowest unoccupied molecular orbital (LUMO) top and side views and (g, h, i) 2D electron localization contour (1 0 0 plane) for ML, S_3 , and S_5 , respectively.

corrugation geometries in MLs and BLs were differentiated with bands at the K point of momentum space. In the ML, smooth small curvature bands at Γ and K points are seen, which turn into bands with a large curvature at Γ at VBM and those with a conical curvature at the K point at CBM for the BLs as a consequence of weakening or partial π -delocalization over the mesh due to formation of ridge/groove defects. The parallel bands in S_0 confirm its balanced BL geometry, whereas all other BLs through the energy difference value at a certain point in the band pair evidence the interlayer orbital interaction. Structures of Set 1 being energetically similar show a difference at VBM along the M, K, and Γ points, whereas interlayer coupling changes the indirect band gap from Γ -K to Γ -M for S_5 and S_8 as a result of a similar atom orbital

repulsion. As discussed from PDOS for band gap difference in BLs, a similar trend is seen from the band structure plot as the VBM of the planar structures is found at the higher energy and CBM toward the lower energy region, narrowing the band gap, while the corrugated structure leads to shifting of VBM toward negative energy and shifting of CBM toward higher energy, resulting in the increment of the band gap due to orbital interaction.

Along with the presence of the band gap in the visible spectrum, the role of charge carrier mobility and its recombination rate determines the photocatalytic activity of the material. Higher charge carrier mobility as a consequence of the lower effective mass ($m^* = e\tau/\mu$, m^* : effective mass, e : electronic charge, τ : collision time, and μ : carrier mobility) not only decreases the time of photoinduced e^-/h^+ pair transport within the material but also accelerates the charge displacement over the surface to avoid charge accumulation and provide a clean surface for the enhancement of redox activity. Parabolic band approximation has been used to calculate the effective mass of electrons and holes (m_e^* and m_h^*) using $m^* = \hbar^2 / [\partial^2 E(k) / \partial k^2]$, from the band structure of BLs plotted in Figure S2 and values of m_e^* and m_h^* given in Table 2 along with

Table 2. Theoretical Value of Effective Mass of Holes, Electrons, Effective Mass Ratio, and Integrated Absorption

| structure | $m_h^* (m_0)$ | $m_e^* (m_0)$ | β | absorption (10^5) |
|---|---------------|---------------|---------|-----------------------|
| g-C ₃ N ₄ -S ₀ | 0.354 | 0.173 | 0.49 | 2.92 |
| g-C ₃ N ₄ -S ₁ | 0.128 | 0.062 | 0.48 | 3.77 |
| g-C ₃ N ₄ -S ₂ | 0.127 | 0.060 | 0.47 | 3.68 |
| g-C ₃ N ₄ -S ₃ | 0.134 | 0.058 | 0.43 | 4.12 |
| g-C ₃ N ₄ -S ₄ | 0.135 | 0.074 | 0.55 | 3.85 |
| g-C ₃ N ₄ -S ₅ | 0.352 | 0.478 | 1.36 | 2.89 |
| g-C ₃ N ₄ -S ₆ | 0.139 | 0.080 | 0.58 | 3.93 |
| g-C ₃ N ₄ -S ₇ | 0.344 | 0.156 | 0.45 | 3.39 |
| g-C ₃ N ₄ -S ₈ | 0.389 | 0.174 | 0.45 | 3.45 |

the effective mass ratio ($\beta = m_e^*/m_h^*$). β also corresponds to the variance in the effective mass for the e^-/h^+ pair, where the smaller value of variance implies rapid recombination with sluggish activity and vice versa. m_e^* and m_h^* are calculated from the Γ -point of CBM and the M-point of VBM for S₅ and S₈, respectively, and from the Γ -point of CBM and the K point of VBM for MLs and rest of the BLs. The m_e^* and m_h^* values for ML, S₀, S₅, S₇, and S₈ (planar) show higher effective mass due to a small band curvature; therefore, low electron mobility and heavy holes lead to low activity, while for S₁, S₂, S₃, S₄, and S₆ (corrugated), comparatively lower effective masses point toward high photoinduced charge carrier mobility, implying its significance in enhancing the photocatalytic activity. From Table 2, the highest mobility of the e^-/h^+ pair is noticed for S₃. S₅ is an exception regarding $m_e^* > m_h^*$ as a result of the small curvature of VBM as compared to CBM and small variance. S₂, S₃, S₇, and S₈ show larger variance than ML,¹⁰ thus promoting them a step ahead for better photocatalytic activity.

In structures inculcating interlayer coupling and no π -conjugation (S₀, S₅, S₇, and S₈), a valence band similar to that of the ML is seen, while the conduction band displays lower effective mass of electrons due to the high curvature and hence rapid electron migration. Although structures show synergistic characteristics of interlayer orbital interaction and π -conjugation (S₁, S₂, S₃, S₄, and S₆), the curvature of the valence band and hence the mobility of holes increased due to

hybridization of the HOMO. A similar behavior was observed for the conduction band as a result of p_x/p_y orbital activation, as seen from Figure 3, where dominance of C-2p_x tailored the electron mobility. Hence, increasing photogenerated charge carrier mobility, their effective separation and reduce recombination rate eradicating problems related to the recovery time of electron–hole pairs. Thus, as a consequence of the low recombination rate and high electron mobility, S₃ proclaims its dominance in charge separation among all structures in the quest of efficient photocatalysts.

3.3. Optical and Photocatalytic Properties. The frequency-dependent absorption coefficient [$\alpha(\omega)$ and imaginary part $\epsilon_2(\omega)$ of complex dielectric function $\epsilon(\omega) = \epsilon_1(\omega) + i\epsilon_2(\omega)$, $\epsilon_1(\omega)$: real part] is computed and presented for the ML, S₃, and S₅ in Figure 5a,b using $\alpha(\omega) = \sqrt{2}\omega\sqrt{\epsilon_1(\omega)^2 + \epsilon_2(\omega)^2} - \epsilon_1(\omega)$ for the study of optical properties using HSE06, and the insets show the corresponding data using PBE functional. In Figure 5a, red shift of $\alpha(\omega)$ for BLs with respect to the ML (black color) implies an increase in the absorption in the visible region

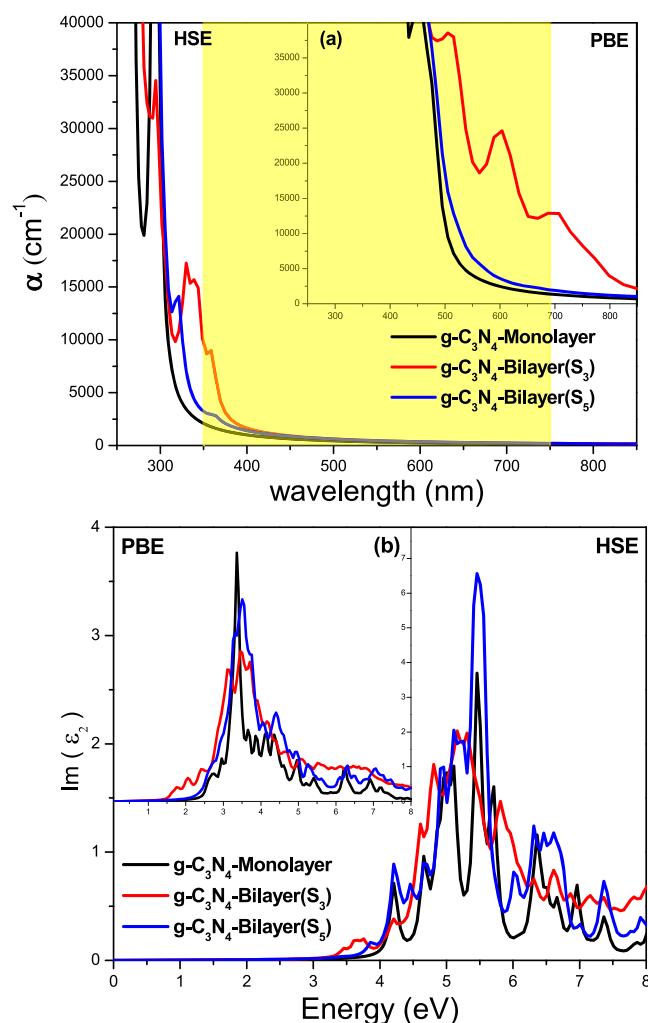


Figure 5. (a) Absorption coefficient (cm^{-1}) for the monolayer and S₃ and S₅ bilayer g-C₃N₄ (visible region shown by the yellow part) and (b) imaginary part of the dielectric function for ML, S₃, and S₅ structures using HSE06. Insets show the corresponding data using PBE–GGA.

(shaded yellow region), also confirmed by the integrated absorption values (10^5) provided in Table 2 for BLs, and for the ML, it is calculated as 2.01×10^5 . This directs us toward the application of BLs in higher visible light absorption, resulting in higher photogenerated charge carriers for high photocatalytic activity due to the activation of some forbidden dipole transition channel in the ML derived from interlayer orbital interaction. However, a huge positive difference between the absorption value of a corrugated and planar structure is the outcome of a broad peak positioned at 325 nm along the x -axis for former geometry.

Figure 5b shows that the peak corresponds to electronic transition from the top of VB dominated by occupied N_1-2p states to the bottom of CB comprising unoccupied hybrid states of N_2 ; C_1 atoms are present at 5.5 eV for ML $g-C_3N_4$. The low energy peak in the imaginary function of dielectric in S_3 and S_5 also supports the higher absorption as compared to the ML, which is due to the allowed transition from VBM to CBM in S_3 and S_5 , as shown in Figure S2, which is forbidden in the ML.^{26,27} The analysis shows the role of interlayer orbital coupling in increasing the band gap and larger absorption in the visible region, and the corrugation leads to π -delocalization further enhancing the optical property as a result of synergistic effects, while pronouncing S_3 as the best suitable structural configuration among the rest.

Overall water splitting by any photocatalyst is based on the position of band edges relevant to reduction–oxidation potential in its forbidden energy region in the visible spectrum and higher mobility of the e^-/h^+ pair with a reduced rate of recombination. For the analysis of photocatalytic activity, we have computed band edges from VBM and CBM of DOS with a correction of $E(H^+/H_2) = -4.44$ eV (reduction potential) to change the scale to the normal hydrogen electrode [NHE; $E(H^+/H_2) = 0$ V vs NHE], as depicted in Figure 6. Band edges

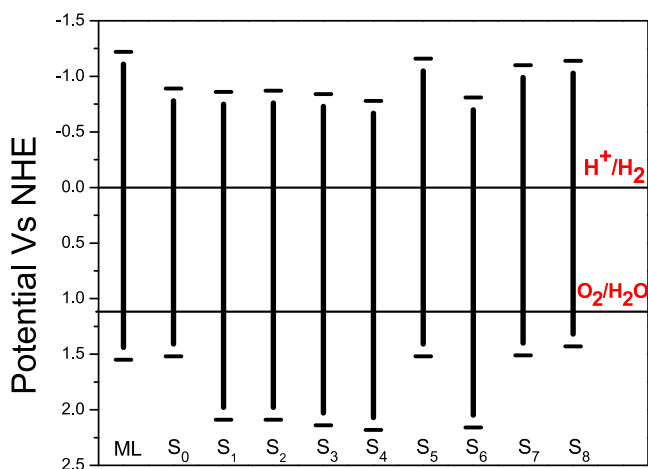


Figure 6. Valence band edge and conduction band edge for the monolayer and S_0 – S_8 bilayer $g-C_3N_4$ (with respect to NHE potential).

for all the BLs signify their potential application in overall water splitting, although an almost equal magnitude of the potential straddle redox level of water for S_1 , S_2 , S_3 , S_4 , and S_6 benefits from the lower value of E_F compared to the ML, S_0 , S_5 , S_7 , and S_8 , hence increasing their chances of crossing the prohibitive overpotential of 1.56 eV for ML $g-C_3N_4$ calculated by Wirth et al.⁷ easily as compared to the latter structures. On the basis of stability, band gap, charge separation, rate of

recombination of charge carriers, absorption in the visible region, and band edges, we find the S_3 configuration most suitable and proceed with this BL arrangement to further study the thermodynamics of OER/HER.

3.4. Surface Redox Reaction Mechanism. **3.4.1. Oxygen Evolution Reaction.** The overall water splitting study includes straddling of band edges across redox levels as a mandatory step accompanied by overpotential values within the band edges, as the narrower the overpotential ($\eta^{OER/HER}$), the better is its OER/HER activity. To compute and analyze the role of overpotential for efficient OER activity, we follow the four-electron reaction path used extensively and developed by Nørskov and co-workers.^{48,49} For OER, the essential step includes adsorption of a H_2O molecule over the substrate followed by OH, O, and OOH intermediates, which has been optimized subject to energy and force minimization and the corresponding adsorption energy has been calculated. Although in-plane π conjugation provides multiple adsorption sites on either layer, based on electronegativity seen from the HOMO–LUMO and previous work on different absorption sites over $g-C_3N_4$,⁴⁶ we have considered six different reaction sites, as shown in Figure 7. Sites A, B, C, D, E, and F correspond to positions above the void of the L_U , over the N_2 atom of the L_L , below the N_1 atom of the L_L , above the N_1 atom of the L_U (diagonally opposite to Site C), below corner carbon of the L_L , and below bay carbon of the L_U , respectively.

The adsorption of the water molecule placed at a distance of 3.42 Å above/below the corresponding layer shows a trivial change due to molecule's orientation but exhibit alignment with the H atom directed toward the edge N forming hydrogen bond except for H_2O adsorbed over Site C, which drifts away. The absorption energies (ΔE_{H_2O}) for Sites A, B, C, D, E, and F are -0.29 , -0.16 , 0.04 , -0.16 , -0.35 , and 0.038 eV, respectively, which denote physisorption, with Site C being the least preferred site. The higher energy value of ΔE_{H_2O} than the ML^{10,51} implies strong adsorption-inducing feasibility in the oncoming reaction steps due to interlayer interaction; similar results are displayed by charge transfer analysis in Table 3.

The fundamental step for OER includes conversion of H_2O into OH^* with the release of a single e^-/H^+ pair. In our case, OH^* adsorbed over the surface of the substrate chemisorbs, forming a single bond. For Sites A, B, C, and F, the O atom bonds with the C_1 atom of the corresponding layer, while for Site D, bonding takes place with the edge N atom; there is no bond formation in the case of Site E, which results in ΔE_{OH^*} values of 2.21, 2.03, 2.07, 2.05, 2.60, and 3.08 eV. The calculated value of ΔG_1 for the first step (OH^*) is lowest for Site B, indicating strong OH^* adsorption. In the second step, further removal of the ($e^- + H^+$) pair leaving isolated O^* retains its bonds with C_1 for sites A, B, C and E and the edge N atom for Sites D, and F, while huge charge transfer for Site D due to the bond formed with edge N and rapid charge distribution over a corrugated geometry weakens π -delocalization, promoting it higher on the stability scale for O^* adsorption. With the addition of the H_2O molecule, the third reaction step converts the $H_2O + O^*$ to $OOH^* + (e^- + H^+)$ via formation of the hydroxyl intermediate. Site A shows desorption of the whole molecule, while for Sites B, C, E, and F, a change in the orientation of the H atom bonded to O–O is seen, and Site D involves detachment of hydroxide due to the electronegativity difference along with strong covalent

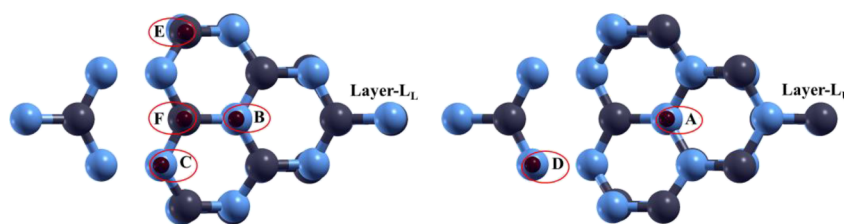


Figure 7. Six adsorption sites on either of the layer for water, hydrogen atom, and hydronium molecule at the layer. Here, blue color represents N, and gray color represents the C atom.

Table 3. Interlayer Orbital Charge Difference ($|L_U - L_L|$) for OER and HER Reaction Steps at Different Sites

| sites | | OER | | | | HER | |
|--------|-------|------------------|----------------|---------------|-----------------|---------------|------------------|
| | | $C_3N_4-S3-H_2O$ | $C_3N_4-S3-OH$ | C_3N_4-S3-O | $C_3N_4-S3-OOH$ | C_3N_4-S3-H | $C_3N_4-S3-H_3O$ |
| Site A | p_z | 0.0045 | 0.3112 | 0.3286 | 0.0064 | 0.6217 | 0.6165 |
| | p_x | 0.0652 | 0.1973 | 0.4629 | 0.0006 | 0.0396 | 0.0522 |
| | p_y | 0.0488 | 0.1391 | 0.1816 | 0.005 | 0.1094 | 0.1063 |
| Site B | p_z | 0.0073 | 0.1911 | 0.071 | 0.1875 | 0.0221 | 0.603 |
| | p_x | 0.0523 | 0.0963 | 0.244 | 0.1249 | 0.0059 | 0.0821 |
| | p_y | 0.068 | 0.1879 | 0.1707 | 0.1743 | 0.0172 | 0.0526 |
| Site C | p_z | 0.0042 | 0.2022 | 0.0381 | 0.2404 | 0.6029 | 0.6707 |
| | p_x | 0.0636 | 0.1126 | 0.2314 | 0.1054 | 0.0745 | 0.0967 |
| | p_y | 0.0584 | 0.1699 | 0.1635 | 0.1677 | 0.044 | 0.1003 |
| Site D | p_z | 0.0063 | 0.3787 | 0.0288 | 0.002 | 0.6001 | 0.6074 |
| | p_x | 0.0708 | 0.0266 | 0.0804 | 0.0549 | 0.0723 | 0.084 |
| | p_y | 0.0524 | 0.2305 | 0.2947 | 0.2192 | 0.0333 | 0.0456 |
| Site E | p_z | 0.0085 | 0.0954 | 0.1489 | 0.3398 | 0.6038 | 0.5734 |
| | p_x | 0.0052 | 0.0513 | 0.1639 | 0.2782 | 0.1279 | 0.132 |
| | p_y | 0.0159 | 0.0288 | 0.0281 | 0.1256 | 0.0131 | 0.0069 |
| Site-F | p_z | 0.0163 | 0.2032 | 0.0482 | 0.2368 | 0.4903 | 0.5936 |
| | p_x | 0.0611 | 0.1893 | 0.2409 | 0.2022 | 0.1297 | 0.0807 |
| | p_y | 0.0681 | 0.1002 | 0.1449 | 0.0855 | 0.2403 | 0.0521 |

bonding of O–N with ΔE_{OOH^*} values of 5.43, 5.85, 5.84, 6.12, 5.93, and 5.83 eV for Sites A, B, C, D, E, and F, respectively, following the quantity of electron transfer with free energy (ΔG_3). The final step involves formation of the oxygen molecule along with the ($e^- + H^+$) pair, with free energy calculated from the corresponding equation to preserve $\Delta G_{1-4} = 4.92$ eV.⁴⁸

The free energy values for all the sites are uphill at $U = 0.0$ eV, whereas the first step for Sites A, B, C, E, and F and the third step for Site D showed the maximum value of free energy change, proclaiming the respective reactions as limiting steps, and the corresponding values need to be adopted for the calculation of overpotential, as depicted from the free energy profile for different intermediates adsorbed at all four sites plotted in Figure 8, with reaction coordinates at the x -axis directing to the step number. Along with the free energy profile at $U = 0.0$ eV, we computed ΔG at equilibrium potential ($U = 1.23$ eV) and at $U = \eta^{OER} + 1.23$ eV, and it was found that $\eta_{BL}^{OER} < \eta_{ML}^{OER}$ and the exothermic nature of all the reactions was observed over four different sites at $U = \eta^{OER} + 1.23$ eV, implying their feasibility to carry the reaction forward. From the analysis, $\eta^{OER} < |E_{VB}|$ for A, B, and C sites accompanied by $\eta^{OER} < 1.56$ eV (prohibitive overpotential), which enhances their OER activity, while the lowest value of $\Delta G_1 = 2.38$ eV implies $\eta^{OER} = 1.15$ eV for Site B, which makes it the most suitable surface reaction site.

3.4.2. Hydrogen Evolution Reaction. Using the pathway of Volmer–Heyrovsky for HER illustrated by a three-step reaction beginning with $H_2O_n + H^+ + e^-$ ($n = 0$ for the single

hydrogen atom and $n = 1$ for additional water molecules) changed to an intermediate, $H_2O_n + H^*$ or H_3O^* followed by the formation of $H_2 + H_2O_n$ as final entity. Initial, and optimized structures of adsorbate over the substrate are given in Table S3. The Gibbs free energy ($|\Delta G_{H^*}|$ or $|\Delta G_{H_3O^*}|$) of the intermediate state is an important parameter of HER activity calculated using eqs 2345, and its counterpart is calculated according to the formula reported by Nørskov et al.⁵⁰ for the respective adsorbate. Although the negative value depicts the preferred adsorption site, its optimum value is considered zero. We simulated HER on the same adsorption sites as considered in the OER study, and it was found that for Sites A, C, D, and E, the H atom chemically bonds with the edge N of the respective layer with ΔE_{H^*} values of -0.44 , -0.58 , -0.51 , and -0.53 eV, respectively, showing that $|\Delta G_{H^*}| < 0.35$ eV, which is half the value of the ML, indicating weak adsorption of the H atom over the BL. However, Site B and F show $|\Delta G_{H^*}| > 3.0$ and 1.2 eV due to the confinement of the H atom over the threefold coordinated N (N_3) atom and formation of the H–C bond, thus excluding this case. Figure 9a shows the $|\Delta G_{H^*}|$ vs reaction states with Pt as reference, where Site A is found to be the best suitable site. The value of overpotential for Site A (-0.20 eV) is lower than the value reported previously by Niu et al.²⁷ due to the different BL arrangement with C–N orbital overlap, which generates access charge at the reaction site as compared to the BL with N–N orbital interaction (i.e., S5).

The role of a water molecule along with the isolated H atom is crucial to interpret the true situation considering the effect of H_2O over the H atom and their interaction in the HER

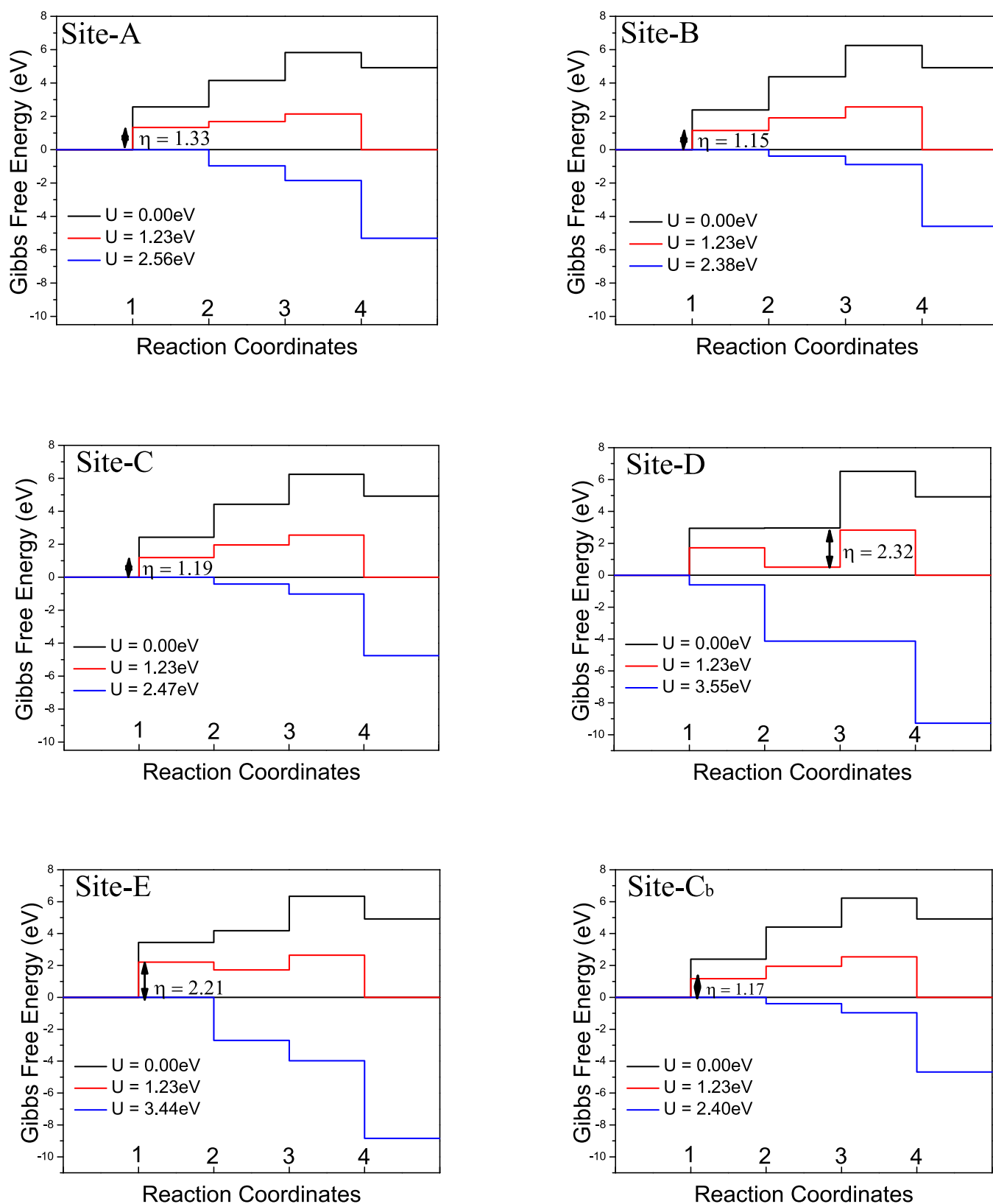


Figure 8. Free energy plots for each step of oxygen evolution reaction for six different adsorption sites (site C_b is similar to site F).

mechanism. The adsorption of H₃O* over the same sites resulted in the separation of the H atom forming H* + H₂O. For all the sites, chemisorption of H* to the twofold coordinated N atom of the respective layer is seen, while the H₂O molecule drifts away, forming the H bond with other

edge N. The presence of an extra H₂O molecule assisted chemisorption of the confined H atom over N₂ for Site B along with a decrease in the value of $|\Delta G_{H_3O^*}|$ for Sites B, C, and D but increase in that for Site A, thus making Site C energetically most favorable. However, Site D will be preferred over C, as it

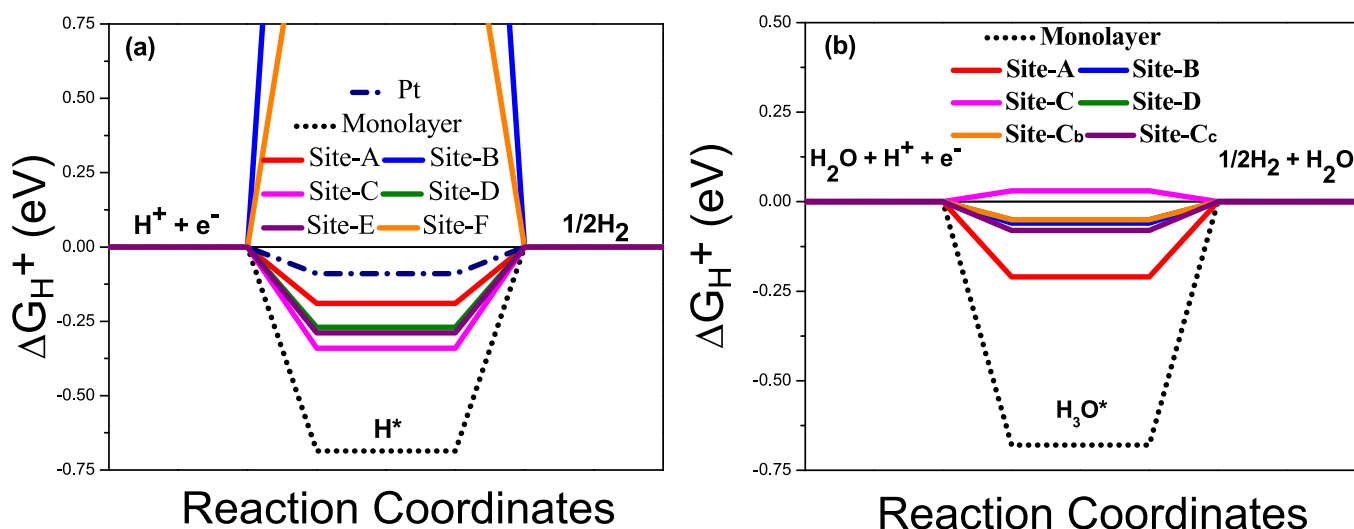


Figure 9. Gibbs free energy profile for (a) hydrogen atom adsorbed and (b) effect of an extra water molecule over the isolated H atom at different sites. Pt is reference.⁵⁰ In (b), Site C_c represents Site-E and Site C_b represents Site-F.

lies in the negative side, as seen from Figure 9b, with an overpotential value of -0.05 eV.

3.5. Role of Interlayer and Intralayer Charge Variation. Successful synthesis of BL graphene, borophene, and their different structural stacking and rotation has paved way to investigate stability-based properties of well-known MLs, where the study of electronic charge transfer has shown its capability to explain the surface reaction to understand and improve the material for required applications. Here, charge analysis of HER and OER performed over six sites has been tabulated in Table 3. It is seen that in the absence of intermediate species for OER/HER, the value of ΔQ is almost zero, while the adsorption of the intermediate on the BL creates the charge redistribution due to the change in π -delocalization of orbitals and interlayer interaction, which affects the value of free energy of the reaction. In the case of HER, the lowest adsorption energy is found for the most suitable site for HER, that is, Site A, which has the highest value of ΔQ for p_z and $(p_x + p_y)$ orbital, while in the case of the additional H_2O molecule, lowest adsorption energy is found for Site C, which also has the highest value of ΔQ for p_z and $(p_x + p_y)$. The highest value of ΔQ for the p_z orbital suggests interlayer charge redistribution, while that for $p_x + p_y$ suggests enhanced π -delocalization as compared to the other sites. A similar observation can be seen in the case of OER for the most suitable site (Site B). For the rate-determining step (with OH^* adsorption), the value of ΔQ for p_z and $(p_x + p_y)$ orbitals was found to be lowest among other considered sites. Although Sites A, D, F, and B are mentioned as the most suitable sites for the HER (H and H_3O) and OER, other sites show low values of overpotential as compared to ML $g-C_3N_4$. Thus, the synergistic effect of inter- and intralayer charge conjugation increases the surface reaction sites by creating an additional pathway of charge transfer, which was absent in the ML. This combined effect has been verified by HOMO–LUMO and LDOS by activation of p_x and p_y orbitals in the corrugated configuration and hybridization of the p_z orbital, where S_3 has proved its suitability in terms of the largest effective mass variance and optical absorption in the visible region, thereby reducing the overpotential as compared to the ML and increasing the photocatalytic efficiency.

4. CONCLUSIONS

The study of structural, electronic, optical, and photocatalytic properties of MLs and spatially tailored BLs along with reaction kinematics for the most photoactive BL (S_3) covering all the steps involved in the photocatalytic process has been carried out thoroughly and presented by means of hybrid density functional theory. Band gap tuning due to structural changes in BLs, increased spatial charge distribution, and higher electron mobility overcome the issue of π -localization in the $g-C_3N_4$ ML, while the issue of rapidly photogenerated e^-/h^+ pair recombination is resolved by S_3 configuration of the BL due to interlayer π -LP hybridization, which also increases the absorption in the visible region for BLs. Charge transfer analysis and formation of the interfacial electric field on adsorption reveal water dissociation reaction as being the limiting step for all the sites for OER and the effect of extra H_2O on decreasing the value of free energy change for highly efficient HER. With in-plane π -conjugation driven by interlayer orbital interaction, charge accumulation and dissipation at the edges strengthen the capability of reaction sites, as seen from the decrease in the adsorption energy of intermediates, which led to modification of the overpotential, with the values of -1.15 eV for OER and -0.20 eV (-0.05 eV with an additional H_2O molecule) for HER enhancing the photoactivity compared to the ML. It opens an opportunity for its application in flexible nanodevices for complete water splitting, producing hydrogen fuel even at the nanoscale.

■ ASSOCIATED CONTENT

Supporting Information

The Supporting Information is available free of charge at <https://pubs.acs.org/doi/10.1021/acs.jpcc.1c09973>.

Initial and optimized structures for all bilayers, ELF plot, density of states, band structure plots calculated using PBE for ML and BLs, and initial and optimized structures of S_3 depicting HER (H and H_3O) and OER (H_2O , OH, O, and OOH) reactions over the most suitable sites (PDF)

Animation for S_6 structure optimization (MP4)

AUTHOR INFORMATION

Corresponding Author

Alpa Dashora – Physics Department, Faculty of Science, The Maharaja Sayajirao University of Baroda, Vadodara 390002, India; orcid.org/0000-0002-7426-3917; Phone: +91-9461503962; Email: dashoralpa@gmail.com

Authors

Brajesh Rajesh Bhagat – Physics Department, Faculty of Science, The Maharaja Sayajirao University of Baroda, Vadodara 390002, India

Kishan H. Mali – Physics Department, Faculty of Science, The Maharaja Sayajirao University of Baroda, Vadodara 390002, India

Complete contact information is available at:
<https://pubs.acs.org/10.1021/acs.jpcc.1c09973>

Notes

The authors declare no competing financial interest.

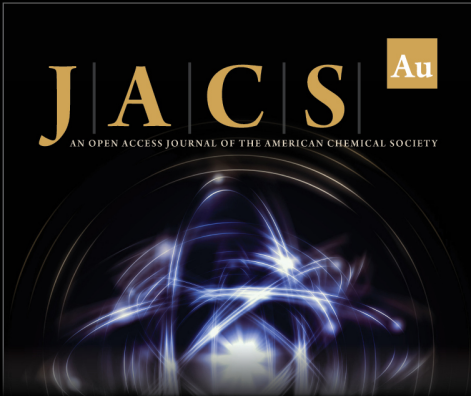
ACKNOWLEDGMENTS

The authors show their sincere gratitude to the Department of Science and Technology, India, for their DST-INSPIRE faculty project. A.D. is also thankful to University Grants Commission, India, for Assistant Professorship under Faculty Recharge Programme and start-up research grant. B.R.B. acknowledges The Maharaja Sayajirao University of Baroda for University Research Fellowship.


REFERENCES

- (1) Reshak, A. H.; Khan, S. A.; Auluck, S. Electronic band structure and specific features of AA-and AB-stacking of carbon nitride (C_3N_4): DFT calculation. *RSC Adv.* **2014**, *4*, 6957–6964.
- (2) Wei, B.; Wang, W.; Sun, J.; Mei, Q.; An, Z.; Cao, H.; Han, D.; Xie, J.; Zhan, J.; He, M. Insight into the effect of boron doping on electronic structure, photocatalytic and adsorption performance of $g-C_3N_4$ by first-principles study. *Appl. Surf. Sci.* **2020**, *511*, No. 145549.
- (3) Wang, L.; Guo, X.; Chen, Y.; Ai, S.; Ding, H. Cobalt-doped $g-C_3N_4$ as a heterogeneous catalyst for photo-assisted activation of peroxydisulfate for the degradation of organic contaminants. *Appl. Surf. Sci.* **2019**, *467–468*, 954–962.
- (4) Wang, S.; Li, C.; Wang, T.; Zhang, P.; Li, A.; Gong, J. Controllable synthesis of nanotube-type graphitic C_3N_4 and their visible-light photocatalytic and fluorescent properties. *J. Mater. Chem. A* **2014**, *2*, 2885–2890.
- (5) Wang, X.; Maeda, K.; Thomas, A.; Takanabe, K.; Xin, G.; Carlsson, J. M.; Domen, K.; Antonietti, M. A metal-free polymeric photocatalyst for hydrogen production from water under visible light. *Nat. Mater.* **2009**, *8*, 76–80.
- (6) Zhang, J.; Chen, X.; Takanabe, K.; Maeda, K.; Domen, K.; Epping, J. D.; Fu, X.; Antonietti, M.; Wang, X. Synthesis of a carbon nitride structure for visible-light catalysis by copolymerization. *Angew. Chem., Int. Ed.* **2010**, *49*, 441–444.
- (7) Wirth, J.; Neumann, R.; Antonietti, M.; Saalfrank, P. Adsorption and photocatalytic splitting of water on graphitic carbon nitride: a combined first principles and semiempirical study. *Phys. Chem. Chem. Phys.* **2014**, *16*, 15917–15926.
- (8) Azofra, L. M.; MacFarlane, D. R.; Sun, C. A DFT study of planar vs. corrugated graphene-like carbon nitride ($g-C_3N_4$) and its role in the catalytic performance of CO_2 conversion. *Phys. Chem. Chem. Phys.* **2016**, *18*, 18507–18514.
- (9) Huang, J.; Cao, Y.; Wang, H.; Yu, H.; Peng, F.; Zou, H.; Liu, Z. Revealing active-site structure of porous nitrogen-defected carbon nitride for highly effective photocatalytic hydrogen evolution. *Chem. Eng. J.* **2019**, *373*, 687–699.
- (10) Bhagat, B. R.; Dashora, A. Understanding the synergistic effect of Co-loading and B-doping in $g-C_3N_4$ for enhanced photocatalytic activity for overall solar water splitting. *Carbon* **2021**, *178*, 666–677.
- (11) Wang, L.; Hong, Y.; Liu, E.; Wang, Z.; Chen, J.; Yang, S.; Wang, J.; Lin, X.; Shi, J. Rapid polymerization synthesizing high-crystalline $g-C_3N_4$ towards boosting solar photocatalytic H_2 generation. *Int. J. Hydrogen Energy* **2020**, *45*, 6425–6436.
- (12) He, B.; Wang, Y.; Zhai, Q.; Qiu, P.; Dong, G.; Liu, X.; Chen, Y.; Li, Z. From polymeric carbon nitride to carbon materials: extended application to electrochemical energy conversion and storage. *Nanoscale* **2020**, *12*, 8636–8646.
- (13) Raziq, F.; Qu, Y.; Zhang, X.; Humayun, M.; Wu, J.; Zada, A.; Yu, H.; Sun, X.; Jing, L. Enhanced cocatalyst-free visible-light activities for photocatalytic fuel production of $g-C_3N_4$ by trapping holes and transferring electrons. *J. Phys. Chem. C* **2016**, *120*, 98–107.
- (14) Liang, D.; Jing, T.; Ma, Y.; Hao, J.; Sun, G.; Deng, M. Photocatalytic properties of $g-C_6N_6/g-C_3N_4$ heterostructure: a theoretical study. *J. Phys. Chem. C* **2016**, *120*, 24023–24029.
- (15) Zhang, L.; Zhang, X.; Lu, G. Band Alignment in Two-Dimensional Halide Perovskite Heterostructures: Type I or Type II? *J. Phys. Chem. Lett.* **2020**, *11*, 2910–2916.
- (16) Xue, Z.; Zhang, X.; Qin, J.; Liu, R. Constructing $MoS_2/g-C_3N_4$ heterojunction with enhanced oxygen evolution reaction activity: A theoretical insight. *Appl. Surf. Sci.* **2020**, *510*, No. 145489.
- (17) Thorat, N.; Yadav, A.; Yadav, M.; Gupta, S.; Varma, R.; Pillai, S.; Fernandes, R.; Patel, M.; Patel, N. Ag loaded B-doped $g-C_3N_4$ nanosheet with efficient properties for photocatalysis. *J. Environ. Manage.* **2019**, *247*, 57–66.
- (18) Thorat, N.; Borade, S.; Varma, R.; Yadav, A.; Gupta, S.; Fernandes, R.; Sarawade, P.; Bhanage, B. M.; Patel, N. High surface area Nanoflakes of $P-g-C_3N_4$ photocatalyst loaded with Ag nanoparticle with intraplanar and interplanar charge separation for environmental remediation. *J. Photochem. Photobiol., A* **2021**, *408*, No. 113098.
- (19) Wei, W.; Jacob, T. Strong excitonic effects in the optical properties of graphitic carbon nitride $g-C_3N_4$ from first principles. *Phys. Rev. B* **2013**, *87*, No. 085202.
- (20) Ma, X.; Lv, Y.; Xu, J.; Liu, Y.; Zhang, R.; Zhu, Y. A strategy of enhancing the photoactivity of $g-C_3N_4$ via doping of nonmetal elements: a first-principles study. *J. Phys. Chem. C* **2012**, *116*, 23485–23493.
- (21) Li, J.; Cui, W.; Sun, Y.; Chu, Y.; Cen, W.; Dong, F. Directional electron delivery via a vertical channel between $g-C_3N_4$ layers promotes photocatalytic efficiency. *J. Mater. Chem. A* **2017**, *5*, 9358–9364.
- (22) Xiong, T.; Cen, W.; Zhang, Y.; Dong, F. Bridging the $g-C_3N_4$ interlayers for enhanced photocatalysis. *ACS Catal.* **2016**, *6*, 2462–2472.
- (23) Ghosh, D.; Periyasamy, G.; Pati, S. K. Transition metal embedded two-dimensional C_3N_4 -graphene nanocomposite: a multi-functional material. *J. Phys. Chem. C* **2014**, *118*, 15487–15494.
- (24) Li, S.; Yang, S.; Shen, D.; Sun, W.; Shan, X.; Dong, W.; Chen, Y.; Zhang, X.; Mao, Y.; Tang, S. Polysulfide intercalation in bilayer-structured graphitic C_3N_4 : a first-principles study. *Phys. Chem. Chem. Phys.* **2017**, *19*, 32708–32714.
- (25) Gracia, J.; Kroll, P. Corrugated layered heptazine-based carbon nitride: the lowest energy modifications of C_3N_4 ground state. *J. Mater. Chem.* **2009**, *19*, 3013–3019.
- (26) Wu, F.; Liu, Y.; Yu, G.; Shen, D.; Wang, Y.; Kan, E. Visible-light-absorption in graphitic C_3N_4 bilayer: enhanced by interlayer coupling. *J. Phys. Chem. Lett.* **2012**, *3*, 3330–3334.
- (27) Niu, X.; Yi, Y.; Bai, X.; Zhang, J.; Zhou, Z.; Chu, L.; Yang, J.; Li, X. A. Photocatalytic performance of few-layer graphitic C_3N_4 : enhanced by interlayer coupling. *Nanoscale* **2019**, *11*, 4101–4107.
- (28) Wang, J.; Hao, D.; Ye, J.; Umezawa, N. Determination of crystal structure of graphitic carbon nitride: ab initio evolutionary search and experimental validation. *Chem. Mater.* **2017**, *29*, 2694–2707.


- (29) Zuluaga, S.; Liu, L. H.; Shafiq, N.; Rupich, S. M.; Veyan, J. F.; Chabal, Y. J.; Thonhauser, T. Structural band-gap tuning in g-C₃N₄. *Phys. Chem. Chem. Phys.* **2015**, *17*, 957–962.
- (30) Zhao, D.; Chen, J.; Dong, C. L.; Zhou, W.; Huang, Y. C.; Mao, S. S.; Guo, L.; Shen, S. Interlayer interaction in ultrathin nanosheets of graphitic carbon nitride for efficient photocatalytic hydrogen evolution. *J. Catal.* **2017**, *352*, 491–497.
- (31) Li, F.; Yue, X.; Zhou, H.; Fan, J.; Xiang, Q. Construction of efficient active sites through cyano-modified graphitic carbon nitride for photocatalytic CO₂ reduction. *Chinese J. Catal.* **2021**, *42*, 1608–1616.
- (32) Li, Y.; Li, X.; Zhang, H.; Fan, J.; Xiang, Q. Design and application of active sites in g-C₃N₄-based photocatalysts. *J. Mater. Sci. Technol.* **2020**, *56*, 69–88.
- (33) Li, F.; Cheng, L.; Fan, J.; Xiang, Q. Steering the behavior of photogenerated carriers in semiconductor photocatalysts: a new insight and perspective. *J. Mater. Chem. A* **2021**, *9*, 23765–23782.
- (34) Mali, K. H.; Bhagat, B. R.; Dashora, A. Tailoring electronic properties of bilayer tri-s-triazine C₃N₄ using spatial modification: An ab-initio study. *J. Phys. Conf. Ser.* **2021**, *1849*, No. 012028.
- (35) Giannozzi, P.; Baroni, S.; Bonini, N.; Calandra, M.; Car, R.; Cavazzoni, C.; Ceresoli, D.; Chiarotti, G. L.; Cococcioni, M.; Dabo, I.; Dal Corso, A.; de Gironcoli, S.; Fabris, S.; Fratesi, G.; Gebauer, R.; Gerstmann, U.; Gougoussis, C.; Kokalj, A.; Lazzeri, M.; Martin-Samos, L.; Marzari, N.; Mauri, F.; Mazzarello, R.; Paolini, S.; Pasquarello, A.; Paulatto, L.; Sbraccia, C.; Scandolo, S.; Sclauzero, G.; Seitsonen, A. P.; Smogunov, A.; Umari, P.; Wentzcovitch, R. M. QUANTUM ESPRESSO: a modular and open-source software project for quantum simulations of materials. *J. Phys.: Condens. Matter* **2009**, *21*, No. 395502.
- (36) Heyd, J.; Scuseria, G. E.; Ernzerhof, M. Hybrid functionals based on a screened Coulomb potential. *J. Chem. Phys.* **2003**, *118*, 8207.
- (37) Heyd, J.; Scuseria, G. E.; Ernzerhof, M. Erratum: “Hybrid functionals based on a screened Coulomb potential” [*J. Chem. Phys.* **2003**, *118*, 8207]. *J. Chem. Phys.* **2006**, *124*, 219906.
- (38) Perdew, J. P.; Burke, K.; Ernzerhof, M. Generalized gradient approximation made simple. *Phys. Rev. Lett.* **1996**, *77*, 3865.
- (39) Hamann, D. R.; Schlüter, M.; Chiang, C. Norm-conserving pseudopotentials. *Phys. Rev. Lett.* **1979**, *43*, 1494.
- (40) Hamann, D. R. Generalized norm-conserving pseudopotentials. *Phys. Rev. B* **1989**, *40*, 2980.
- (41) Hamann, D. R. Optimized norm-conserving Vanderbilt pseudopotentials. *Phys. Rev. B* **2013**, *88*, No. 085117.
- (42) Grimme, S. Semiempirical GGA-type density functional constructed with a long-range dispersion correction. *J. Comput. Chem.* **2006**, *27*, 1787–1799.
- (43) Monkhorst, H. J.; Pack, J. D. Special points for Brillouin-zone integrations. *Phys. Rev. B* **1976**, *13*, 5188.
- (44) Pack, J. D.; Monkhorst, H. J. “Special points for Brillouin-zone integrations”—a reply. *Phys. Rev. B* **1977**, *16*, 1748.
- (45) Kokalj, A.; Causà, M. XCrySDen:(X-Window) CRYstalline Structures and DENsities. 2001.
- (46) Aspera, S. M.; David, M.; Kasai, H. First-principles study of the adsorption of water on tri-s-triazine-based graphitic carbon nitride. *Jap. J. Appl. Phys.* **2010**, *49*, No. 115703.
- (47) Li, H.; Wu, Y.; Li, L.; Gong, Y.; Niu, L.; Liu, X.; Wang, T.; Sun, C.; Li, C. Adjustable photocatalytic ability of monolayer g-C₃N₄ utilizing single-metal atom: Density functional theory. *Appl. Surf. Sci.* **2018**, *457*, 735.
- (48) Nørskov, J. K.; Rossmeisl, J.; Logadottir, A.; Lindqvist, L. R. K. J.; Kitchin, J. R.; Bligaard, T.; Jónsson, H. Origin of the overpotential for oxygen reduction at a fuel-cell cathode. *J. Phys. Chem. B* **2004**, *108*, 17886–17892.
- (49) Rossmeisl, J.; Logadottir, A.; Nørskov, J. K. Electrolysis of water on (oxidized) metal surfaces. *Chem. Phys.* **2005**, *319*, 178–184.
- (50) Nørskov, J. K.; Bligaard, T.; Logadottir, A.; Kitchin, J. R.; Chen, J. G.; Pandelov, S.; Stimming, U. Trends in the exchange current for hydrogen evolution. *J. Electrochem. Soc.* **2005**, *152*, J23.
- (51) Zhu, B.; Zhang, L.; Cheng, B.; Yu, J. First-principle calculation study of tri-s-triazine-based g-C₃N₄: a review. *Appl. Catal. B: Environ.* **2018**, *224*, 983.
- (52) Wan, C.; Zhou, L.; Sun, L.; Xu, L.; Cheng, D. G.; Chen, F.; Zhan, X.; Yang, Y. Boosting visible-light-driven hydrogen evolution from formic acid over AgPd/2D g-C₃N₄ nanosheets Mott-Schottky photocatalyst. *Chem. Eng. J.* **2020**, *396*, No. 125229.




JACS Au
AN OPEN ACCESS JOURNAL OF THE AMERICAN CHEMICAL SOCIETY

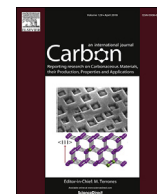


Editor-in-Chief
Prof. Christopher W. Jones
Georgia Institute of Technology, USA

Open for Submissions 

pubs.acs.org/jacsau

 **ACS Publications**
Most Trusted. Most Cited. Most Read.



Research Article

Understanding the synergistic effect of Co-loading and B-doping in g-C₃N₄ for enhanced photocatalytic activity for overall solar water splitting

B.R. Bhagat, Alpa Dashora*

Physics Department, Faculty of Science, The M.S. University of Baroda, Vadodra, 390002, India



ARTICLE INFO

Article history:

Received 5 January 2021

Received in revised form

15 March 2021

Accepted 24 March 2021

Available online 30 March 2021

Keywords:

Heptazine-C₃N₄

Density functional theory

Overall solar water splitting

OER

HER

ABSTRACT

An effective approach of loading of metal (Co) and doping of non-metal (B) together has been considered to enhance the photocatalytic activity of tri-s-triazine based g-C₃N₄. Here, pristine and functionalized g-C₃N₄ with B-doping at bay C site (B_{C1}-C₃N₄), corner C site (B_{C2}-C₃N₄), Co-loading (Co-C₃N₄) and Co-loading and B-doping together [(Co-B)_{C1}-C₃N₄ and (Co-B)_{C2}-C₃N₄] have been studied for structural, electronic, optical and photocatalytic properties using hybrid density functional theory. B-doping in g-C₃N₄ formed p-type semiconductor while Co-loading revealed formation of n-type semiconductor with formation of Co-3d intermediate states while both together indicated partial charge compensation. All the functionalized films show lower overpotential value for oxygen evolution reaction (OER) as compared to g-C₃N₄ while for hydrogen evolution reaction (HER) lower overpotential values are obtained for Co-C₃N₄, (Co-B)_{C1}-C₃N₄ and (Co-B)_{C2}-C₃N₄. The present work, highlights the synergistic effects of Co-loading and B-doping in g-C₃N₄ in terms of formation of impurity states, high absorption, charge redistribution and lower OER and HER overpotential along with suitable redox potentials than g-C₃N₄ and suggests (Co-B)_{C1}-C₃N₄ as potential candidate for overall photocatalytic water splitting.

© 2021 Elsevier Ltd. All rights reserved.

1. Introduction

The requirement of current scenario guides us to use renewable energy resources efficiently. Insight about the future energy crisis, abundance of solar energy and search for hazard free materials lead us to study efficient, low cost and ecofriendly photocatalyst material which fits perfect in the situation resolving the future energy problems. After the conversion of graphite in thin layers, the technique opened multiple pathways in the application of various materials in their low dimensional forms. Recently, various 2D-sheet structures have attracted significant attention from the scientific community because of their easy synthesis processes and various unusual properties. Numerous 2D-sheet materials such as graphene [1,2], hexagonal boron nitride [3,4], molybdenum disulphide [5,6], manganese dioxide [7] and graphitic carbon nitride (g-C₃N₄) [8–11] have already been explored systematically. Materials for the promising photocatalytic properties have to be screened on the basis of their band gap compatibility towards

visible light spectrum, and have to be selected on the basis of materials which are abundant in nature and less hazardous to living organisms. Due to promising electronic and optical performances with suitable band gap of 2.70 eV g-C₃N₄ has been studied widely [12–15]. With excellent chemical and thermal stability g-C₃N₄ is also considered as promising metal-free photocatalyst for a series of photocatalytic redox reactions like water splitting [16,17], organic pollutant degradation [18–20] and oxidative dehydrogenation of amines [21]. However, the shortcomings of g-C₃N₄ have restricted its practical applications, which include small specific surface area, low visible light response and rapid photogenerated e⁻/h⁺ pair recombination [22].

In recent years, lots of strategies have been proved to improve the photocatalytic ability of g-C₃N₄, such as depositing noble-metal [23], compositing semiconductor [24,25], engineering nano-structure [26,27] and doping of metal and non-metal atoms [28–30]. Nano-sheets of g-C₃N₄ are reported for enhanced intrinsic photo-absorption, and the photoluminescence quantum yield have improved up to 19.6% [31]. Interstitial doping of non-metals like S and P in g-C₃N₄ enhanced the absorption in visible energy region due to the alteration of the topology and connectivity pattern of g-

* Corresponding author.

E-mail address: dashoralpa@gmail.com (A. Dashora).

C₃N₄ sheets [32]. Lu et al. [33] studied that the HOMO and LUMO of H-, B-, O-, S-, F- and As-doped g-C₃N₄ effectively separate the photogenerated e⁻/h⁺ pairs and enhanced the photocatalytic efficiency. B-doping enhanced the visible-light response of g-C₃N₄ by replacing the C atom in the ring and also formed impurity states near the top of the valence band [34]. The effects of B-doping in g-C₃N₄ prolonged the lifetime of photogenerated charge carriers which is beneficial for increasing photocatalytic activity for H₂ evolution and CO₂ conversion [35]. Co-doped g-C₃N₄ has enhanced the photocatalytic properties because of formation of Co–N bond [36] and also reported as promising catalyst in the photo-assisted degradation of sulfate radicals based organic materials [37], whereas when Fe and Ni are loaded on g-C₃N₄, they penetrated into void present in g-C₃N₄ and extended the charge carrier migration distance which suppressed the recombination of e⁻-h⁺ pairs while on the other hand Cu and Zn contributes in inter-layer charge carrier migration [38]. Ling et al. [39] performed the doping of S atom or C/N-vacancy in g-C₃N₄ and reported the enhancement in light response by narrowing the band-gap or creating gap states, while the coupling effect at interface of g-C₃N₄/MoS₂ is able to tune the band edge potentials of g-C₃N₄. Zhao et al. [40] have studied the photocatalytic mechanism of F and Ti co-doped heptazine based g-C₃N₄ heterostructure using hybrid density functional theory (h-DFT).

Various attempts have made to overcome the issue of high oxidation overpotential of 1.56 eV [17] in g-C₃N₄ which includes different doping, loading and formation of heterostructure. However, the lack of study on synergistic effects of various non-metal doping and TM loading attracted our attention towards the functionalization of g-C₃N₄ with non-metal doping and TM loading. For the efficient photocatalyst, choice of non-metal and TM is very important. For the selection of non-metal and TM to functionalize the g-C₃N₄, B and Co have attracted our attention. As, in recent years, TM based borides have gained huge interest [41] among which Co–B compounds are reported as efficient electrocatalyst for HER [42]. Co and B co-doping is also found promising to increase the photocatalytic degradation rate of organic aqueous pollutants (p-nitrophenol and Rhodamine B dye) in TiO₂ [43]. Therefore, the synergistic effect from B-doping and Co-loading in g-C₃N₄ can also enhance the overall water splitting potential.

Current work focused on Co-loaded and B-doped g-C₃N₄ using density functional theory (DFT) in terms of band gap reduction, enhancement in visible light absorption, charge redistribution and separation along with the thermodynamical studies of water splitting reactions (HER and OER). For the present study, Co atom was embedded in the void of g-C₃N₄ while two different sites for B doping were considered. Two different interaction scenario (short range and long range) for Co and B were studied. The role of Co-loading and B-doping in g-C₃N₄ for efficient photocatalytic material is explained on the basis of increment in charge carrier generation, reduction in their rate of recombination and charge redistribution over the surface of g-C₃N₄ which create the active site.

2. Computational details

2.1. Methods

Structural, electronic, optical and thermodynamic properties were studied using DFT as embodied in QUANTUM ESPRESSO [44] package. For structural design and visualization VESTA [45], XCrySDen [46] and BURAI [47] software were used. The structural optimization, energy band structure calculations, optical and thermodynamic property were calculated using generalized

gradient approximation (GGA) of Perdew et al. [48] referred as GGA-PBE, while hybrid functional HSE06 [49,50] was considered for the calculation of density of states (DOS) only, which gives better energy gap value than GGA-PBE calculation. The HSE06 functional is obtained by combination of the semi local GGA/LDA exchange potential with an exact Hartree-Fock (HF) exchange energy additionally, given by

$$E_{xc}^{HSE} = \alpha E_x^{HF,SR}(\omega) + (1 - \alpha) E_x^{PBE,SR}(\omega) + E_x^{PBE,LR}(\omega) + E_c^{PBE}(\omega) \quad [1]$$

In this functional the coulomb operator is separated into short-ranged (SR) and long ranged (LR) parts for which the short-range exchange fraction (α) is set to 0.25, where ω is a parameter controlling the extent of short-range interactions, necessarily chosen $\omega < 0.15 \text{ a}_0^{-1}$. In the present case the value of ω is considered as 0.012 a_0^{-1} for reliable values of energy gap in semiconducting solids. For the computation of optical properties, we have considered the norm-conserving pseudo-potentials (ONCV) whereas ultra-soft pseudo-potentials (USPP) for other properties. Total energies were corrected for van der Waals (vdW) interaction by employing Grimme-D2 [51] scheme. A $5 \times 5 \times 1$ Monkhorst-Pack \mathbf{k} -point grid was used for all the calculations. Charge densities and the Kohn-Sham [52,53] orbitals are represented using plane waves based basis sets consisting up to a maximal kinetic energy of 540 and 60 Ry, respectively which were determined by observing the convergence of the total energy with the increase in plane wave kinetic energy. Convergence threshold was fixed to be 10^{-6} Ry. Structural parameters were optimized by quasi-Newton ionic relaxation using the Broyden, Fletcher, Goldfarb, Shanno (BFGS) [54–57] algorithm.

2.2. Structural models

Among all the different forms of C₃N₄, hexagonal heptazine-based g-C₃N₄ is reported as the most stable form [58]. Here, we created a unit cell of heptazine g-C₃N₄ with lattice parameter 7.14 Å, with pore (radius of 1.18 Å) and void (radius of 2.38 Å). We extended the cell in x and y directions creating $2 \times 2 \times 1$ supercell which generates the monolayer of g-C₃N₄ with a vacuum of 15 Å (which was found most suitable after considering different vacuum size on the basis of saturation in total energy) in the z direction of the cell to avoid the interaction with next periodic layer. This supercell contains 24C and 32 N atoms summing to total 56 atoms as presented in Fig. 1. Single C atom was substituted by B atom at either bay (C₁) or at corner (C₂) site resulting 4.16% doping at C site referred as B_{C1}–C₃N₄ and B_{C2}–C₃N₄, respectively. A single atom of Co was embedded in the void of the g-C₃N₄ with 1.78% concentration (referred as Co–C₃N₄). While for loading and doping together, we have considered two B-doping sites (at C₁ and C₂) with Co-loading which formed two different structure further referred as (Co–B)_{C1}–C₃N₄ and (Co–B)_{C2}–C₃N₄, respectively. For the structural stability we have calculated the bonding energy (ΔE_b) for all the systems after loading, doping and with both using

$$\Delta E_b = E_{C_3N_4+Co+B} - (E_{C_3N_4} - \mu_{Co} - \mu_B + \mu_C) \quad [2]$$

Where $E_{C_3N_4+Co+B}$ and $E_{C_3N_4}$ are total energy of loading/doping and pristine samples, respectively while μ_{Co} , μ_B , μ_C denotes the chemical potential of Co, B and C computed from their bulk or compound form. For thermodynamic properties, the adsorption of intermediate over the surface was performed on the unit cell since the periodicity and smaller doping and loading concentration provide a similar chemical environment as that of supercell [17].

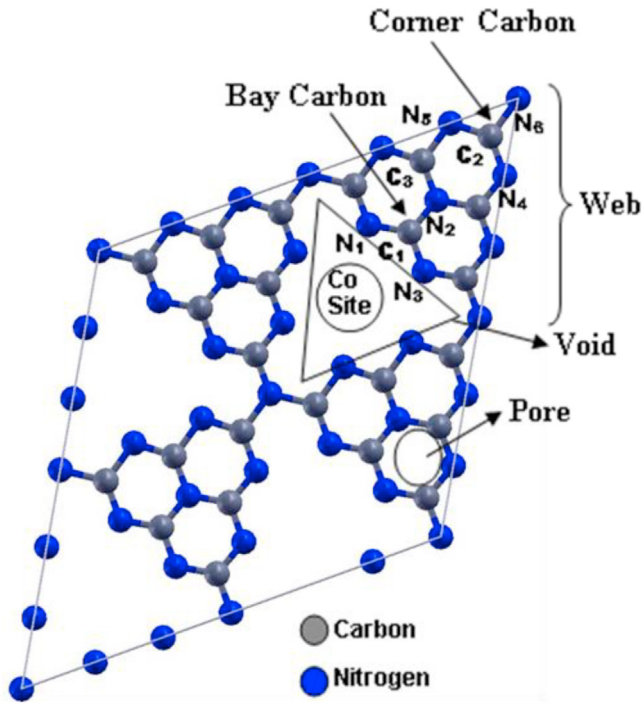


Fig. 1. Monolayer of g-C₃N₄ with active sites for B doping and Co loading. (A colour version of this figure can be viewed online.)

2.3. Thermodynamics

The adsorption energy (ΔE_{Ads}) for any adsorbate species over the substrate surface is calculated as the energy difference

$$\Delta E_{\text{Ads}} = E_{\text{sub+A}} - (E_{\text{sub}} + E_{\text{A}}), \quad [3]$$

with $E_{\text{sub+A}}$, E_{sub} and E_{A} indicating total energy of “substrate + adsorbate”, substrate and adsorbate, respectively. For error elimination, same computational settings were applied to all species involved.

For water and intermediates (OH^* , O^* , OOH^*) over the g-C₃N₄ surface, adsorption energies were calculated as follows:

$$\Delta E_{\text{H}_2\text{O}} = E_{\text{C}_3\text{N}_4+\text{H}_2\text{O}} - (E_{\text{C}_3\text{N}_4} + E_{\text{H}_2\text{O}}) \quad [4]$$

$$\Delta E_{\text{OH}^*} = E_{\text{C}_3\text{N}_4+\text{OH}} - E_{\text{C}_3\text{N}_4} - (E_{\text{H}_2\text{O}} - 1/2E_{\text{H}_2}) \quad [5]$$

$$\Delta E_{\text{O}^*} = E_{\text{C}_3\text{N}_4+\text{O}} - E_{\text{C}_3\text{N}_4} - (E_{\text{H}_2\text{O}} - E_{\text{H}_2}) \quad [6]$$

$$\Delta E_{\text{OOH}^*} = E_{\text{C}_3\text{N}_4+\text{OOH}} - E_{\text{C}_3\text{N}_4} - (2 \times E_{\text{H}_2\text{O}} - 3/2E_{\text{H}_2}) \quad [7]$$

$E_{\text{C}_3\text{N}_4+\text{H}_2\text{O}}$, $E_{\text{C}_3\text{N}_4+\text{OH}}$, $E_{\text{C}_3\text{N}_4+\text{O}}$ and $E_{\text{C}_3\text{N}_4+\text{OOH}}$ represent the total ground state energy of H₂O, OH*, O* and OOH* intermediates on substrate, respectively; $E_{\text{C}_3\text{N}_4}$, $E_{\text{H}_2\text{O}}$ and E_{H_2} are the total ground state energy of bare substrate, water molecule and hydrogen molecule, respectively.

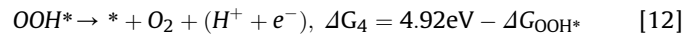
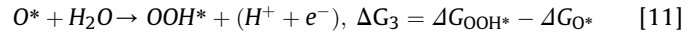
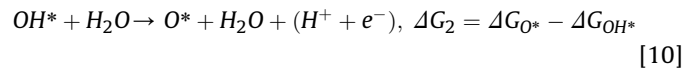
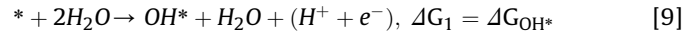
Change in Gibbs free energy (ΔG) for each adsorption reaction is evaluated as follows:

$$\Delta G = \Delta E + \Delta \text{ZPE} - T\Delta S + \Delta G_{\text{U}} + \Delta G_{\text{pH}} \quad [8]$$

Here, ΔE is the total energy change evaluated from DFT study, ΔZPE is the change in zero-point energies, T is temperature, ΔS is the entropy change, $\Delta G_{\text{U}} = -eU$ (U is the potential measured against

NHE) and $\Delta G_{\text{pH}} = -k_{\text{B}}T \ln(10) \times \text{pH}$. We have calculated ΔG at pH = 0. The calculation of free energy change in the oxidation/reduction reaction is done using the method developed by Nørskov et al. [59].

The chemical reaction describing OER for water splitting is divided into four one-electron transfer step [60].



Where, * represents the active site on the monolayer. Since the energies of H₂O and H₂ in gas phase are well described therefore they were taken as the reference states, on the other hand because of complicated electronic structure of O₂ which cannot be accurately described by DFT, we have taken sum of energies as $\Delta G_{1-4} = 4.92$ eV which is equal to negative experimental Gibbs free energy formation of two water molecule ($2\text{H}_2\text{O} \rightarrow \text{O}_2 + \text{H}_2$) [59].

The step which has maximum energy change is the rate determining step, the theoretical overpotential of OER is calculated as:

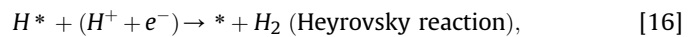
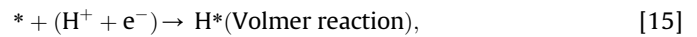
$$\Delta \eta^{\text{OER}} = \text{Max}_i[\Delta G_i] - 1.23 \text{ V (where } i \text{ denote intermediate)} \quad [13]$$

Adsorption energy of H atom on g-C₃N₄ is calculated by:

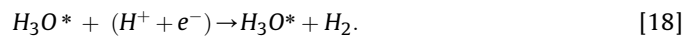
$$\Delta E_{\text{H}^*} = E_{\text{C}_3\text{N}_4+\text{H}} - E_{\text{C}_3\text{N}_4} - 1/2E_{\text{H}_2} \quad [14]$$

Where $E_{\text{C}_3\text{N}_4+\text{H}}$ denotes the total ground state energy of H atom on g-C₃N₄.

The HER of water splitting is described as:



and with the involvement of additional water molecule following the same reaction mechanisms:



The entropy of H atom is much less than the entropy in the gas phase (H₂). Therefore, the entropy capacity is determined with the entropy of H₂ gas at standard condition, since the ZPE and entropy are not sensitive to the coverage [61]. The overall correction to the equation proposed by Nørskov et al. ($\Delta G_{\text{H}^*} = \Delta E_{\text{H}^*} + 0.24$) [62] and Zhu et al. [63] is

$$\Delta G_{\text{H}^*} = \Delta E_{\text{H}^*} + 0.35 \quad [19]$$

$$\Delta \eta^{\text{HER}} = [\Delta G_{\text{H}^*}]V, \quad [20]$$

Where $\Delta \eta^{\text{HER}}$ is overpotential of HER and we have considered Eq. (19) for the calculation of ΔG_{H^*} due to the larger ZPE of g-C₃N₄ [63], similar corrections are followed for the calculation in case of an extra water molecule (H₃O*).

3. Results and discussion

3.1. Structural properties

Fig. 1 represents the crystal structure of monolayer of g- C_3N_4 with 5 substitutional doping sites i.e., N_1 , N_2 , N_6 , C_1 and C_2 . Here N_1 is tri-bonded N positioned at center of web, N_6 bridging three s-triazine molecules and N_2 is double bonded atom present at edge of the web. C_1 and C_2 are triple bonded atoms at bay site of the web and at corner of the web, respectively. For the present calculations, we have loaded Co atom at the void named as “Co Site” in Fig. 1. For B-doping, different sites were checked for the stability. In terms of substitutional doping of B atom, most stable site was found at C atom as compared to N atom due to presence of single electron in 2p orbital of B and electronegative nature of N. Among the different C sites, we have considered both C_1 and C_2 sites for B-doping and we found energy difference of (≈ 0.35 eV) between them, also reported by Huang et al. [64] and Ghashghaee et al. [65] whereas for Co-loading with B-doping energy difference of 0.28 eV was computed, for B-doping C_2 site was found energetically more stable but for B-doping with Co-loading C_1 site is most stable. The bonding energy calculated for $\text{B}_{\text{C}_1}-\text{C}_3\text{N}_4$, $\text{B}_{\text{C}_2}-\text{C}_3\text{N}_4$, $\text{Co}-\text{C}_3\text{N}_4$, $(\text{Co}-\text{B})_{\text{C}_1}-\text{C}_3\text{N}_4$ and $(\text{Co}-\text{B})_{\text{C}_2}-\text{C}_3\text{N}_4$ are -1.22 , -1.57 , 1.98 , -0.63 and -0.35 eV where the negative value indicates exothermic and spontaneous routes while the lower value of ΔE_b shows the easy incorporation of impurity atoms in the supercell. All optimized structures are presented in Fig. S1 not showing any distortion in planer geometry (z direction) due to the presence of van der Waals interaction. It is seen that the Co loading in the void leads to its displacement towards the corner of the triangular void and form bond with two edge N atoms, after the optimization.

The optimized lattice parameter for g- C_3N_4 was calculated as $a = b = 14.25$ Å which is in accordance with the reported value of lattice parameter for unit-cell [58]. This optimized parameter was used for the further calculation of the functionalized g- C_3N_4 . The lattice parameters for $\text{B}_{\text{C}_1}-\text{C}_3\text{N}_4$ and $\text{B}_{\text{C}_2}-\text{C}_3\text{N}_4$ were obtained as $a = b = 14.23$ Å and $a = b = 14.30$ Å, respectively. The calculated lattice parameter for $\text{Co}-\text{C}_3\text{N}_4$, $(\text{Co}-\text{B})_{\text{C}_1}-\text{C}_3\text{N}_4$ and $(\text{Co}-\text{B})_{\text{C}_2}-\text{C}_3\text{N}_4$ are obtained as $a = b = 14.22$, 14.24 and 14.31 Å, respectively.

3.2. Electronic properties

The density of states (DOS) studied using HSE06 for g- C_3N_4 , $\text{B}_{\text{C}_1}-\text{C}_3\text{N}_4$, $\text{B}_{\text{C}_2}-\text{C}_3\text{N}_4$, $\text{Co}-\text{C}_3\text{N}_4$, $(\text{Co}-\text{B})_{\text{C}_1}-\text{C}_3\text{N}_4$ and $(\text{Co}-\text{B})_{\text{C}_2}-\text{C}_3\text{N}_4$, are presented in Fig. 2. Value of band gap for pristine g- C_3N_4 is calculated as 2.76 eV which is in accordance with experimental values 2.78 eV and 2.67 eV [66,67]. For $\text{B}_{\text{C}_1}-\text{C}_3\text{N}_4$ and $\text{B}_{\text{C}_2}-\text{C}_3\text{N}_4$ the band gap reduced to 1.76 eV and 2.21 eV, respectively and Fermi energy (E_F) is shifted towards the valence band (VB) forming p-type semiconductor. In case of $\text{Co}-\text{C}_3\text{N}_4$, a broad intermediate band (IB) is formed in the forbidden band gap region of g- C_3N_4 inferring to formation of deep levels for charge carriers and E_F is shifted toward the conduction band (CB) implying its n-type semiconductor nature. In case of $(\text{Co}-\text{B})_{\text{C}_1}-\text{C}_3\text{N}_4$ and $(\text{Co}-\text{B})_{\text{C}_2}-\text{C}_3\text{N}_4$, E_F is shifted in the middle of the band gap and suggests Co-loading and B-doping together for partial charge compensation in g- C_3N_4 . Co-loading and B-doping together also formed completely filled impurity states well separated from the lower VB.

To understand the orbital contribution in total DOS, partial DOS (PDOS) for all the studied monolayer are presented in Fig. 3(a–f). In g- C_3N_4 (Fig. 3a), VB is mainly dominated by the N_1 -2p states while the CB is formed due to the hybridization between N_2 -2p and C_1 and C_2 -2p states. Shaded DOS in Fig. 3 (a) represents the contribution of N-2s orbitals which is very small as compared to the 2p orbitals of N and C. The PDOS of $\text{B}_{\text{C}_1}-\text{C}_3\text{N}_4$ and $\text{B}_{\text{C}_2}-\text{C}_3\text{N}_4$ in Fig. 3(b

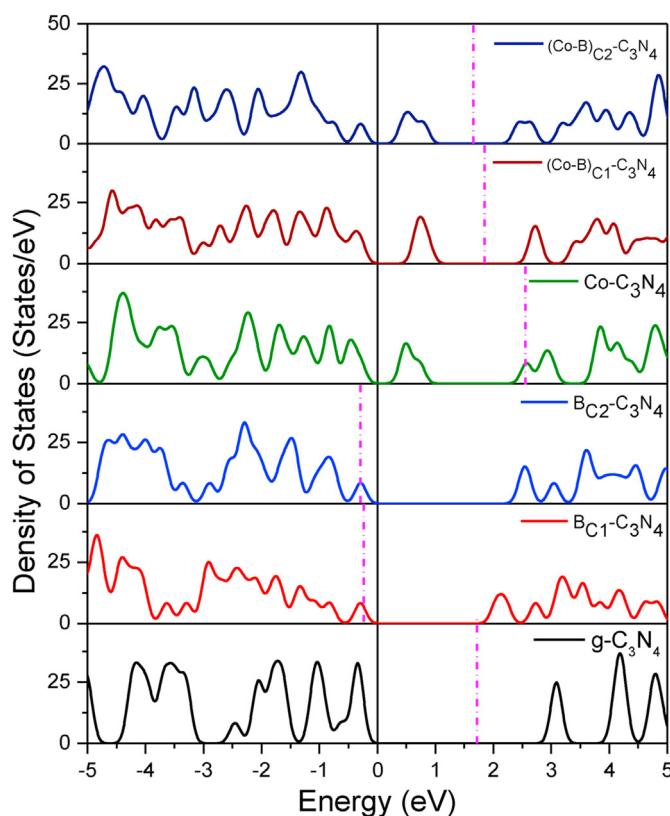


Fig. 2. The density of states for (from bottom) pristine g- C_3N_4 , $\text{B}_{\text{C}_1}-\text{C}_3\text{N}_4$, $\text{B}_{\text{C}_2}-\text{C}_3\text{N}_4$, $\text{Co}-\text{C}_3\text{N}_4$, $(\text{Co}-\text{B})_{\text{C}_1}-\text{C}_3\text{N}_4$ and $(\text{Co}-\text{B})_{\text{C}_2}-\text{C}_3\text{N}_4$. Here, zero-energy (eV) shows highest occupied energy states of C-2p and N-2p and Fermi energy (E_F) is marked by dotted line. (A colour version of this figure can be viewed online.)

and c) show the shifting of E_F towards the VB and CB is dominated due to the formation of impurity state of B-2p at 2.5 eV and 2.75 eV, respectively while VB comprise of N_3 -2p and N_5 -2p states corresponding to the neighbor N atoms of B. After introducing B in g- C_3N_4 , B-2p states hybridize with the N-2p states, and C-2p and N-2p states have been altered in both CB and VB mainly due to the formation of new N–B bonds and the varying interactions between C-2p and N-2p states in C–N bonds in the mesh. Whereas for $\text{Co}-\text{C}_3\text{N}_4$ (Fig. 3d) formation of Co-3d impurity states between -2.5 and -1.5 eV above the VB region is observed. Small isolated DOS of N-2p states and C-2p states are also seen in this region and hybridizing with the Co-3d states. The hybridization between Co-3d and N-2p states in CB shows some direct or indirect interaction with Co which can be understood on the basis of charge transfer (will be discussed in the next section). In case of $(\text{Co}-\text{B})_{\text{C}_1}-\text{C}_3\text{N}_4$ (Fig. 3e), the isolated DOS between -1.5 and -0.75 eV sharpen as compared to $\text{Co}-\text{C}_3\text{N}_4$ mainly due to the additional B-2p states in same energy region. But the orbital hybridization formed intense isolated DOS at top of the VB. E_F is shifted between the hybridized intermediate states of Co-3d and B-2p in the VB and CB, respectively. These impurity states can be responsible for higher absorption in the low energy region and can also work as deep trapping sites for charge carriers. For $(\text{Co}-\text{B})_{\text{C}_2}-\text{C}_3\text{N}_4$ (Fig. 3f) the formed impurity states are wider than $(\text{Co}-\text{B})_{\text{C}_1}-\text{C}_3\text{N}_4$.

3.3. Charge separation

The diffusion rate and separation of photo-generated charge carriers are essential factors to determine the photocatalytic activity of a semiconductor. The higher carrier mobility means lighter

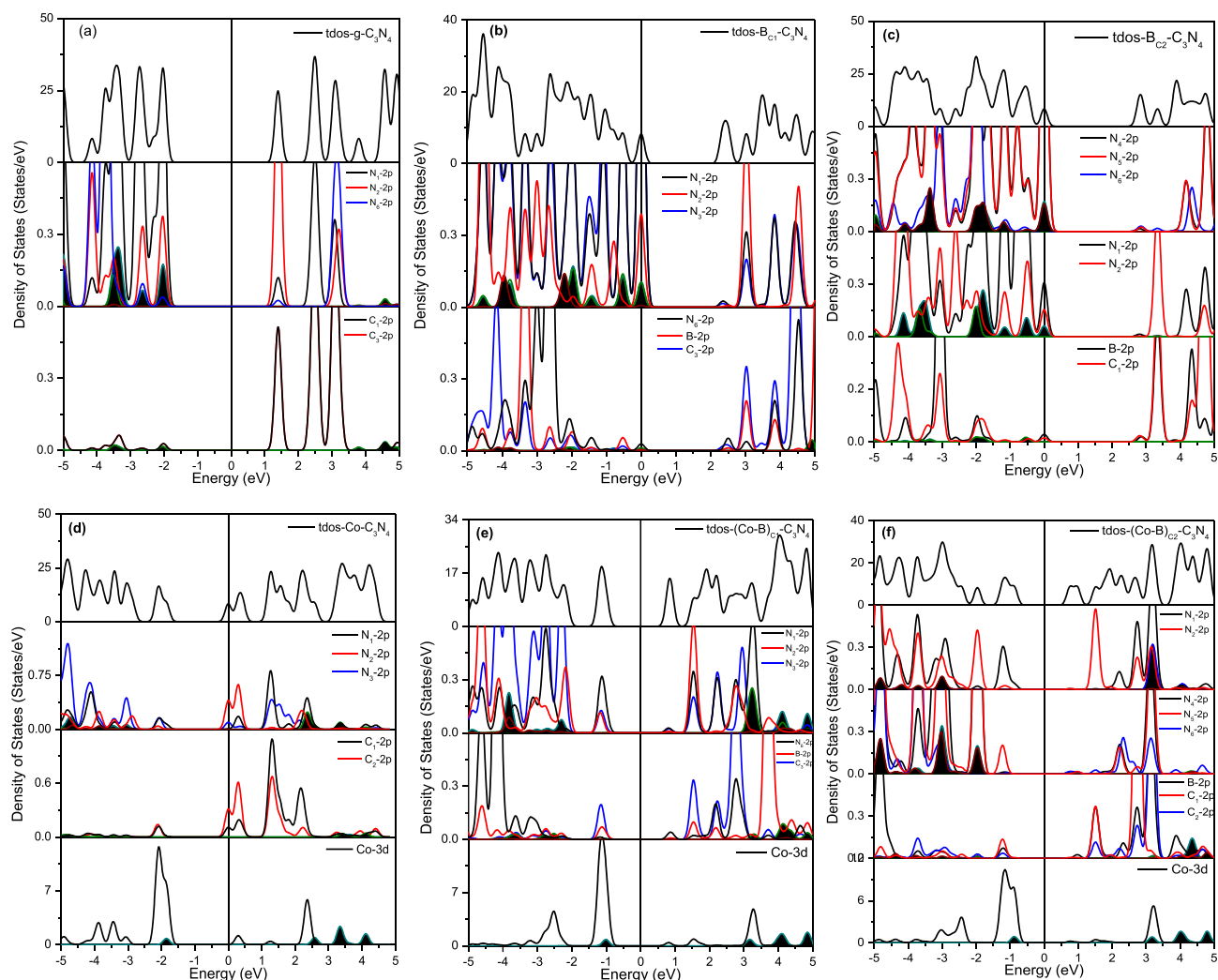


Fig. 3. The PDOS for (a) pristine $g\text{-C}_3\text{N}_4$, (b) $\text{B}_{\text{C1}}\text{-C}_3\text{N}_4$, (c) $\text{B}_{\text{C2}}\text{-C}_3\text{N}_4$, (d) $\text{Co-C}_3\text{N}_4$, (e) $(\text{Co-B})_{\text{C1}}\text{-C}_3\text{N}_4$ and (f) $(\text{Co-B})_{\text{C2}}\text{-C}_3\text{N}_4$. E_F is denoted at zero energy. Shaded region represents the s-orbital of respective atom. (A colour version of this figure can be viewed online.)

effective mass of the photo-generated carriers hence more probability of reaching the surface reaction sites within their life-time leading to improvement of the photo-assisted activity. The effective mass (m^*) is calculated considering the curvature of the energy band diagrams calculated using GGA [48] as shown in Fig. S2. Effective mass of the charge carrier is defined as:

$$m^* = \hbar^2 \left[\frac{\partial^2 E(k)}{\partial k^2} \right]^{-1} \quad [21]$$

Where, $E(k)$ is the energy of the VBM for holes and the CBM for electrons. The mobility of charge carriers is inversely proportional to their effective mass.

The relative ratio of effective mass ($\beta = m_e^*/m_h^*$, m_e^* and m_h^* are effective mass of electron and hole, respectively) is one of the key parameter to determine the rate of recombination of e^-h^+ pairs which also plays major role in separation of charge carriers. A larger or smaller value of effective mass ratio than one suggests greater difference in the e^-h^+ mobility and thus a lower recombination rate which suggests their availability for redox reactions over the surface for wider time range thus higher photocatalytic activity [68, 69].

For the effective mass calculations, the average of the band curvature was considered whereas for the sample with intermediate band (IB) the transition from VB to CB, VB to IB and from IB to CB was evaluated and the average value was analyzed further as collated in Table 1. The value of m_e^* are calculated as 1.55, 2.47 and 1.38 m_e (m_e is the mass of free e^-) for $g\text{-C}_3\text{N}_4$, $\text{B}_{\text{C1}}\text{-C}_3\text{N}_4$ and $\text{B}_{\text{C2}}\text{-C}_3\text{N}_4$, respectively, with lowest value of m_e^* $\text{B}_{\text{C2}}\text{-C}_3\text{N}_4$ shows highest mobility of e^- . For $\text{Co-C}_3\text{N}_4$, $(\text{Co-B})_{\text{C1}}\text{-C}_3\text{N}_4$ and $(\text{Co-B})_{\text{C2}}\text{-C}_3\text{N}_4$, IB/impurity states are formed which acts as a meta-stable level for charge carriers before they jump on to CB. These can act as a trapping site to reduce the recombination rate of e^-h^+ pair. Highest value of β for $(\text{Co-B})_{\text{C1}}\text{-C}_3\text{N}_4$ suggested the lowest recombination of charge carrier in the impurity states as compared to $\text{Co-C}_3\text{N}_4$ and $(\text{Co-B})_{\text{C2}}\text{-C}_3\text{N}_4$ suggesting $(\text{Co-B})_{\text{C1}}\text{-C}_3\text{N}_4$ as most suitable material for the charge carrier separation.

3.4. Charge redistribution

To study the effect of B-doping and Co-loading due to electronic charge in the $g\text{-C}_3\text{N}_4$ monolayer, we have briefly analyzed the Löwdin charge transfer on each atom of the cell and charge transfer on few selected atoms in the cell consisting of B and Co atoms as

Table 1The theoretical values of E_{vac} , E_F , E_{BGC} , Φ and β for $g\text{-C}_3\text{N}_4$, $\text{B}_{\text{C1}}\text{-C}_3\text{N}_4$, $\text{B}_{\text{C2}}\text{-C}_3\text{N}_4$, $\text{Co-C}_3\text{N}_4$, $(\text{Co-B})_{\text{C1}}\text{-C}_3\text{N}_4$ and $(\text{Co-B})_{\text{C2}}\text{-C}_3\text{N}_4$.

| Sample | Vacuum Energy (E_{vac}) (eV) | Fermi Energy (E_F) (eV) | Band Gap Center (E_{BGC}) (eV) | Work Function (Φ) (eV) | Effective Mass Ratio (β) |
|--|---|-----------------------------|---|-------------------------------|----------------------------------|
| $g\text{-C}_3\text{N}_4$ | 2.06 | −2.34 | −4.71 | 4.39 | 0.49 |
| $\text{B}_{\text{C1}}\text{-C}_3\text{N}_4$ | 2.06 | −3.46 | −4.34 | 5.52 | 0.95 |
| $\text{B}_{\text{C2}}\text{-C}_3\text{N}_4$ | 2.05 | −3.88 | −4.53 | 5.93 | 0.72 |
| $\text{Co-C}_3\text{N}_4$ | 2.16 | −1.19 | −4.78 | 3.35 | 1.99 |
| $(\text{Co-B})_{\text{C1}}\text{-C}_3\text{N}_4$ | 2.15 | −1.81 | −4.63 | 3.95 | 2.71 |
| $(\text{Co-B})_{\text{C2}}\text{-C}_3\text{N}_4$ | 2.13 | −1.85 | −4.58 | 3.98 | 1.55 |

Table 2Löwdin charge analysis of different atoms for $g\text{-C}_3\text{N}_4$, $\text{B}_{\text{C1}}\text{-C}_3\text{N}_4$, $\text{B}_{\text{C2}}\text{-C}_3\text{N}_4$, $\text{Co-C}_3\text{N}_4$, $(\text{Co-B})_{\text{C1}}\text{-C}_3\text{N}_4$ and $(\text{Co-B})_{\text{C2}}\text{-C}_3\text{N}_4$.

| Atom | C_3N_4 | $\text{B}_{\text{C1}}\text{-C}_3\text{N}_4$ | $\text{B}_{\text{C2}}\text{-C}_3\text{N}_4$ | $\text{Co-C}_3\text{N}_4$ | $(\text{CoB})_{\text{C1}}\text{-C}_3\text{N}_4$ | $(\text{CoB})_{\text{C2}}\text{-C}_3\text{N}_4$ |
|------|------------------------|---|---|---------------------------|---|---|
| N1 | −0.27 | −0.33 | −0.27 | −0.33 | −0.47 | −0.36 |
| N2 | −0.10 | −0.20 | −0.12 | −0.12 | −0.22 | −0.12 |
| N3 | −0.27 | −0.32 | −0.28 | −0.31 | −0.41 | −0.33 |
| N4 | −0.27 | −0.27 | −0.30 | −0.24 | −0.27 | −0.35 |
| N5 | −0.27 | −0.29 | −0.31 | −0.26 | −0.29 | −0.38 |
| N6 | −0.12 | −0.11 | −0.23 | −0.10 | −0.10 | −0.23 |
| C1 | 0.46 | — | 0.47 | 0.44 | — | 0.45 |
| C2 | 0.45 | 0.45 | — | 0.42 | 0.44 | — |
| C3 | 0.46 | 0.46 | 0.47 | 0.44 | 0.46 | 0.45 |
| B | — | 0.52 | 0.51 | — | 0.47 | 0.50 |
| Co | — | — | — | −0.35 | −0.38 | −0.33 |

neighbors are listed in Table 2. Here, $g\text{-C}_3\text{N}_4$ shows charge transfer from C to its neighboring N atoms with N₁ and N₃ having more negative charges than N₂ atoms. In $\text{B}_{\text{C1}}\text{-C}_3\text{N}_4$ and $\text{B}_{\text{C2}}\text{-C}_3\text{N}_4$, B atom transfer excess charge to neighboring N than C atoms (in pristine $g\text{-C}_3\text{N}_4$). In $\text{B}_{\text{C1}}\text{-C}_3\text{N}_4$ ($\text{B}_{\text{C2}}\text{-C}_3\text{N}_4$) neighboring N atoms N₁ and N₃ (N₄ and N₅) are more electronegative than N₂ (N₆). While in $\text{Co-C}_3\text{N}_4$ due to formation of Co–N bond, charge transfer from C to N and Co atoms is observed. Co atom gets excess charge of 0.35e due to redistribution of charges among the neighboring atoms, this redistribution leads total charge of 0.33e at N₁ atom.

In case of $(\text{Co-B})_{\text{C1}}\text{-C}_3\text{N}_4$ [$(\text{Co-B})_{\text{C2}}\text{-C}_3\text{N}_4$] there is 0.44e [0.36e] average charge transfer from C and B atoms to N₁ and N₃ [N₄ and N₅] while 0.22e [0.23] to N₂ [N₆]. The charge transfer to Co atom is 0.38e and 0.33e for $(\text{Co-B})_{\text{C1}}\text{-C}_3\text{N}_4$ and $(\text{Co-B})_{\text{C2}}\text{-C}_3\text{N}_4$, respectively. This difference in the charge transfer for $(\text{Co-B})_{\text{C1}}\text{-C}_3\text{N}_4$ and $(\text{Co-B})_{\text{C2}}\text{-C}_3\text{N}_4$ is due to charge redistribution through a channel of linking atoms between B and N₁ atom due to presence of Co atom in the void. Since charge gained by N₁ for $(\text{Co-B})_{\text{C1}}\text{-C}_3\text{N}_4$ is 0.47e and for $(\text{Co-B})_{\text{C2}}\text{-C}_3\text{N}_4$ is 0.36e (almost similar to 0.38e for N₅), N₁ is considered as the most electronegative atom in all the studied $g\text{-C}_3\text{N}_4$ monolayers and is further used as the adsorption site for water and intermediates for OER and HER.

The formation of electron channel through redistribution of charges is inspired from the fact that Cobalt Boride (CoB, Co₂B and Co₃B) [70,71] is an efficient electrocatalyst and have an effective interaction due to partially filled 3d orbital of Co and 3p orbital of B with its effective electron affinity to give its single electron present in the 2p orbital to relative more electronegative atom. This charge redistribution within the plane increase the charge carrier migration among the atoms towards the most active site for the redox and also from the present charge transfer analysis on the p_z orbital of the atoms signify the increment in the surface charge specially due to short range and long range interaction of Co–B in case of $(\text{Co-B})_{\text{C1}}\text{-C}_3\text{N}_4$ and $(\text{Co-B})_{\text{C2}}\text{-C}_3\text{N}_4$, respectively for effective charge transfer in the photocatalytic OER and HER.

3.5. Optical and photocatalytic properties

For the study of optical absorption, we have considered

epsilon.x module of QUANTUM ESPRESSO with PBE-GGA [44] which provides the complex frequency dependent dielectric $\epsilon(\omega) = \epsilon_1(\omega) + i\epsilon_2(\omega)$, function, where $\epsilon_1(\omega)$ and $\epsilon_2(\omega)$ are real and imaginary part of the dielectric function, respectively. Using $\epsilon(\omega)$ the absorption coefficient $\alpha(\omega)$ is calculated as

$$\alpha(\omega) = \sqrt{2}\omega[\sqrt{\epsilon_1(\omega)^2 + \epsilon_2(\omega)^2} - \epsilon_1(\omega)]^{1/2} \quad [22].$$

The average value is deduced from the parallel and perpendicular components of the $\alpha(\omega)$ is plotted in Fig. 4a. It is seen that $g\text{-C}_3\text{N}_4$ (shaded region) shows very small absorption in the wavelength range 450 nm–700 nm. Doping of B at either site increases the absorption as compared to pristine monolayer. The absorption spectra of $\text{Co-C}_3\text{N}_4$, $(\text{Co-B})_{\text{C1}}\text{-C}_3\text{N}_4$, and $(\text{Co-B})_{\text{C2}}\text{-C}_3\text{N}_4$ with peak-shift towards higher wavelength and their area under the curve also corresponds to the increase in the absorbance as compared to the $g\text{-C}_3\text{N}_4$.

From the imaginary part of dielectric function shown in Fig. 4 (b), presence of peak at 3.35 eV for pristine $g\text{-C}_3\text{N}_4$ corresponds to the intrinsic plasma frequencies [72]. Origin of this peak is due to electronic transition from the edge of the N-2p level in VB to the edge of the C-2p level in the CB. In case of $\text{B}_{\text{C1}}\text{-C}_3\text{N}_4$, $\text{B}_{\text{C2}}\text{-C}_3\text{N}_4$, $\text{Co-C}_3\text{N}_4$, $(\text{Co-B})_{\text{C1}}\text{-C}_3\text{N}_4$, and $(\text{Co-B})_{\text{C2}}\text{-C}_3\text{N}_4$ two peaks one at 3.32, 3.32, 3.55, 3.34 and 3.55 eV, while the other at 0.82, 0.85, 1.06, 0.89 and 0.85 eV are observed, respectively. The peak around 1.00 eV in $\text{B}_{\text{C1}}\text{-C}_3\text{N}_4$ and $\text{B}_{\text{C2}}\text{-C}_3\text{N}_4$ is due to electronic transition from the edge of the N-2p level in VB to the edge of the B-2p level around the E_F . Whereas the peak around 3.50 eV is due to electronic transition from N-2p level in VB to C₂-2p level, N₃-2p level and N₃-2p level in CB for $\text{Co-C}_3\text{N}_4$, $(\text{Co-B})_{\text{C1}}\text{-C}_3\text{N}_4$, and $(\text{Co-B})_{\text{C2}}\text{-C}_3\text{N}_4$ respectively and the low energy peak is due to intra-band transition from the edge of the N₂-2p level in the VB to the edge of the impurity Co-3d states for all three, the variation in the peak intensity and broadening is due to the short and long range interaction of the Co–B and corresponding charge redistribution among the planar atoms in the $g\text{-C}_3\text{N}_4$. Therefore, the formation of IB due to the Co loading and B-doping together in the forbidden band of $g\text{-C}_3\text{N}_4$ improved the visible light absorption in $(\text{Co-B})_{\text{C1}}\text{-C}_3\text{N}_4$ and $(\text{Co-B})_{\text{C2}}\text{-C}_3\text{N}_4$ which is beneficial to improve the photocatalytic activity.

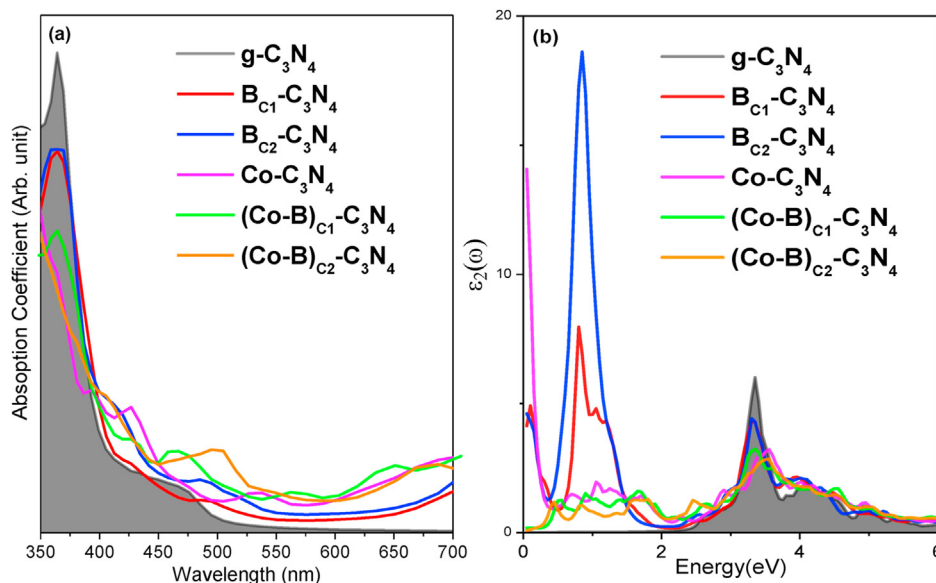


Fig. 4. (a) Absorption spectra and (b) imaginary part of dielectric function [$\epsilon_2(\omega)$] of pristine $g\text{-C}_3\text{N}_4$ (shaded region), $B_{C1}\text{-C}_3\text{N}_4$, $B_{C2}\text{-C}_3\text{N}_4$, $\text{Co-C}_3\text{N}_4$, $(\text{Co-B})_{C1}\text{-C}_3\text{N}_4$ and $(\text{Co-B})_{C2}\text{-C}_3\text{N}_4$. (A colour version of this figure can be viewed online.)

Appropriate band gap and high visible light absorption is not sufficient for any semiconductor material to work as photocatalyst for the overall solar water splitting. The position of the band edges is an important parameter for the generation of hydrogen and oxygen from water. The band edges should be positioned according to the redox potential which is a variable factor based on the use of functional and pseudopotential when done using DFT in periodic boundary condition. From the study of electrostatic potential profile, the calculated vacuum energies (E_{vac}) are given in Table 1 with band gap center (E_{BGC}) and work function (Φ) for all the samples. Fig. S3 shows electrostatic potential profile for $(\text{Co-B})_{C1}\text{-C}_3\text{N}_4$, where we have marked the various energies like E_{BGC} , E_{F} , Φ , valence band edge (E_{VB}) and conduction band edge (E_{CB}) with respect to the E_{vac} with corrected band edges according to the model given by Refs. [73,74].

In Fig. 5, theoretical values of bandgap (E_{g}), E_{VB} and E_{CB} for all the studied monolayers along with the experimental band edges of

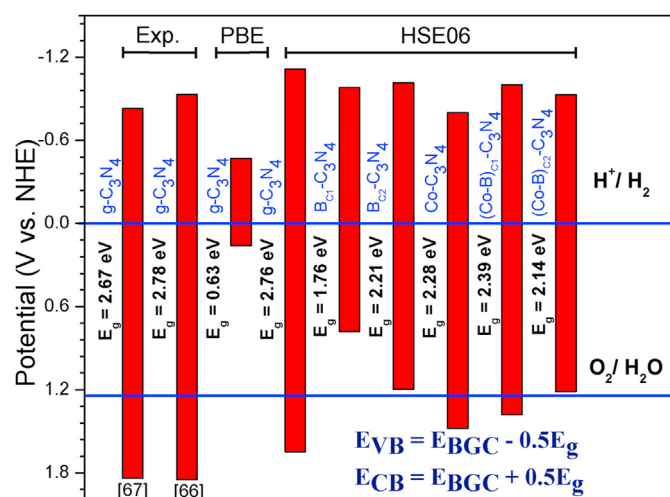


Fig. 5. The E_{VB} and E_{CB} levels with respect to NHE potential for pristine $g\text{-C}_3\text{N}_4$, $B_{C1}\text{-C}_3\text{N}_4$, $B_{C2}\text{-C}_3\text{N}_4$, $\text{Co-C}_3\text{N}_4$, $(\text{Co-B})_{C1}\text{-C}_3\text{N}_4$ and $(\text{Co-B})_{C2}\text{-C}_3\text{N}_4$ along with the experimental values of E_{VB} and E_{CB} for bulk [67], and nano-sheet [66] of pristine $g\text{-C}_3\text{N}_4$. (A colour version of this figure can be viewed online.)

Table 3

The value of E_{VB} and E_{CB} along with the calculated overpotentials of OER ($\Delta\eta^{\text{OER}}$) and HER ($\Delta\eta^{\text{HER}}$) for $g\text{-C}_3\text{N}_4$, $B_{C1}\text{-C}_3\text{N}_4$, $B_{C2}\text{-C}_3\text{N}_4$, $\text{Co-C}_3\text{N}_4$, $(\text{Co-B})_{C1}\text{-C}_3\text{N}_4$ and $(\text{Co-B})_{C2}\text{-C}_3\text{N}_4$.

| System | E_{VB} (V) | $\Delta\eta^{\text{OER}}$ (V) | $ E_{\text{CB}} $ (V) | $ \Delta\eta^{\text{HER}} $ (V) | |
|---|---------------------|-------------------------------|-----------------------|---------------------------------|------------------------|
| | | | | H^+ | H_3O^+ |
| $g\text{-C}_3\text{N}_4$ | 1.65 | 2.32 | 1.11 | 0.69 | 0.68 |
| $B_{C1}\text{-C}_3\text{N}_4$ | 0.78 | 1.22 | 0.98 | 2.11 | 2.15 |
| $B_{C2}\text{-C}_3\text{N}_4$ | 1.19 | 1.27 | 1.02 | 2.37 | 2.38 |
| $\text{Co-C}_3\text{N}_4$ | 1.48 | 1.78 | 0.80 | 0.06 | 0.13 |
| $(\text{Co-B})_{C1}\text{-C}_3\text{N}_4$ | 1.38 | 1.28 | 1.00 | 0.27 | 0.42 |
| $(\text{Co-B})_{C2}\text{-C}_3\text{N}_4$ | 1.21 | 1.08 | 0.93 | 0.37 | 0.45 |

pristine $g\text{-C}_3\text{N}_4$ bulk [67] and nano-sheet [66] are presented. We have also mentioned the E_{g} , E_{VB} and E_{CB} values for pristine film using PBE-GGA functional in Fig. 5. Here it is seen that the opening of the band gap after using HSE06 functional gives uneven shift in E_{VB} and E_{CB} which is also reported previously [75,76]. In Table 3, we have calculated the value of E_{VB} and E_{CB} . By the analysis of E_{VB} and E_{CB} for all the functionalized $g\text{-C}_3\text{N}_4$ monolayers it is seen that the E_{CB} is well above the reduction potential for hydrogen generation, while for $B_{C1}\text{-C}_3\text{N}_4$ is far above the oxidation potential, though $B_{C2}\text{-C}_3\text{N}_4$, $(\text{Co-B})_{C2}\text{-C}_3\text{N}_4$ are close to oxidation potential but do not cross it, but rest of the monolayers cross the oxidation potential. Therefore, on the basis of band edge position analysis, $g\text{-C}_3\text{N}_4$, $\text{Co-C}_3\text{N}_4$ and $(\text{Co-B})_{C1}\text{-C}_3\text{N}_4$ will be suitable for the overall water splitting.

3.6. Thermodynamic performance

For efficient photocatalyst, besides the suitable band gap, suitable band edges with respect to NHE potential, charge carrier separation and high optical performance in visible energy region, thermodynamic performance of photocatalyst during OER and HER also plays a major role. In following section, we have studied the reaction thermodynamics for both OER and HER.

3.6.1. Oxygen evolution reaction

For the analysis of the water splitting process, study of the adsorption of H_2O , OH , O and OOH on the surface of catalyst is essential. For this purpose, we have studied adsorption energies of H_2O , OH , O and OOH intermediates on the pristine and all functionalized $\text{g-C}_3\text{N}_4$ and the adsorption energy of each is calculated using Eqs. (4)–(7). In the present case for the adsorption of different intermediates we have considered the most electronegative N i.e. N_1 on the basis of present charge redistribution analysis. Same site is also considered as suitable site for water adsorption [77]. For $(\text{Co-B})_{\text{C}_1-\text{C}_3\text{N}_4}$ the initial and optimized structures for adsorption of all the intermediates are shown in Table S1.

Initially, adsorption of water molecule is studied as the first step of a four electron step, for this a water molecule has been kept at a distance of 3.42 Å above the $\text{g-C}_3\text{N}_4$, with the orientation that one O–H bond is parallel to the plane of $\text{g-C}_3\text{N}_4$ and another O–H is towards the N_1 atom. The optimized structure after water adsorption shows the change in orientation of H_2O molecule for all the structures in such a manner that the H atom forms hydrogen bond with N_4 due to electronegativity of N. The value of $\Delta E_{\text{H}_2\text{O}}$ is calculated as -0.43eV for $\text{g-C}_3\text{N}_4$ which is in agreement with the other theoretical report [77]. The calculated $\Delta E_{\text{H}_2\text{O}}$ values are 0.04, -0.16 , -0.14 , 0.04 and -0.05eV for $\text{B}_{\text{C}_1-\text{C}_3\text{N}_4}$, $\text{B}_{\text{C}_2-\text{C}_3\text{N}_4}$, $\text{Co-C}_3\text{N}_4$, $(\text{Co-B})_{\text{C}_1-\text{C}_3\text{N}_4}$, and $(\text{Co-B})_{\text{C}_2-\text{C}_3\text{N}_4}$, respectively implying the physical adsorption of water molecule since it needs small adsorption energy.

The water molecule on the surface of catalyst is converted to OH^* and $(\text{H}^+ + \text{e}^-)$ pair according to the reaction in Eq. (9) as the first step of OER, the adsorption energy (ΔE_{OH^*}), Gibbs free energy (ΔG_1) and the adsorbed state of OH^* on the surface of catalyst is important for the energy changes in forthcoming reaction steps and initial structure for next step reaction. The structure after computation with OH^* as an intermediate leads to formation of O– N_1 bond for $\text{g-C}_3\text{N}_4$, $\text{B}_{\text{C}_1-\text{C}_3\text{N}_4}$, $\text{B}_{\text{C}_2-\text{C}_3\text{N}_4}$ and O– C_1 bond, O–B bond, O–Co bond for $\text{Co-C}_3\text{N}_4$, $(\text{Co-B})_{\text{C}_1-\text{C}_3\text{N}_4}$, and $(\text{Co-B})_{\text{C}_2-\text{C}_3\text{N}_4}$, respectively with change in orientation and further distortion in the z plane. The calculated values of ΔE_{OH^*} for $\text{g-C}_3\text{N}_4$, $\text{B}_{\text{C}_1-\text{C}_3\text{N}_4}$, $\text{B}_{\text{C}_2-\text{C}_3\text{N}_4}$, $\text{Co-C}_3\text{N}_4$, $(\text{Co-B})_{\text{C}_1-\text{C}_3\text{N}_4}$, and $(\text{Co-B})_{\text{C}_2-\text{C}_3\text{N}_4}$ are 2.15, 0.59, 0.74, -0.39 , -0.23 and 0.03eV , respectively.

After the separation of a proton from the OH^* radical leads to O^* and $(\text{H}^+ + \text{e}^-)$ pair formation in accordance with Eq. (10), the remaining O^* makes bond with N_1 atoms for $\text{g-C}_3\text{N}_4$, $\text{B}_{\text{C}_1-\text{C}_3\text{N}_4}$, $\text{B}_{\text{C}_2-\text{C}_3\text{N}_4}$, while $\text{Co-C}_3\text{N}_4$, $(\text{Co-B})_{\text{C}_1-\text{C}_3\text{N}_4}$, and $(\text{Co-B})_{\text{C}_2-\text{C}_3\text{N}_4}$ make bond with C_1 , Co & B and Co, with the ΔE_{O^*} as 2.51, 2.22, 2.62, 0.74, 1.46 and 1.45 eV, respectively. In third step, the conversion of second water molecule to OOH^* and $(\text{H}^+ + \text{e}^-)$ pair via the formation of OH^* which combines with O^* according to Eq. (11), the OOH^* is adsorbed on the N_1 atom for $\text{g-C}_3\text{N}_4$, $\text{B}_{\text{C}_1-\text{C}_3\text{N}_4}$, $\text{B}_{\text{C}_2-\text{C}_3\text{N}_4}$, and on C_1 atom for $\text{Co-C}_3\text{N}_4$ and Co for $(\text{Co-B})_{\text{C}_1-\text{C}_3\text{N}_4}$, and $(\text{Co-B})_{\text{C}_2-\text{C}_3\text{N}_4}$, with ΔE_{OOH^*} as 4.45, 4.32, 4.78, 3.40, 3.62 and 3.41 eV, respectively. In the fourth reaction OOH^* is converted to O_2 and $(\text{H}^+ + \text{e}^-)$ pair, whereas the ΔG_4 of the final reaction is calculated by Eq. (12) to keep the $\Delta G_{1-4} = 4.92\text{eV}$ [59]. Value of ΔG_3 is found to be maximum for all the studied monolayers, therefore it is considered as the rate determining step and has to be considered for the calculation of overpotential.

The variation in ΔG calculated using the change in adsorption energy with each intermediate for pristine and functionalized $\text{g-C}_3\text{N}_4$ are plotted in Fig. 6(a–f) at three different potential: $U = 0$, 1.23 and η^{OER} V. From Fig. 6(a), for $\text{g-C}_3\text{N}_4$, $\Delta G_3 = 3.55\text{eV}$ is found to be maximum at 0 V than the free energy changes of other reactions, thus using Eq. (13) the value of η^{OER} is calculated as 3.55 V. At the equilibrium position at $U = 1.23\text{V}$ the free energy value reduced and the $\Delta\eta^{\text{OER}}$ becomes 2.32 V therefore the plot at $U = 3.55\text{V}$ corresponds to the complete downhill OER reaction.

ΔG_3 value of $\text{B}_{\text{C}_1-\text{C}_3\text{N}_4}$, $\text{B}_{\text{C}_2-\text{C}_3\text{N}_4}$, $\text{Co-C}_3\text{N}_4$, $(\text{Co-B})_{\text{C}_1-\text{C}_3\text{N}_4}$, and $(\text{Co-B})_{\text{C}_2-\text{C}_3\text{N}_4}$ are calculated to be 2.45, 2.50, 3.01, 2.51 and 2.31 eV, respectively at $U = 0\text{V}$, while their corresponding values for $U = 1.23\text{eV}$ are reduced to 1.22, 1.27, 1.78, 1.28 and 1.08 V which also corresponds to the respective $\Delta\eta^{\text{OER}}$ values. Reactions at $U = \eta^{\text{OER}}$ are found to be downhill which imply that reaction will take place simultaneously. The $\Delta\eta^{\text{OER}}$ of all the samples are smaller than that of pristine $\text{g-C}_3\text{N}_4$ which is useful to improve the photocatalytic activity of $\text{g-C}_3\text{N}_4$ and also predicted by Wirth et al. [17] which concludes the effectiveness of B and Co as co-catalyst with $\text{g-C}_3\text{N}_4$.

As mentioned earlier also, that the position of $E_{\text{CB}}/E_{\text{VB}}$ crossing the reduction/oxidation potential does not guarantee the overall water splitting since $\text{g-C}_3\text{N}_4$ suffers from high over potentials, the value of $\Delta\eta^{\text{OER}}$ should be lower than the E_{VB} [72]. Here water oxidation efficiency is analyzed by comparing the $\Delta\eta^{\text{OER}}$ with E_{VB} , in our case all the samples except $(\text{Co-B})_{\text{C}_1-\text{C}_3\text{N}_4}$ and $(\text{Co-B})_{\text{C}_2-\text{C}_3\text{N}_4}$ has lower E_{VB} than its corresponding $\Delta\eta^{\text{OER}}$ value. $(\text{Co-B})_{\text{C}_2-\text{C}_3\text{N}_4}$ does not cross the oxidative potential whereas $(\text{Co-B})_{\text{C}_1-\text{C}_3\text{N}_4}$ found as the most suitable material for the oxidation reaction among the rest.

3.6.2. Hydrogen evolution reaction

For HER (according to Eqs. (15)–(18)), an isolated H atom or H_3O molecule (for the effect of extra water molecule) are adsorbed over the N_1 atom due to its high electronegative nature and the adsorption energy is calculated using Eq. (14) for H and Eq. (3) for H_3O molecule. The brief structural changes before and after optimization on adsorbing the H and H_3O molecule on $(\text{Co-B})_{\text{C}_1}$ are presented in Table S2. The H atom is chemically bonded to N_1 atom for $\text{g-C}_3\text{N}_4$ and $\text{B}_{\text{C}_1-\text{C}_3\text{N}_4}$ while it bonds with N_4 for $\text{B}_{\text{C}_2-\text{C}_3\text{N}_4}$ due to the higher electronegativity. With $\text{Co-C}_3\text{N}_4$, $(\text{Co-B})_{\text{C}_1-\text{C}_3\text{N}_4}$ and $(\text{Co-B})_{\text{C}_2-\text{C}_3\text{N}_4}$, H atom chemically bonded to Co. In the case of H_3O molecule the separation of H atom and H_2O molecule take place where H atom makes hydrogen bond with N_4 in $\text{g-C}_3\text{N}_4$ while for $\text{B}_{\text{C}_1-\text{C}_3\text{N}_4}$, $\text{B}_{\text{C}_2-\text{C}_3\text{N}_4}$ it bonds chemically with N_1 , N_4 , respectively and with Co for $\text{Co-C}_3\text{N}_4$, $(\text{Co-B})_{\text{C}_1-\text{C}_3\text{N}_4}$ and $(\text{Co-B})_{\text{C}_2-\text{C}_3\text{N}_4}$ while H_2O molecule remains free. The corresponding change in Gibbs free energy of H atom and H_3O molecule (ΔG_{H^*} and $\Delta G_{\text{H}_3\text{O}^*}$) is plotted in Fig. 7 (a, b). The negative value of the free energy corresponds to the favorable adsorption site [78]. ΔG_{H^*} and $\Delta G_{\text{H}_3\text{O}^*}$ are almost same for $\text{g-C}_3\text{N}_4$, $\text{B}_{\text{C}_1-\text{C}_3\text{N}_4}$, $\text{B}_{\text{C}_2-\text{C}_3\text{N}_4}$, while $\Delta G_{\text{H}_3\text{O}^*}$ is higher for $\text{Co-C}_3\text{N}_4$, $(\text{Co-B})_{\text{C}_1-\text{C}_3\text{N}_4}$ and $(\text{Co-B})_{\text{C}_2-\text{C}_3\text{N}_4}$ as compared to ΔG_{H^*} .

Comparing the $\Delta\eta^{\text{HER}}$ with the E_{CB} (Table 3), both the B-doped monolayers ($\text{B}_{\text{C}_1-\text{C}_3\text{N}_4}$ and $\text{B}_{\text{C}_2-\text{C}_3\text{N}_4}$) are not found suitable for HER while $\text{g-C}_3\text{N}_4$, $\text{Co-C}_3\text{N}_4$, $(\text{Co-B})_{\text{C}_1-\text{C}_3\text{N}_4}$, and $(\text{Co-B})_{\text{C}_2-\text{C}_3\text{N}_4}$ showing their effective utilization for hydrogen production. Among the HER suitable monolayers, $\text{Co-C}_3\text{N}_4$ shows very small value of $\Delta\eta^{\text{HER}}$ which is smaller than the reported value of Pt loaded $\text{g-C}_3\text{N}_4$ [78].

3.7. Effect of Co and B on photocatalytic activity of $\text{g-C}_3\text{N}_4$

To design any material for overall water splitting following properties should be considered (i) high absorption in the visible energy region; (ii) suitable band edges with respect to NHE; (iii) excess charge carriers on the surface with high mobility and low recombination of charge carriers; (iv) suitable value of overpotential ($\Delta\eta^{\text{OER}}/\Delta\eta^{\text{HER}}$). In the present study, with the aim to design a material for overall water splitting we have functionalized $\text{g-C}_3\text{N}_4$ with B-doping, Co-loading and B-doping and Co-loading together. Substituting B at C site either at C_1 or C_2 facilitate hole in the lattice which shows its affinity to lose its single electron to neighboring highly electronegative N (as seen from charge

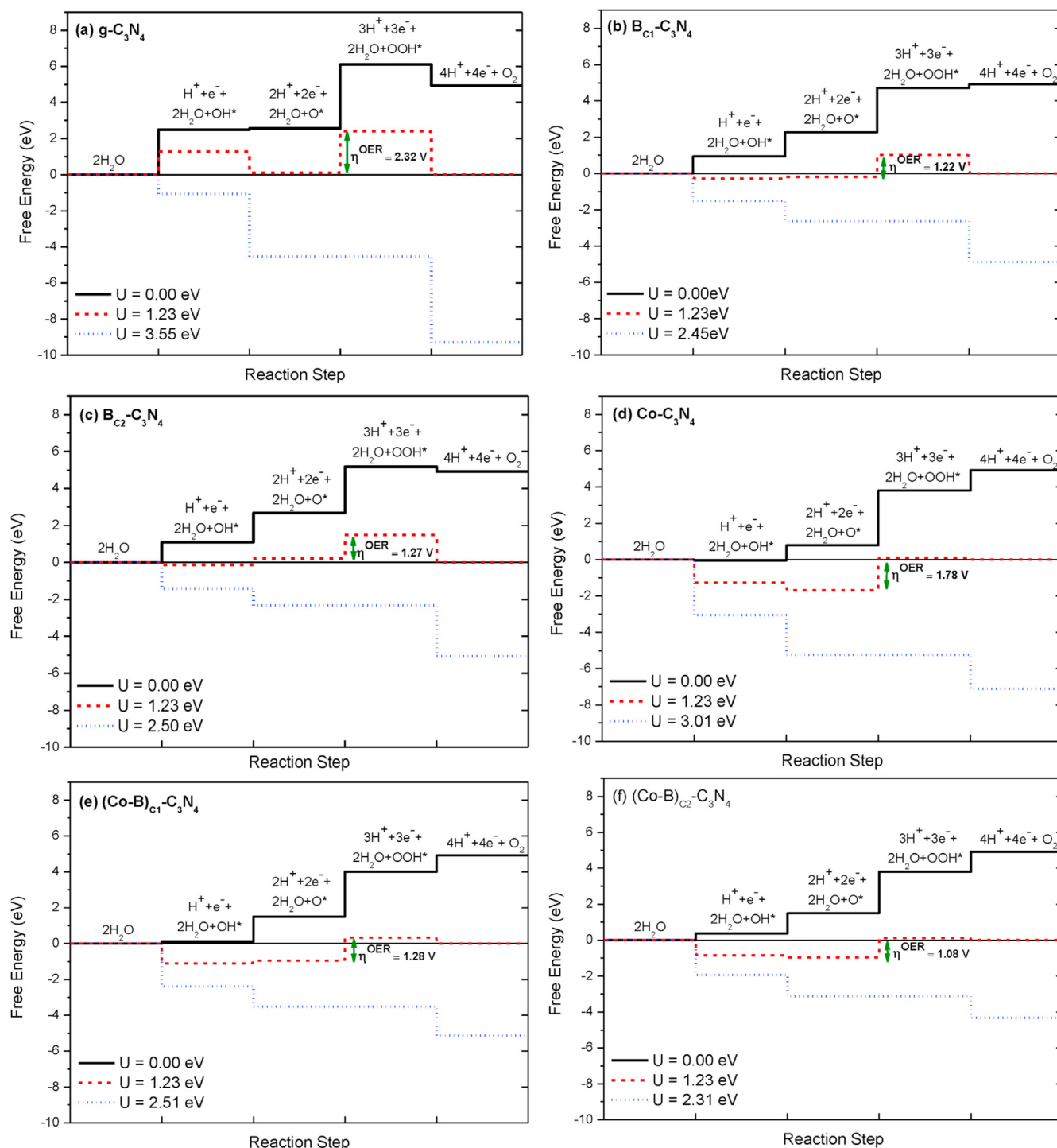


Fig. 6. Gibbs free energy change profile of OER for (a) $g\text{-C}_3\text{N}_4$, (b) $\text{B}_{\text{C}_1}\text{-C}_3\text{N}_4$, (c) $\text{B}_{\text{C}_2}\text{-C}_3\text{N}_4$, (d) $\text{Co-C}_3\text{N}_4$, (e) $(\text{Co-B})_{\text{C}_1}\text{-C}_3\text{N}_4$ and (f) $(\text{Co-B})_{\text{C}_2}\text{-C}_3\text{N}_4$. (A colour version of this figure can be viewed online.)

redistribution). Neighboring N plays major role for B doping due to B–N p_π – p_π hybridization and shifting of unoccupied levels to low energy thus reducing the bandgap and affecting the valence band edge (E_{VB}), thus $\text{B}_{\text{C}_1}\text{-C}_3\text{N}_4$ does not show OER activity while $\text{B}_{\text{C}_2}\text{-C}_3\text{N}_4$ can participate. B-doping also leads to increment in hole concentration and decreasing the $\Delta\eta^{\text{OER}}$ due to the change in interaction of intermediates as compared to $g\text{-C}_3\text{N}_4$ while the higher value of $|\Delta\eta^{\text{HER}}|$ prohibits easy hydrogen evolution.

Presence of partially filled TM (Co) in the lattice increases the

electron density due to their affinity to be stable after giving electrons, Co loading provides electron pair from its 3d orbital which leads to formation of IB bringing Co loaded $g\text{-C}_3\text{N}_4$ in visible spectrum while enhancing E_{CB} for efficient HER, p_π – d_π orbital interaction of Co–N facilitate charge redistribution over the N_1 atom making it electron rich as effective adsorption site for HER.

In case of B-doping and Co-loading together, the E_{F} is shifted in the middle of the forbidden band gap which also shows partial charge compensation in $g\text{-C}_3\text{N}_4$. Hybridization of Co-3d and B-2p

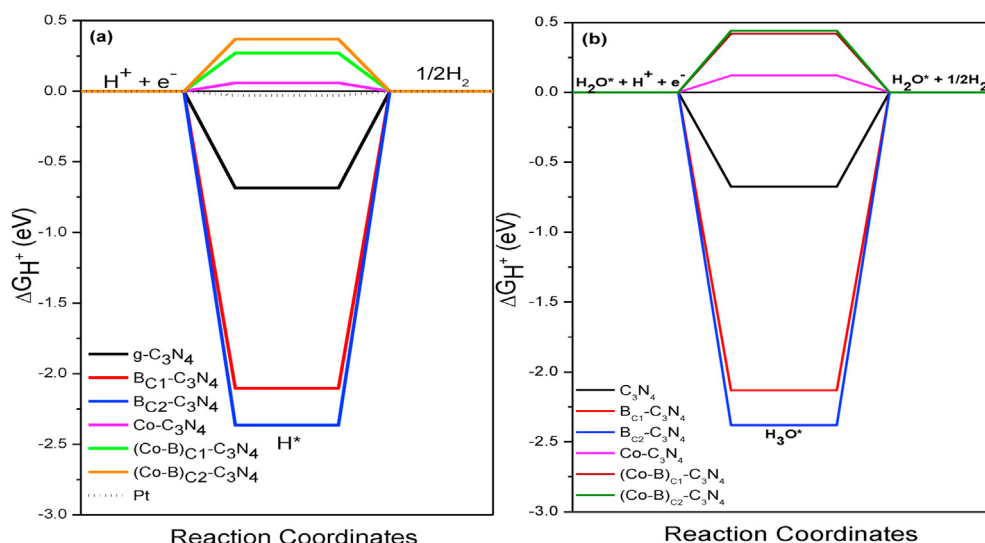


Fig. 7. The change in free energy of HER for $g\text{-C}_3\text{N}_4$, $\text{B}_{\text{C1}}\text{-C}_3\text{N}_4$, $\text{B}_{\text{C2}}\text{-C}_3\text{N}_4$, $\text{Co-C}_3\text{N}_4$, $(\text{Co-B})_{\text{C1}}\text{-C}_3\text{N}_4$ and $(\text{Co-B})_{\text{C2}}\text{-C}_3\text{N}_4$ with adsorption of (a) an isolated H atom and (b) H_2O molecule. Pt is plotted for reference [62]. (A colour version of this figure can be viewed online.)

orbitals formed impurity states which gives higher absorption as compared to pristine while $(\text{Co-B})_{\text{C1}}\text{-C}_3\text{N}_4$ shows the highest absorption. To check the effect of Co and B interaction, different concentration of Co and B in $2 \times 2 \times 1$ cell of $g\text{-C}_3\text{N}_4$ is also considered. Along with the previously mentioned 1 Co (1 B) loading (doping) i.e. $(\text{Co-B})_{\text{C1}}\text{-C}_3\text{N}_4$, three different arrangements were considered (as mentioned in Fig. S4 and Table S3) and studied using PBE-GGA only (due to the computationally expensive HSE06). On the basis of ΔE_b (Table S3), formation of $(\text{Co-2B})_{\text{C1}}\text{-C}_3\text{N}_4$ and $(2\text{Co-2B})_{\text{C1}}\text{-C}_3\text{N}_4$ is feasible while $(2\text{Co-B})_{\text{C1}}\text{-C}_3\text{N}_4$ shows positive value of E_b . DOS in Fig. S4 (using PBE-GGA) does not show any feature of impurity states formation in the $(\text{Co-2B})_{\text{C1}}\text{-C}_3\text{N}_4$, $(2\text{Co-B})_{\text{C1}}\text{-C}_3\text{N}_4$ and $(2\text{Co-2B})_{\text{C1}}\text{-C}_3\text{N}_4$ as visible in case of $(\text{Co-B})_{\text{C1}}\text{-C}_3\text{N}_4$ (PBE-GGA). Therefore, charge compensation and distinct impurity state formation is obtained only in case $(\text{Co-B})_{\text{C1}}\text{-C}_3\text{N}_4$ in the present study.

It is also seen that the Co-loading in B-doped $g\text{-C}_3\text{N}_4$ enhances the negative charge on N_1 atom mainly due to the short [long] range interaction between Co and B in $(\text{Co-B})_{\text{C1}}\text{-C}_3\text{N}_4$ [$(\text{Co-B})_{\text{C2}}\text{-C}_3\text{N}_4$] making the N site active for the effective adsorption of intermediate due to electronegativity difference. From effective mass analysis it is concluded that due to the formation of impurity states, $(\text{Co-B})_{\text{C1}}\text{-C}_3\text{N}_4$ shows lowest rate of recombination of charge carriers and the formed impurity states will be considered as deep trapping site increasing the life time and availability of photogenerated e^- - h^+ pair for redox reactions.

The Co-B combination provides the e^- - h^+ pair hence good for HER and OER, but the site dependence of B in $g\text{-C}_3\text{N}_4$ in different properties reversed with Co-loading due to large Pauling electronegativity difference which is dependent on the interaction range but in both cases N_1 is the most suitable site for adsorption. The formation of impurity states and charge redistribution over the plane due to the electron affinity and partially filled Co-3d orbitals leads to p_π - d_π bonding for Co-B in short range interaction, while as the effect of B in long range interaction is observed via charge difference on its neighboring N. Hence the formation of channel for charge redistribution leading to increase in electronegativity of N_1 atom for further enhancement in other properties.

From thermodynamical analysis, $\text{Co-C}_3\text{N}_4$ is considered best suitable among all the studied monolayers for HER while $(\text{Co-B})_{\text{C1}}\text{-C}_3\text{N}_4$ is considered for overall water splitting since the

individual doping/loading properties are now combined with synergistic effect of Co-B interaction. If we consider all the affecting parameters like, the synergistic effect of impurity states formation, low rate of charge carrier recombination and low overpotential with respect to $g\text{-C}_3\text{N}_4$ for both OER and HER make $(\text{Co-B})_{\text{C1}}\text{-C}_3\text{N}_4$ as efficient photocatalyst for overall water splitting.

4. Conclusion

The structural, electronic and optical properties of pristine $g\text{-C}_3\text{N}_4$, $\text{B}_{\text{C1}}\text{-C}_3\text{N}_4$, $\text{B}_{\text{C2}}\text{-C}_3\text{N}_4$, $\text{Co-C}_3\text{N}_4$, $(\text{Co-B})_{\text{C1}}\text{-C}_3\text{N}_4$, and $(\text{Co-B})_{\text{C2}}\text{-C}_3\text{N}_4$ were studied using the hybrid density functional theory in form of atomic monolayer for the application of photocatalytic activity. The shortcomings of low charge generation and high rate of recombination of e^- - h^+ pair in $g\text{-C}_3\text{N}_4$ were resolved by B-doping and Co-loading. The partial filled B-2p orbitals help in the charge generation and the redistribution in the $g\text{-C}_3\text{N}_4$. Formation of IB on Co-loading while sharpening [broadening] of impurity states when B is interacted with Co with short [long] range is observed in $(\text{Co-B})_{\text{C1}}\text{-C}_3\text{N}_4$ [$(\text{Co-B})_{\text{C2}}\text{-C}_3\text{N}_4$]. Sharp impurity states in VB of $(\text{Co-B})_{\text{C1}}\text{-C}_3\text{N}_4$ reduced the rate of recombination of e^- - h^+ hence improved the efficiency of the photocatalytic activity. The effect of Co-B short and long range interaction and charge redistribution, excess negative charge is collected on N_1 atom leads to change the adsorption energy of intermediates in HER and OER which modify overpotential values tends to better overall photocatalytic water splitting. On the basis of overpotential values and band edges analysis, we report $(\text{Co-B})_{\text{C1}}\text{-C}_3\text{N}_4$ as good photocatalyst for overall water splitting.

CRediT authorship contribution statement

B.R. Bhagat: Creation of models, Formal analysis, Writing – original draft. **Alpa Dashora:** Conceptualization, Supervision, preparation, creation and/or presentation of the published work.

Declaration of competing interest

The authors declare that they have no known competing financial interests or personal relationships that could have appeared to influence the work reported in this paper.

Acknowledgement

The authors show their sincere gratitude to the Department of Science and Technology, India for their DST-INSPIRE Faculty project. AD is also thankful to University Grants Commission, India for the financial support under Faculty Recharge Programme. Authors are also thankful to Dr. Nainesh Patel, University of Mumbai, India for valuable discussions.

Appendix A. Supplementary data

Supplementary data to this article can be found online at <https://doi.org/10.1016/j.carbon.2021.03.049>.

References

- [1] A.K. Geim, K.S. Novoselov, The rise of graphene, *Nat. Mater.* 6 (2007) 183–191.
- [2] K.S. Novoselov, A.K. Geim, S.V. Morozov, D. Jiang, Y. Zhang, S.V. Dubonos, et al., Electric field effect in atomically thin carbon films, *Science* 306 (2004) 666–669.
- [3] D. Pacile, J.C. Meyer, C.O. Girit, A. Zettl, The two-dimensional phase of boron nitride: few-atomic-layer sheets and suspended membranes, *Appl. Phys. Lett.* 92 (2008), 133107.
- [4] Y. Lin, T.V. Williams, J.W. Connell, Soluble, exfoliated hexagonal boron nitride nanosheets, *J. Phys. Chem. Lett.* 1 (2009) 277–283.
- [5] J.N. Coleman, M. Lotya, A. O'Neill, S.D. Bergin, P.J. King, U. Khan, et al., Two-dimensional nanosheets produced by liquid exfoliation of layered materials, *Science* 331 (2011) 568–571.
- [6] H. Li, G. Lu, Z. Yin, Q. He, H. Li, Q. Zhang, et al., Optical identification of single- and few-layer MoS₂ sheets, *Small* 8 (2012) 682–686.
- [7] Y. Omomo, T. Sasaki, L. Wang, M. Watanabe, Redoxable nanosheet crystallites of MnO₂ derived via delamination of a layered manganese oxide, *J. Am. Chem. Soc.* 125 (2003) 3568.
- [8] X. Li, J. Zhou, Q. Wang, Y. Kawazoe, P. Jena, Patterning graphitic C–N sheets into a kagome lattice for magnetic materials, *J. Phys. Chem. Lett.* 4 (2012) 259–263.
- [9] Y. Zhang, T. Mori, L. Niu, J. Ye, Non-covalent doping of graphitic carbon nitride polymer with graphene: controlled electronic structure and enhanced optoelectronic conversion, *Energy Environ. Sci.* 4 (2011) 4517–4521.
- [10] Y. Zhang, T. Mori, J. Ye, M. Antonietti, Phosphorus-doped carbon nitride solid: enhanced electrical conductivity and photocurrent generation, *J. Am. Chem. Soc.* 132 (2010) 6294–6295.
- [11] A. Thomas, A. Fischer, F. Goettmann, M. Antonietti, J.O. Muller, R. Schlögl, J.M. Carlsson, Graphitic carbon nitride materials: variation of structure and morphology and their use as metal-free catalysts, *J. Mater. Chem.* 18 (2008) 4893–4908.
- [12] A.H. Reshak, S.A. Khan, S. Auluck, Electronic band structure and specific features of AA- and AB-stacking of carbon nitride (C₃N₄): DFT calculation, *RSC Adv.* 4 (2014) 6957–6964.
- [13] B. Wei, W. Wang, J. Sun, Q. Mei, Z. An, H. Cao, et al., Insight into the effect of boron doping on electronic structure, photocatalytic and adsorption performance of g-C₃N₄ by first-principles study, *Appl. Surf. Sci.* 511 (2020) 145549.
- [14] X. Wang, K. Maeda, A. Thomas, K. Takanabe, G. Xin, J.M. Carlsson, et al., A metal-free polymeric photocatalyst for hydrogen production from water under visible light, *Nat. Mater.* 8 (2009) 76–80.
- [15] G. Liu, P. Niu, C.H. Sun, S.C. Smith, Z.G. Chen, G.Q. Lu, et al., Unique electronic structure induced high photoreactivity of sulfur-doped graphitic C₃N₄, *J. Am. Chem. Soc.* 130 (2010) 7176.
- [16] D.J. Martin, K.P. Qiu, S.A. Shevlin, A.D. Handoko, X.W. Chen, Z.X. Guo, et al., Highly efficient photocatalytic H₂ evolution from water using visible light and structure-controlled graphitic carbon nitride, *Angew. Chem.* 53 (2014) 9240–9245.
- [17] J. Wirth, R. Neumann, M. Antonietti, P. Saalfrank, Adsorption and photocatalytic splitting of water on graphitic carbon nitride: a combined first principles and semiempirical study, *Phys. Chem. Chem. Phys.* 16 (2014) 15917–15926.
- [18] K. Dai, D. Li, L. Lu, C. Liang, Q. Liu, G. Zhu, Plasmonic TiO₂/AgBr/Ag ternary composite nanosphere with heterojunction structure for advanced visible light photocatalyst, *Appl. Surf. Sci.* 314 (2014) 864–871.
- [19] Y. Li, Y. Zhao, L. Fang, R. Jin, Y. Yang, Y. Xing, Highly efficient composite visible light-driven Ag–AgBr/g-C₃N₄ plasmonic photocatalyst for degrading organic pollutants, *Mater. Lett.* 126 (2014) 5–8.
- [20] F. Su, S.C. Mathew, G. Lipner, X. Fu, M. Antonietti, S. Blechert, X. Wang, mpg-C₃N₄-catalyzed selective oxidation of alcohols using O₂ and visible light, *J. Am. Chem. Soc.* 132 (2010) 16299–16301.
- [21] K. Maeda, X. Wang, Y. Nishihara, D. Lu, M. Antonietti, K. Domen, Photocatalytic activities of graphitic carbon nitride powder for water reduction and oxidation under visible light, *J. Phys. Chem. C* 113 (2009) 4940–4947.
- [22] X. Bai, L. Wang, Y. Wang, W. Yao, Y. Zhu, Enhanced oxidation ability of g-C₃N₄ photocatalyst via C60 modification, *Appl. Catal. B Environ.* 152–153 (2014) 262–270.
- [23] L.Y. Chen, W.D. Zhang, In₂O₃/g-C₃N₄ composite photocatalysts with enhanced visible light driven activity, *Appl. Surf. Sci.* 301 (2014) 428–435.
- [24] S. Wang, C. Li, T. Wang, P. Zhang, A. Li, J. Gong, Controllable synthesis of nanotube-type graphitic C₃N₄ and their visible-light photocatalytic and fluorescent properties, *J. Mater. Chem. A2* (2014) 2885–2890.
- [25] G. Koh, Y.W. Zhang, H. Pan, First-principles study on hydrogen storage by graphitic carbon nitride nanotubes, *Int. J. Hydrogen Energy* 37 (2012) 4170–4178.
- [26] S. Lu, Z.W. Chen, C. Li, H.H. Li, Y.F. Zhao, Y.Y. Gong, et al., Adjustable electronic performances and redox ability of a g-C₃N₄ monolayer by adsorbing nonmetal solute ions: a first principles study, *J. Mater. Chem. A* 4 (2016) 14827–14838.
- [27] S.Z. Hu, L. Ma, J.G. You, F.Y. Li, Z.P. Fan, G. Lu, et al., Enhanced visible light photocatalytic performance of g-C₃N₄ photocatalysts co-doped with iron and phosphorus, *Appl. Surf. Sci.* 311 (2014) 164–171.
- [28] D. Ghosh, G. Periyasamy, S.K. Pati, Transition metal embedded two-dimensional C₃N₄-graphene nano composite: a multifunctional material, *J. Phys. Chem. C* 118 (2014) 15487–15494.
- [29] Q.Y. Lin, L. Li, S.J. Liang, M.H. Liu, J.H. Bi, L. Wu, Efficient synthesis of monolayer carbon nitride 2D nanosheet with tunable concentration and enhanced visible-light photocatalytic activities, *Appl. Catal. B Environ.* 163 (2015) 135–142.
- [30] L.W. Ruan, G.S. Xu, L. Gu, C. Li, Y.J. Zhu, Y.X. Lu, The physical properties of Li-doped g-C₃N₄ monolayer sheet investigated by the first-principles, *Mater. Res. Bull.* 66 (2015) 156–162.
- [31] X. Zhang, X. Xie, H. Wang, J. Zhang, B. Pan, Y. Xie, Enhanced photoresponsive ultrathin graphitic-phase C₃N₄ nanosheets for bioimaging, *J. Am. Chem. Soc.* 135 (2013) 18–21.
- [32] X. Ma, Y. Lv, J. Xu, Y. Liu, R. Zhang, Y. Zhu, A strategy of enhancing the photoactivity of g-C₃N₄ via doping of nonmetal elements: a first-principles study, *J. Phys. Chem. C* 116 (2012) 23485–23493.
- [33] S. Lu, C. Li, H.H. Li, Y.F. Zhao, Y.Y. Gong, L.Y. Niu, et al., The effects of nonmetal dopants on the electronic, optical and chemical performances of monolayer g-C₃N₄ by first-principles study, *Appl. Surf. Sci.* 392 (2017) 966.
- [34] J.P. Paraknowitsch, A. Thomas, Doping carbons beyond nitrogen: an overview of advanced heteroatom doped carbons with boron, sulphur and phosphorus for energy applications, *Energy Environ. Sci.* 6 (10) (2013) 2839–2855.
- [35] F. Raziq, Y. Qu, X. Zhang, M. Humayun, J. Wu, A. Zada, et al., Enhanced cocatalyst-free visible-light activities for photocatalytic fuel production of g-C₃N₄ by trapping holes and transferring electrons, *J. Phys. Chem. C* 120 (1) (2016) 98–107.
- [36] Z. Zhu, X. Tang, T. Wang, W. Fan, Z. Liu, C. Li, et al., Insight into the effect of co-doped to the photocatalytic performance and electronic structure of g-C₃N₄ by first principle, *Appl. Catal. B Environ.* 241 (2019) 319.
- [37] L. Wang, X. Guo, Y. Chen, S. Ai, H. Ding, Cobalt-doped g-C₃N₄ as a heterogeneous catalyst for photo-assisted activation of peroxymonosulfate for the degradation of organic contaminants, *Appl. Surf. Sci.* 467 (2019) 954–962.
- [38] T. Tong, B. He, B. Zhu, B. Cheng, L. Zhang, First-principle investigation on charge carrier transfer in transition-metal single atoms loaded g-C₃N₄, *Appl. Surf. Sci.* 459 (2018) 385.
- [39] F. Ling, W. Li, L. Ye, The synergistic effect of non-metal doping or defect engineering and interface coupling on the photocatalytic property of g-C₃N₄: first-principle investigations, *Appl. Surf. Sci.* 473 (2019) 386.
- [40] Y. Zhao, Y. Lin, G. Wang, Z. Jiang, R. Zhang, C. Zhu, Photocatalytic water splitting of (F, Ti) codoped heptazine/triazine based g-C₃N₄ heterostructure: a hybrid DFT study, *Appl. Surf. Sci.* 463 (2019) 809.
- [41] S. Gupta, M.K. Patel, A. Miotello, N. Patel, Metal boride-based catalysts for electrochemical water-splitting: a review, *Adv. Funct. Mater.* 30 (1) (2020) 1906481.
- [42] S. Gupta, N. Patel, A. Miotello, D.C. Kothari, Cobalt-boride: an efficient and robust electrocatalyst for hydrogen evolution reaction, *J. Power Sources* 279 (2015) 620–625.
- [43] R. Jaiswal, N. Patel, A. Dashora, R. Fernandes, M. Yadav, R. Edla, et al., Efficient Co-B-codoped TiO₂ photocatalyst for degradation of organic water pollutant under visible light, *Appl. Catal. B Environ.* 183 (2016) 242.
- [44] P. Giannozzi, S. Baroni, N. Bonini, M. Calandra, R. Car, C. Cavazzoni, et al., Quantum ESPRESSO: a modular and open-source software project for quantum simulations of materials, *J. Phys. Condens. Matter* 21 (39) (2009), 395502.
- [45] K. Momma, F. Izumi, VESTA 3 for three-dimensional visualization of crystal, volumetric and morphology data, *J. Appl. Crystallogr.* 44 (2011) 1272.
- [46] A. Kokalj, M. Causà, XCrySDen: (X-Window) CRYstalline Structures and DENsities, 2001.
- [47] BURAI 1.3, A GUI of QUANTUM ESPRESSO code. <https://github.com/BURAI-team/burai>.
- [48] J.P. Perdew, K. Burke, M. Ernzerhof, Generalized gradient approximation made simple, *Phys. Rev. Lett.* 77 (1996) 3865.
- [49] J. Heyd, G.E. Scuseria, M. Ernzerhof, Hybrid functionals based on a screened Coulomb potential, *J. Chem. Phys.* 118 (2003) 8207.
- [50] J. Heyd, G.E. Scuseria, M. Ernzerhof, Erratum: “Hybrid functionals based on a screened Coulomb potential”, *J. Chem. Phys.* 118 (2003) 8207, 124 (2006) 219906.
- [51] S. Grimme, Semiempirical GGA-type density functional constructed with a long-range dispersion correction, *J. Comput. Chem.* 27 (2006) 1787–1799.
- [52] P. Hohenberg, W. Kohn, Inhomogeneous electron gas, *Phys. Rev.* 136 (1964) B864.

- [53] W. Kohn, L.J. Sham, Self-consistent equations including exchange and correlation effects, *Phys. Rev.* 140 (1965) A1133.
- [54] C.G. Broyden, The convergence of a class of double-rank minimization algorithms: 2. The New Algorithm, *IMA J. Appl. Math.* 6 (1970) 222–231.
- [55] R. Fletcher, A new approach to variable metric algorithms, *Comput. J.* 13 (1970) 317.
- [56] D. Goldfarb, A family of variable-metric methods derived by variational means, *Math. Comput.* 24 (1970) 23.
- [57] D.F. Shanno, Conditioning of quasi-Newton methods for function minimization, *Math. Comput.* 24 (1970) 647.
- [58] B. Zhu, L. Zhang, B. Cheng, J. Yu, First-principle calculation study of tri-s-triazine-based g-C₃N₄: a review, *Appl. Catal. B Environ.* 224 (2018) 983.
- [59] J.K. Nørskov, J. Rossmeisl, A. Logadottir, L.R.K.J. Lindqvist, J.R. Kitchin, T. Bligaard, et al., Origin of the overpotential for oxygen reduction at a fuel-cell cathode, *J. Phys. Chem. B* 108 (46) (2004) 17886–17892.
- [60] J. Rossmeisl, A. Logadottir, J.K. Nørskov, Electrolysis of water on (oxidized) metal surfaces, *Chem. Phys.* 319 (1–3) (2005) 178–184.
- [61] G. Gao, Y. Jiao, F. Ma, Y. Jiao, E. Wacławik, A. Du, Metal-free graphitic carbon nitride as mechano-catalyst for hydrogen evolution reaction, *J. Catal.* 332 (2015) 149–155.
- [62] J.K. Nørskov, T. Bligaard, A. Logadottir, J.R. Kitchin, J.G. Hen, S. Pandelov, et al., Trends in the exchange current for hydrogen evolution, *J. Electrochem. Soc.* 152 (3) (2005) J23.
- [63] Y. Zhu, D. Zhang, L. Gong, L. Zhang, Z. Xia, Catalytic activity origin and design principles of graphitic carbon nitride electrocatalysts for hydrogen evolution, *Front. Mater.* 6 (2019) 16.
- [64] M. Huang, Y.L. Zhao, W. Xiong, S.V. Kershaw, Y. Yu, W. Li, et al., Collaborative enhancement of photon harvesting and charge carrier dynamics in carbon nitride photoelectrode, *Appl. Catal. B Environ.* 237 (2018) 783–790.
- [65] M. Ghashghaee, Z. Azizi, M. Ghambarian, Conductivity tuning of charged triazine and heptazine graphitic carbon nitride (g-C₃N₄) quantum dots via nonmetal (B, O, S, P) doping: DFT calculations, *J. Phys. Chem. Solid.* 141 (2020) 109422.
- [66] C. Wan, L. Zhou, L. Sun, L. Xu, D.G. Cheng, F. Chen, et al., Boosting visible-light-driven hydrogen evolution from formic acid over AgPd/2D g-C₃N₄ nanosheets Mott-Schottky photocatalyst, *Chem. Eng. J.* 396 (2020), 125229.
- [67] J. Zhang, X. Chen, K. Takanabe, K. Maeda, K. Domen, J.D. Epping, et al., Synthesis of a carbon nitride structure for visible-light catalysis by copolymerization, *Angew. Chem. Int. Ed.* 49 (2) (2010) 441–444.
- [68] Z. Ma, Z. Yi, J. Sun, K. Wu, Electronic and photo-catalytic properties of Ag₃PC₄VI (C=O, S, Se): a systematic hybrid DFT study, *J. Phys. Chem. C* 116 (2012) 25074–25080.
- [69] K. Ding, B. Chen, Y. Li, Y. Zhang, Z. Chen, Comparative density functional theory study on the electronic and optical properties of BiMO₄ (M=V, Nb, Ta), *J. Mater. Chem.* 2 (2014) 8284–8303.
- [70] R. Kadrekar, N. Patel, A. Arya, Understanding the role of boron and stoichiometric ratio in the catalytic performance of amorphous Co-B catalyst, *Appl. Surf. Sci.* 518 (2020), 146199.
- [71] S. Gupta, N. Patel, R. Fernandes, R. Kadrekar, A. Dashora, A.K. Yadav, et al., Co–Ni–B nanocatalyst for efficient hydrogen evolution reaction in wide pH range, *Appl. Catal. B Environ.* 192 (2016) 126.
- [72] L. Li, W. Wang, H. Liu, X. Liu, Q. Song, S. Ren, First principles calculations of electronic band structure and optical properties of Cr-doped ZnO, *J. Phys. Chem. C* 113 (19) (2009) 8460–8464.
- [73] M.C. Toroker, D.K. Kanan, N. Alidoust, L.Y. Isseroff, P. Liao, E.A. Carter, First principles scheme to evaluate band edge positions in potential transition metal oxide photocatalysts and photoelectrodes, *Phys. Chem. Chem. Phys.* 13 (2011) 16644–16654.
- [74] J. Kang, S. Tongay, J. Zhou, J. Li, J. Wu, Band offsets and heterostructures of two-dimensional semiconductors, *Appl. Phys. Lett.* 102 (2013), 012111.
- [75] W. Chen, A. Pasquarello, Band-edge level in semiconductors and insulators: hybrid density functional theory versus many-body perturbation theory, *Phys. Rev. B* 86 (2012), 035134.
- [76] T.M. Henderson, J. Paier, G.E. Scuseria, Accurate treatment of solids with the HSE screened hybrid, *Phys. Status Solidi B* 248 (4) (2011) 767–774.
- [77] S.M. Aspera, M. David, H. Kasai, First-principles study of the adsorption of water on tri-s-triazine-based graphitic carbon nitride, *Jap. J. Appl. Phys.* 49 (11R) (2010), 115703.
- [78] H. Li, Y. Wu, L. Li, Y. Gong, L. Niu, X. Liu, et al., Adjustable photocatalytic ability of monolayer g-C₃N₄ utilizing single-metal atom: density functional theory, *Appl. Surf. Sci.* 457 (2018) 735.

1 Photocatalyst

Potential Materials for Energy Production and Conversion

B.R. Bhagat and Alpa Dashora

CONTENTS

| | | |
|-------|---|----|
| 1.1 | Introduction..... | 3 |
| 1.2 | Photocatalytic Mechanism..... | 5 |
| 1.2.1 | Hydrogen Evolution Reaction | 7 |
| 1.2.2 | Oxygen Evolution Reaction..... | 8 |
| 1.2.3 | Carbon Dioxide Reduction Reaction | 9 |
| 1.3 | Functionalization Methods for Photocatalytic Activity Enhancement | 11 |
| 1.3.1 | Anionic and Cationic Doping | 11 |
| 1.3.2 | Co-doping | 14 |
| 1.3.3 | Semiconductor Heterostructure and Metallic Co-catalyst..... | 15 |
| 1.4 | Role of Charge Transfer in Enhancing Photocatalytic Activity | 18 |
| 1.5 | Conclusion | 19 |
| | References..... | 19 |

1.1 INTRODUCTION

Nature has been a source of inspiration for human beings from the beginning of time for mimicking and utilizing various advanced techniques of energy production and conversion at a large scale [1–3]. In the current scenario with energy and environmental issues, several techniques for waste management and energy generation at different levels have been developed, but the problem remains intact and is expected to increase our concern in the near future [4]. In order to overcome this issue, a green, sustainable and low-cost methodology is necessary. In this direction, solar energy seems to be the only viable renewable energy source that is consumed and converted by living species in various forms, where photosynthesis is being widely replicated worldwide in the form of artificial photosynthesis for photocatalytic carbon dioxide reduction reaction (CO₂RR) for transformation of high environment pollutant gas (CO₂, NH₃) into fuels such as methanol or methane and for air purification globally by photocatalytic paints and building materials in high-rising architectures [5–13].

This process is also used for hydrogen production with simultaneous oxygen evolution reactions. Photocatalyst has emerged as a cure to paralyzed conventional water treatment methods that had high operating cost along with its ability to cause secondary pollution [14,15]. It has also helped in degradation of industrial dyes and paints released into the water bodies, water purification and water splitting into fuel production by utilizing metal oxides that prevent photo-corrosion. This is now a multifunctional research and development field for the scientific community across the world [16–23].

Various metal oxide semiconductor thin films and nanoparticles have shown a possible solution as an efficient photocatalyst for remediation and as an alternate for the treatment of contaminated water. On the basis of their stability, high quantum yield, suitable band alignment and large reactive surface, TiO_2 [24–26], WO_3 [27–29], ZnO [30–32], CdS [33,34] and ZnS [35–37] have proved and are being used as potential candidates for photocatalytic applications. Having multiple phases and facets with band gap value in ultraviolet range, TiO_2 has received attention as a material with a wide band gap for cationic and anionic impurity accommodation, which creates metastable states between valence band and conduction band for charge separation [38–40]. On the other hand, polymorphic ZnO has performed well because of its high thermal stability and possibility of functionalization in the degradation of organic pollutants. However, the activity in ultraviolet region and high heavy-metal content limit their usage in visible spectrum of light and for treatment of water to be consumed later by living species. To utilize maximum region of visible spectrum, various approaches have been tried, but the heavy-metal ion issue remains the same [41,42].

As a photocatalyst, alternative to metal oxides, the journey of carbon nitride started from its first synthesis as polymeric melon, reported in 1834 by Berzelius and Liebig [43] as one of the oldest synthetic polymers. Later, Liu and Cohen [44] constructed the beta phase by replacing Si from $\beta\text{-Si}_3\text{N}_4$. From 1989 to 1996, carbon nitride was evolved, synthesized and reported as a multifunctional compound with a total of eight polymorphs each having a separate role. $\alpha\text{-C}_3\text{N}_4$, $\beta\text{-C}_3\text{N}_4$, cubic- C_3N_4 , pseudocubic- C_3N_4 and graphitic carbon nitride, which have an s-triazine-based hexagonal structure, s-triazine-based orthorhombic structure and tri-s-triazine-based structure also known as heptazine [45–50], are different allotropes, while tri-s-triazine-based g- C_3N_4 is found to be the most stable structure. g- C_3N_4 structure is a nitrogen heteroatom-substituted graphite framework which includes π -conjugated graphitic planes and sp^2 hybridization of carbon and nitrogen atoms along with numerous photo-reactive and photo-responsive sites. It is a widely known photocatalyst with good visible light absorption, a multi-layered porous structure, great stability and non-toxicity [51–54], but due to high charge carrier (e^- – h^+ pair) recombination tendency, overall photocatalytic efficiency reduces significantly. Many modifications have been included to increase its activity in the visible region of spectrum along with decreasing the rate of recombination of photogenerated charge carriers for enhanced photoactivity [55–58].

This chapter voyages through the functionalization of g- C_3N_4 undertaken to increase its photo-responsive properties in terms of catalysis and presents a comparative study based on various modification strategies. Structural modification of bulk form into nanosheets, nanoflakes, nanotubes and nanoparticles along with modification from planar to corrugated geometry and formation of bi-, tri- and four-layered

stacking has been seen for reducing the recombination rate of photogenerated charge carriers and increasing the reactive surface [59–70]. Cationic and anionic doping is a frequently observed technique to reduce the band gap for higher absorption. Doping of several electron-rich elements has caused the formation of deep trap sites, also called intermediate band for reducing recombination rate of photogenerated e^- – h^+ pair. Nobel metal inclusion shows local surface plasmon resonance enhancing the charge separation leading to higher reactivity.

However, simultaneous reduction–oxidation reaction is difficult to achieve from a single material. Thus, synergistic effects with band mismatch method have been utilized to create a multifunctional catalyst with high absorption by formation of heterostructures via various schemes for efficient charge transfer. At last, this chapter provides deep insight into the development of environmentally friendly carbon nitride photocatalyst as a potential candidate by systematically comparing reported efficiencies based on modification methods and their future scope for charge facilitation over and within layers [71–81].

1.2 PHOTOCATALYTIC MECHANISM

Synergistic effect where photons interact with the photo-responsive material and accelerate the chemical reaction is the prima step of photocatalysis. On absorbing the photon of energy equivalent or greater than band gap of a semiconductor catalyst, electron excites from the valence band (VB) states to the conduction band (CB) states resulting in the formation of a photogenerated electron–hole pair in CB–VB. These charge carriers migrate to the reaction site to participate in the corresponding reaction where the electrons take part in the reduction reaction forming hydrogen molecule, superoxide anions by reducing the ambient oxygen, $HCOO^-$ via carbon dioxide reduction and ammonia production through nitrogen reduction, while holes oxidize adsorbed water molecule in the form of moisture from the atmosphere to generate hydroxyl radicals which are useful for oxygen evolution reaction and dye degradation [82–86]. However, low band gap value, high absorption and large photogenerated electron–hole pair satisfy the essential step for photocatalysis, but reduction–oxidation process depends on band-edge positions of the material. Straddling redox potential is required to provide reduction–oxidation environment to the photocatalyst which includes conduction band minima (CBM) to be higher than the H_2O/H_2 level known as reduction potential (-4.44 eV) and valence band maxima (VBM) to be lower than O_2/H_2O level called oxidation potential (-5.67 eV) against the vacuum potential. Thus, the minimum band gap requirement has to be greater than 1.23 eV for overall water splitting [63,87]. The above process can also be explained with Figure 1.1 in terms of redox potential: band-edge positions like VBM and CBM are determined with respect to normal hydrogen electrode potentials using work function (ϕ) and band gap (E_g) as follows:

$$\text{Conduction band edge } (E_{CB}) = \phi - 4.44\text{ eV} - E_g \quad (1.1)$$

$$\text{Valence band edge } (E_{VB}) = \phi - 4.44\text{ eV} + E_g \quad (1.2)$$

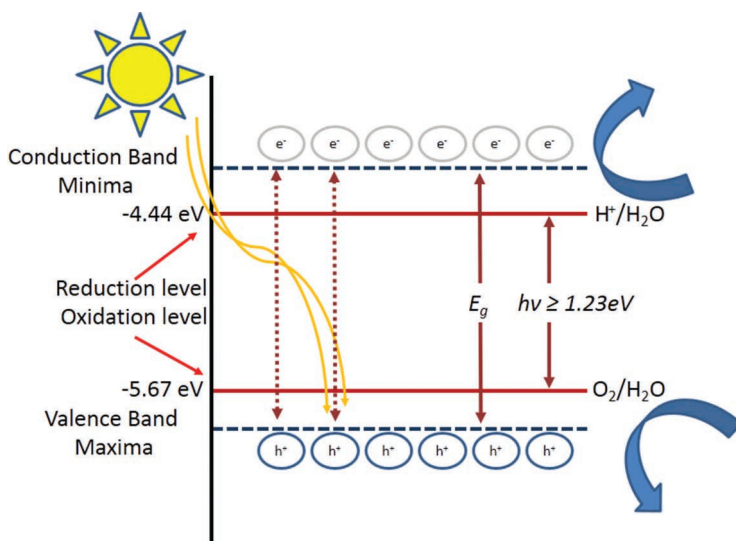


FIGURE 1.1 Photocatalysis mechanism with reduction–oxidation potential and valence–conduction levels. (Energy scale is with respect to vacuum energy.)

For bulk materials, absolute electronegativity (χ) is considered in place of ϕ in Eqs. (1.1) and (1.2). Figure 1.1 shows the schematics of the redox reaction as a part of photocatalytic mechanism. The possibility of a redox reaction is based on the band-edge position, but these band edges are determining the potential for further reaction. Therefore, the potential barrier required for all steps to proceed swiftly should be smaller than the band edges values.

Thus, for the overall water-splitting reaction, four parameters need to be satisfied: (i) high absorption in the visible region, (ii) low charge carrier recombination for high reactivity, (iii) suitable band edges for reduction and oxidation reactions and (iv) reaction energy barrier within the band-edge potential for respective reactions to take place smoothly. The material fulfilling all these four criteria is considered an efficient photocatalyst [88,89]. For the successful screening and validation of above-mentioned criterion for the efficient photocatalyst using first-principles method, a detailed analysis of (i) electronic, (ii) optical and (iii) photocatalytic/thermodynamic properties should be considered as shown in Figure 1.2.

Nowadays, design of an effective photocatalyst using density functional theory (DFT) is one of the most popular, promising, and cost-effective techniques. The required four parameters for efficient photocatalyst can be studied by means of density of states, band structure, ϕ , charge distribution using Löwdin charge transfer and optical property analysis. The number of states present in the system described by the density of states gives the information about the carrier concentration and their energy distribution. Direct and indirect band gap values along with the curvature of the bands are provided by band structure that helps to calculate effective mass (m^*) of the carriers using parabolic fitting method to understand the recombination rate

Steps to Design Novel Photocatalyst

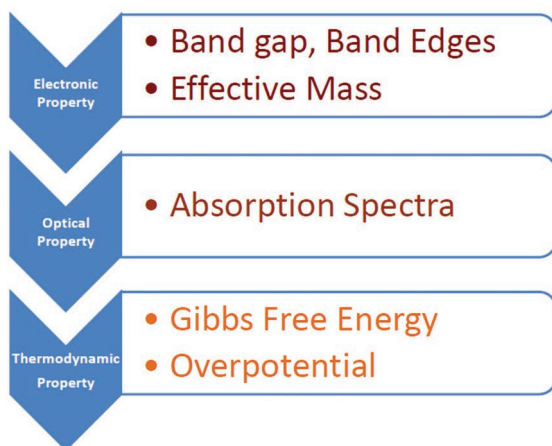


FIGURE 1.2 Stepwise screening methods for efficient photocatalyst.

of electron–hole pair in CBM and VBM. The effective mass of the carrier is defined as follows:

$$m^* = \hbar^2 [(\partial^2 E(k)) / (\partial k^2)]^{-1} \quad (1.3)$$

The mobility of charge carriers and their effective mass exhibit inversely proportional relation as follows:

$$\nu = q\tau/m^* \quad (1.4)$$

Here, ν : mobility of carriers, q : charge carrier and τ : scattering time [90].

The reaction mechanism can also be understood with the help of DFT. The steps of photocatalytic reaction for reduction and oxidation of various molecules are as follows.

1.2.1 HYDROGEN EVOLUTION REACTION

The hydrogen evolution reaction (HER), a part of water-splitting mechanisms, is described by the Volmer–Heyrovsky and Volmer–Tafel reactions shown in Figure 1.3. Volmer–Heyrovsky is energetically more stable than the two-step Volmer–Tafel reaction, where in the former reaction, the electron–hole pair over the substrate (*) forms a hydrogen intermediate (H^*) which converts into a hydrogen molecule on interacting with another pair of charge carrier. The role of the water molecule along with the isolated H^+ is carried out with structural relaxation that describes its interaction and effect on the free energy. Computationally, it includes the formation of hydronium molecule (H_3O) as an intermediate adsorbed over the surface elaborated in the following equations [91,92]:

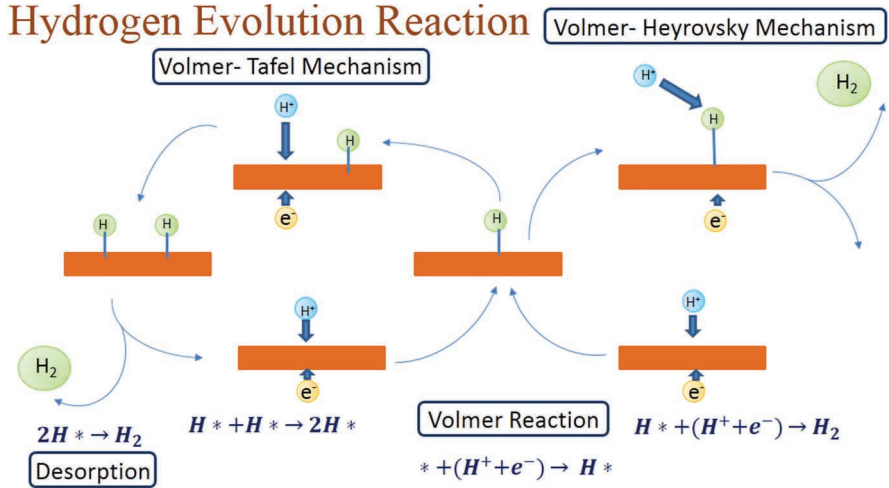
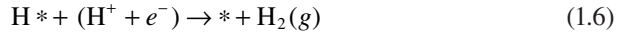
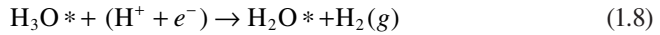
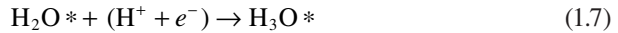


FIGURE 1.3 Hydrogen evolution reaction following the Volmer–Tafel–Heyrovsky mechanism accompanied with desorption.

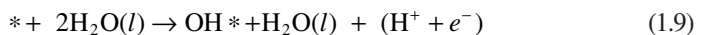


And with inclusion of extra water molecule:



1.2.2 OXYGEN EVOLUTION REACTION

Oxygen evolution reaction (OER) is divided into four one-electron transfer steps as proposed by Rossmeisl et al. [93] and mentioned in Eqs. (1.9–1.12). Here, each step forms an intermediate species (with an asterisk) along with electron–hole pairs, and as the reaction proceeds, there is requirement/involvement of two water molecules for the generation of oxygen molecule releasing a sum of four electrons. OER and HER could simultaneously take place as the released electron–hole pair from the OER can be utilized for generation of two hydrogen molecules. The schematic diagram for OER is also presented in Figure 1.4 for Co–B–C₃N₄ [94].



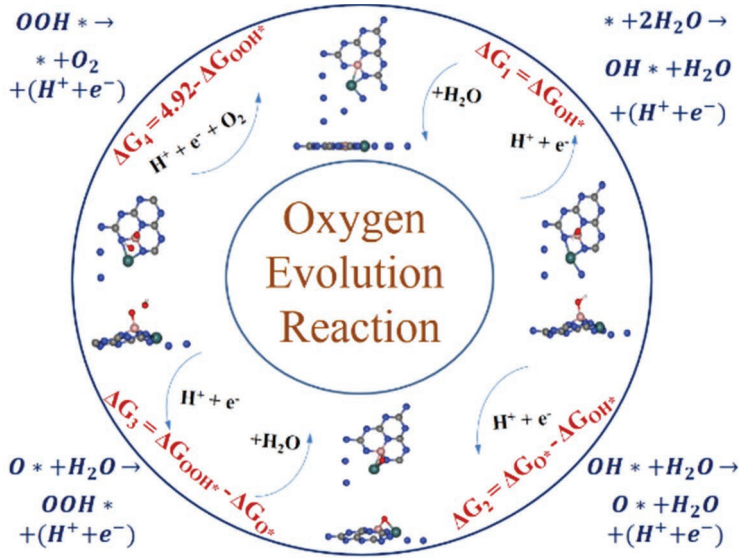
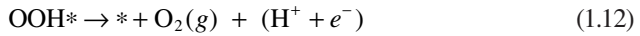
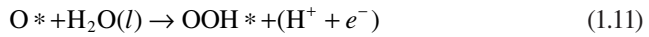
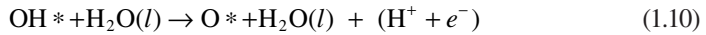


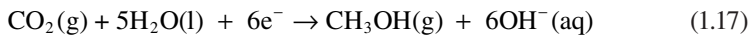
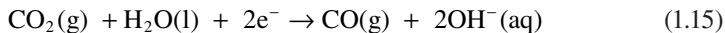
FIGURE 1.4 Four electron step mechanism of oxygen evolution reaction over B-doped-Co-loaded g-C₃N₄ [94].



1.2.3 CARBON DIOXIDE REDUCTION REACTION

Reactions for carbon dioxide reduction involve eight electron steps. There is a possibility of formation of several unstable intermediates apart from that shown in the reactions based on the substrate used. The simultaneous OER and CO₂RR are suitable, leading to the generation of oxygen to carbon dioxide molecule in 2:1 proportion. OER along with HER/CO₂RR is preferred over one-sided reaction since it prevents accumulation of charge carriers over the surface and decreases the possibility of photo-corrosion [6,95]. The following reactions describe the stepwise conversion of carbon dioxide into various forms of fuel:





Change in Gibbs free energy (ΔG) from calculation of energy barrier for each adsorption reaction is evaluated as follows:

$$\Delta G = \Delta E + \Delta \text{ZPE} - T\Delta S + \Delta G_{\text{pH}} + \Delta G_U \quad (1.19)$$

Here, ΔE is the change in the total energy evaluated from the DFT study, ΔZPE is the zero-point energy change, T is the temperature, ΔS is the entropy change, $\Delta G_{\text{pH}} = -k_B T \ln_{10} \times \text{pH}$ and $\Delta G_U = -eU$ (U is the potential measured against normalised hydrogen electrode). The calculation of free energy change in the oxidation/reduction reaction is done using the method developed by Nørskov et al. [96]. The steps that have a maximum change in energy are rate-determining ones. The theoretical value of barrier height for OER is calculated as follows:

$$\eta^{\text{OER}} = \text{Max}_i[\Delta G_i] / ne \quad (1.20)$$

where i denotes intermediate.

The entropy of adsorbed hydrogen atoms is far lower than the entropy in the gas phase (H_2). Since the ZPE and entropy are not sensitive to the coverage, entropy of H_2 gas at standard conditions [92] is used to calculate entropy capacity. Nørskov et al. [96] proposed overall correction to the equation

$$\Delta G_{H^*} = \Delta E_{H^*} + 0.24 \quad (1.21)$$

$$\eta^{\text{HER}} = [\Delta G_{H^*}] / ne \quad (1.22)$$

Photocatalytic energy conversion and dye degradation are measured in terms of quantum yield which is the ratio of reaction rate to the photon absorption rate, although the calculation of absorbed photon energy is difficult due to its scattering. Thus, the efficiency of fuel production is based on its pristine sample or with respect to certain standard material.

The theoretical study of reaction mechanism, adsorption of intermediates, their surface interaction, intermediate interaction among each other and overall effect over the redox capability with the lifetime study of excitons and their role in the inclusion

of van der Waals interaction is still lacking, which plays an important role in the photocatalytic activity as well as enlightens the path for experimentalists to understand the role of catalyst [97,98].

Therefore, the complete theoretical study in terms of photocatalyst performance of any materials should include electronic, optical and thermodynamic (reaction mechanisms). In the next section, the attempts to enhance the photocatalytic activity of $g\text{-C}_3\text{N}_4$ using theoretical and experimental techniques are reviewed.

1.3 FUNCTIONALIZATION METHODS FOR PHOTOCATALYTIC ACTIVITY ENHANCEMENT

In continuation to the current status in the field of photocatalyst for pollutant degradation, CO_2 reduction and H_2 production, it is seen that several modifications such as surface alteration, non-metal and/or metal doping and heterostructures formation have been performed to achieve high photocatalytic activity of different 2D semiconductors. Still there is a bottleneck to accept this technology at a large scale due to low quantum yield and efficiency which is mainly caused due to low charge separation and transportation.

Very few complete theoretical studies are available in this field. Therefore, band gap engineering of functionalized semiconductors for photocatalytic application is the primary technique to enhance the performance.

1.3.1 ANIONIC AND CATIONIC DOPING

Doping in the 2D semiconductor photocatalyst is done in order to enhance the optical performance by narrowing the band gap for higher absorbance in the visible region. Figure 1.5 shows change in band edges for $g\text{-C}_3\text{N}_4$ after different doping. Doping of various non-metal elements has been undertaken on the monolayer of $g\text{-C}_3\text{N}_4$ where band gap alteration for H, B, C, O, F, Si, S, P, Cl, As, Se, Br, Te and I with pristine

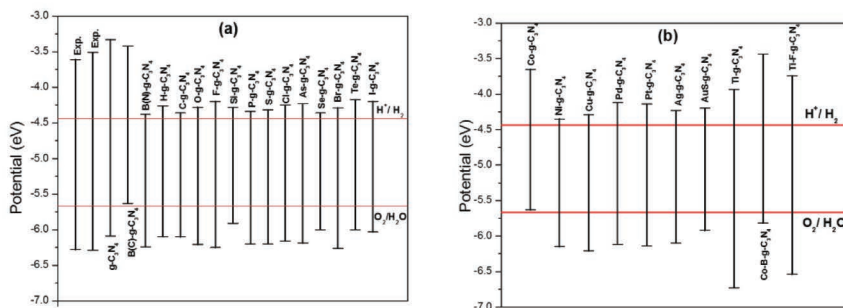


FIGURE 1.5 (a) Band edges for experimental and theoretical pristine and non-metal-doped $g\text{-C}_3\text{N}_4$ [94,99]. (b)s Band edges for metal and anion-cation-doped $g\text{-C}_3\text{N}_4$ (potential vs. vacuum energy) [94,125].

compounds has been studied [99–103]. Among all the anions, Br and I were found unstable thermally due to large positive adsorption energies, while the Fermi energy of all the samples was reduced except that of I-doped monolayer. All reported samples showed higher CBM than reduction potential and lower value than oxidation potential making them suitable for redox ability. HOMO–LUMO position determines the ability to separate the photogenerated charge carriers which directs towards higher photoactivity [99]. S-doped C_3N_4 reduces the Gibbs free energy by 0.28 eV for CO_2 reduction due to promotion of charge separation studied using HOMO–LUMO positioned at N-S atoms and prolongs charge carrier lifetimes by inhibiting the electron–hole recombination [100,101]. A study on the P-doped system emphasized the activation of π -conjugation after the lamellar exfoliation to readily enhance the photo-response [102]. The multiple charge carrier transfers by proton-coupled transfer mechanism and their effective separation show 1.9, 1.4, 1.7 and 2.4-folds high CH_4 production for O-, P-, B-, and S-doped $\text{g-C}_3\text{N}_4$, respectively [103]. Despite limited surface area and photon absorbance of S-doped material, the improvement is subjected to migration and separation of charges. Impurity states formed in the forbidden region have changed the optical absorption along with the obvious redshift after all anionic doping by 10–75 nm [104]. For H-, B-, C-, Si- and Se-integrated ultraviolet region and for all dopants, integrated visible region reduced by 7% and increased by about 14%–71%, respectively. A similar study of S atom or C (N)-vacancy in $\text{g-C}_3\text{N}_4$ has expanded the light response range by decreasing the band gap or by producing impurity states [101,105]. Cui et al. [106] and Zhu et al. [107] have reasoned the charge facilitation to delocalized HOMO–LUMO for improved visible absorption for O- and F-doped tri-s-triazine which also modified the reduction–oxidation potential. So far, the work done on non-metal doping has emphasized on the charge separation and π -localization over the surface for higher reactive sites [108].

Photocatalytic properties are enhanced for Co-doped $\text{g-C}_3\text{N}_4$ due to formation of Co–N bond [109], whereas Fe and Ni penetration into $\text{g-C}_3\text{N}_4$ extends the charge carrier migration distance which suppresses the recombination of electron–hole pairs. On the other hand, Cu and Zn enhance interlayer charge carrier migration [110]. Hussain et al. [111] have designed novel functional nanostructures that are capable of trapping a large number of CO_2 molecules by means of first-principles study. They have functionalized $\text{g-C}_6\text{N}_8$ nanosheets with transition metal (TM) dopant from Sc to Zn, and each TM dopant with a doping concentration of 1.79% can anchor maximum of four CO_2 molecules with suitable adsorption energies (–0.15 to –1.0 eV) for ambient condition applications [111].

Bai et al. [112] have adsorbed alkali metal Li, Na, K, Rb and Cs over the heptazine type $\text{g-C}_3\text{N}_4$ and have seen metallic nature with absorption peak covering visible light area which shows potential application in optoelectronic devices and for visible light catalysis along with sensor detection application due to the charge transfer from alkali metal to substrate leads in decrement of work function as we go down the alkali metal group [112]. Na, K, Rb and Cs have been studied with intercalation between bilayer form of $\text{g-C}_3\text{N}_4$ theoretically and experimentally creating an interlayer bridge for efficient charge transfer and formation of interfacial electric field. K, Rb and Cs decoration increases the oxidation capability

benefiting from a decrease in electronic localization and positive shifted VB position, although Na-doping shows reduced photoactivity due to high rate of recombination [113,114]. A study by Jiang et al. [115] provided 3.7 times increased hydrogen production by Na-doped g-C₃N₄ photocatalyst (18.7 μmol/h) to pristine g-C₃N₄ (5.0 μmol/h) [115]. Electro-positivity and ionic radius direct cations not as a substitutional dopant but as a decoration over the surface on the triazine moieties or in the void. Energetically, high Z cations and noble metal prefer void site over the surface of the 2D structure. A study by Nguyen et al. [116] using semi-empirical tight-binding-based method on the influence of Al, Fe, Ag, Mg and Li doping on corrugated g-C₃N₄ showed lower band gap and reduction in vertical ionization potential that raised electron affinity along with Lewis acidity of pristine specimen attributing to charge transfer from metal to g-C₃N₄. Among single metal-doped g-C₃N₄ system, Fe and Ag atoms' wavefunction participates in the HOMO and C/N atom in LUMO directing towards charge transfer for enhancement of catalytic activity [116]. Rhodamine B degradation rate for Mn adsorbed g-C₃N₄ over different concentrations showed threefold increase in photocatalytic efficiency resulting from the electron-hole recombination, formation of impurity states which leads to increase in optical absorption. For Mn doping of 8.06 at.%, band-edge shifting towards reduction potential takes place which is most suitable for enhanced photoactivity. Density functional theory computation confirms the suitability of Mn among all other 3d TM due to its most suitable band straddling and highest binding energy, while the small potential distance between VB edge and oxidation potential makes hole-H₂O interaction easier [117,118]. Fe doping has been known to activate the low coordinated nitrogen for higher adsorption [119,120], and TM embedding results in the facilitation of light absorption by impurity state formation. A similar experimental study by Tonda et al. [121] on Fe-doped g-C₃N₄ emphasized high charge separation, charge transfer and visible light response providing 7 and 4.5 times increased photocatalytic activity by bulk and nanosheets of pristine specimen. A two-step photo-thermal-catalytic process of H₂ and O₂ generation via 2H₂O → H₂ + H₂O₂, 2H₂O₂ → 2H₂O + O₂ performed over Fe/C₃N₄ shows 1.4 μmol for H₂ and 0.5 μmol of O₂ evolution in 12 hours [121]. The apparent quantum efficiency of oxygen generation is found approximately five times the pristine g-C₃N₄ on studying H₂O₂ disproportionation reaction mechanism [122].

Machine learning study utilizing electronegativity and d-band centre of TM atom helped Zhao et al. [123] to screen single-atom catalysts based on adsorption strength of formic acid. Then, energy barrier of reaction was computed for various transition metals such as Sc, Ti, V, Cr, Mn, Fe, Co, Ni, Zr, Mo, Ru, Rh, Pd, Ag, W, Os, Ir, Pt; among these Au@ g-C₃N₄, Rh-, Pd- and Pt@ g-C₃N₄ exhibit thermodynamical stability and kinetic feasibility and also reported for effective formic acid dehydrogenation catalyst which is beneficial for hydrogen transport and storage. Investigation on single Pt metal atom dispersed over g-C₃N₄ monolayer exhibits anisotropic nature. Meanwhile, its experimental synthesis is possible on considering the density of Pt atom less than that of sixfold cavity, thus avoiding atomic clustering [124]. A complete overall water-splitting study was performed by Li et al. [125] utilizing a single metal atom decorated in planar void site for Pt, Cu, Ni, Pd, Ag and Au based on charge redistribution and

ionic/covalent bond relaxations. Overpotential values showed relationship with conductive bonding nature which is to improve the HER and OER efficiency. Ni, Cu, Pd and Pt show suppression in recombination rate due to separation of VBM and CBM, while overpotential for Pt and Pd with adsorption over the void and TM decreased approximately by four- and threefold for OER and four- and threefold for HER [125]. In spite of band-edge straddling mentioned by single metal catalyst, effective redistribution of HOMO–LUMO altered the barrier height which is an essential step for determination of complete water-splitting ability of photocatalyst.

1.3.2 CO-DOPING

Anionic doping enhances the charge migration and facilitates separation, while cationic doping/decoration increases optical absorption by formation of impurity states and plays a vital role in effective mass tuning which leads to suppression of recombination rate of photogenerated charge carriers along with effective charge compensation. The involvement of CBM and VBM together, which is caused by simultaneous metal/non-metal doping, is predicted highly useful for simultaneous oxidation and reduction reaction. A study performed over co-doped $g\text{-C}_3\text{N}_4$ by Ma et al. [126] on doping of K and S showed positive VB shifting, the opening of charge transfer channel between two triazine moieties, narrowing of band gap, noncoplanar distribution of band edges and increased overpotential value resulting in enhanced OER attributing to separation of electron–hole pair [126]. Efficient approach towards metal-free co-doping in $g\text{-C}_3\text{N}_4$ system leads to the study of S, P co-doped at interstitial and carbon sites by Hu et al. [127] and S, P, O co-doped ultrathin nanosheets by Chu et al. [128] along with Liu et al. [129] have reported increased photocatalytic degradation in the former case and enhanced hydrogen evolution rate reaching $2,480\text{ }\mu\text{mol/h g}$ in the latter case due to suppressed recombination, narrowed forbidden energy change, negative shifting of CB and charge transfer channel formation between heptazine units. Nanosheets synthesized by *in situ* method benefit in the water splitting due to the presence of reactive sites over the large surface area [127–129]. Plasmonic Ag nanoparticle along with B in $g\text{-C}_3\text{N}_4$ increased the activity by 4.2 times which is mainly due to reduction in recombination by charge trap site generation, increased electron mobility and band gap decrement resulting in higher visible region absorption. Therefore, synergetic effect of Ag-B significantly improved the photocatalytic activity compared to mono-doped system [79]. Porous structure, enlarged surface area and interstitial doping of electron-rich Na and P together provided improved charge migration, transfer and mobility due to electron affinity of alkali metal as seen by decreased average lifetime to 5.42 ns indicating emergence of non-radiative charge transfer pathways resulting in efficient photoactivity [130]. In another study where P was co-doped with alkaline earth metal Ba, in $g\text{-C}_3\text{N}_4$ microtubes it exhibits hydrogen evolution up to $12\text{ }\mu\text{mol/h}$ under visible region greater than 420 nm which conforms its 13.2-fold increment to pristine. This increment is attributing to delocalized density of states distribution over HOMO–LUMO and larger surface area for higher photogenerated charge carriers [131]. For the enhancement of photocatalytic activity of tri-s-triazine based $g\text{-C}_3\text{N}_4$, an effective approach of metal (Co) loading and non-metal (B) doping has been considered. On the basis of increment in charge

carrier generation, reduction in recombination rate and charge redistribution over the surface of $g\text{-C}_3\text{N}_4$, two different interaction scenarios (short range and long range) for Co and B were studied and explained. Partial charge compensation along with its conversion into n-type semiconductor with Co-loading and the formation of Co-3d intermediate states while B-doping in $g\text{-C}_3\text{N}_4$ formed p-type semiconductor. In comparison to $g\text{-C}_3\text{N}_4$, all functionalized films have higher visible light absorbance and lower overpotential values for OER, whereas Co- C_3N_4 and co-doped Co-B- C_3N_4 have lower overpotential values for HER [94]. CO_2 reduction utilizing B, K co-doping along with N vacancies has seen photocatalytic production of $3.16\text{ }\mu\text{mol/g}$ CO and $5.93\text{ }\mu\text{mol/g}$ CH_4 , respectively. This high production was achieved using H_2O and CO_2 as feedstocks which are 527% and 161% of CO and CH_4 produced by pristine $g\text{-C}_3\text{N}_4$ without any organic hole scavenger preferring co-doping. This is caused due to the synergistic effect of co-doping over mono-doping which lacks electron donation sites and also the co-doping facilitates CO_2 adsorption over surface [132]. Doping of anion and cation along with the co-doping affects the band edges of the pristine semiconductor which are compiled in wa and b, and it is clearly seen that VB and CB edges are shifted significantly toward the redox potentials.

1.3.3 SEMICONDUCTOR HETEROSTRUCTURE AND METALLIC CO-CATALYST

Considering the points included by the United Nations in sustainable goals for affordable and clean energy accompanied by air purification utilizing natural resources and looking at the current requirement of fuel usage at the world level for transport, industry, power sector and medical applicability, Government of India has also launched the National Hydrogen Mission inviting various industrialists and academicians to collaborate over the design and development of such techniques and for their suitable day-to-day life use. Undergoing the literature, we found that photocatalytic energy conversion displays an attractive pathway to convert earth-abundant molecules (e.g. H_2O , CO_2 , or N_2) into fuels and high-value products (e.g. H_2 , hydrocarbons, oxygenates, or NH_3). The driving force obtained from electron-hole pairs generated in semiconducting materials upon light irradiation is the basis of photocatalysis. Meanwhile, its performance can also be improved by the formation of a cascading junction (Z-scheme) by alignment of same/different material films, hence forming bilayer or heterostructure aimed at enhancing visible light absorption and promoting photogenerated electron-hole separation [133,134]. Formation of heterostructure with narrow band gaps and suitable band-edge positions for utilization of the merit of each component is most viable. Among all three types including Schottky Junction, type II heterojunction and Z-scheme heterojunction as presented in Figure 1.6, type II heterojunction not only provides fast charge transfer route but also suppresses the rapid recombination of electron-hole pairs increasing the photo-conversion efficiency. Due to promotion of charge separation in type II heterojunction by sacrificing charge carriers, a high thermodynamic requirement of CO_2RR makes it unfavourable for feasibility of the reaction mechanism. Natural photosynthesis uses an efficient mode for the transport of photogenerated electrons through a Z-scheme mode [134]. Although type II heterostructure and Z-scheme have similar band structures where one semiconductor suitable for reduction reaction has CB position whereas other

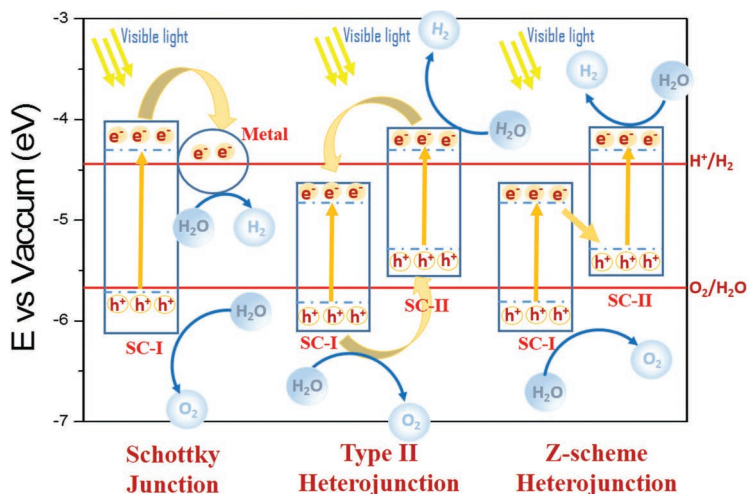


FIGURE 1.6 Charge transfer mechanism in different types of heterojunctions.

semiconductors with low VB position display feasibility for oxidation reaction. When light irradiates on the combination, electrons are excited from VBs to the CBs of both materials and recombination of charge carriers takes place across the interface, thus following a special “Z” shape transport pathway which preserves the pair by strong redox capability, and also the Z-scheme enables wide light response range [135,136].

Numerous works done on various forms of heterojunction have been found which need another chapter to completely review them on the present theme. Thus, the most recent and most efficient heterostructure that plays a critical role in the future of photocatalysis has been considered in this chapter that includes recently developed, synthesized and most popular family of 2D-layered compounds known as MXenes that are both conductors and semiconductors depending on the constituent transition metal and surface functional group. MXenes-based photocatalyst exhibit accelerated charge separation and suppression of carrier recombination [137] as their Fermi level is compatible with that of commonly used wide band gap photocatalysts like ZnO and TiO₂ for the formation of efficient heterojunction. Fermi alignment encourages electron migration to MXene surfaces henceforth formation of Schottky barrier at the interface which prevents electron back-flow on the formation of heterojunction. Therefore, MXenes should be a prime choice as co-catalysts in their metallic form as well as in semiconductor form in formation of Z-scheme for interlayer CB to VB charge transfer and increasing carrier lifetimes for longer reactivity over the surface. It is found that MXenes, especially Sc based such as Sc₂C(OH)₂, are speculated to display high HER photocatalytic activity, attributing to an indirect band gap of around 2.0 eV and CBM above HER theoretical potential making them suitable for Z-scheme semiconductor for the formation of heterostructure with g-C₃N₄ [138]. Ti₃C₂ nanoparticles are highly efficient co-catalyst in H₂ production (14,342 μmol/h g) and have a high quantum efficiency of 40.1% at 420 nm. In addition, they serve efficiently on ZnS or Zn_xCd_{1-x}S [139].

First-principles-based investigation utilizing hybrid functional has been performed for the photocatalytic properties of 2D $g\text{-C}_3\text{N}_4/\text{Ti}_2\text{CO}_2$ van der Waals heterostructure. It falls under the category of type II heterostructure showing band alignment staggering and formation of built-in interfacial electric field due to enhanced charge transfer to Ti_2CO_2 from $g\text{-C}_3\text{N}_4$. High light-harvesting capability, suppression of charge carrier recombination and increased catalytic activity of $g\text{-C}_3\text{N}_4/\text{Ti}_2\text{CO}_2$ towards both HER and OER were demonstrated and reported by reduced overpotential values attributing to the spatially distinguished VB and CB edges, promoting the possibility of direct Z-scheme photocatalytic mechanism [140]. The work done by Liu et al. [141] by fabricating $g\text{-C}_3\text{N}_4/\text{Ti}_3\text{C}_2$ composite resulted in 2.75 times greater photocurrent and enhanced photocatalytic capability of ciprofloxacin degradation as compared to $g\text{-C}_3\text{N}_4$. By varying the mixed ratio of $g\text{-C}_3\text{N}_4$ with Ti_3C_2 and modifying the surface termination groups on the surface of Ti_3C_2 , it was investigated as a co-catalyst in HER. The best HER results were obtained by annealing in the air in a muffle furnace with a high H_2 production of $88\text{ }\mu\text{mol/h g}$ for $g\text{-C}_3\text{N}_4/\text{Ti}_3\text{C}_2$ in a ratio of 190%. Ling et al. [142] have investigated the HER performance step by step for fully O-terminated MXenes, including 7 bi-metal carbides and 10 mono-metal carbides. In another study, lamellar $g\text{-C}_3\text{N}_4$ on Ti_3C_2 surface synthesized by Li et al. [143] have reported the formation of Schottky barrier for facilitating electron immigration attributing to excellent conductivity of MXene at the interface and gives 6 times higher hydrogen production than pure pristine material [143]. He et al. [144] synthesized $\text{TiO}_2/\text{C}_3\text{N}_4$ (2D/2D) core-shell van der Waals heterojunction and deposited 0D MXene forming S-scheme charge transfer pathway between 2D structure and trapping electrons from C_3N_4 . This study provides multi-junction interface tuning for controlled charge migration and regulating enhanced CO_2RR [144]. Work done on the alkalinized Ti_3C_2 with $g\text{-C}_3\text{N}_4$ decoration attributed to superior electrical conductivity and large Fermi level difference for photo-induced carrier separation for 5.9-fold photocatalytic CO_2RR than pristine $g\text{-C}_3\text{N}_4$ and suggests MXene as low-cost and noble metal-free co-catalyst for photocatalysis [145]. Bai et al. [146] synthesized a Z-scheme $g\text{-C}_3\text{N}_4/\text{Bi}_4\text{O}_5\text{I}_2$ photocatalyst based on good photocatalytic nature of bismuth oxyhalides for CO_2 reduction with I^{3-}/I^- as redox mediators. In the absence of co-catalyst and sacrificial reagent, the optimized $g\text{-C}_3\text{N}_4/\text{Bi}_4\text{O}_5\text{I}_2$ system gave a $45.6\text{ }\mu\text{mol/h g}$ production rate of CO quite high as compared to pristine samples [146]. There are other heterostructures explored both experimentally and theoretically based on $g\text{-C}_3\text{N}_4/\text{ZnO}$ for high activity of CO, $g\text{-C}_3\text{N}_4/\alpha\text{-Fe}_2\text{O}_3$ [147], also the high activity of methane and methanol by $g\text{-C}_3\text{N}_4/\text{Sn}_2\text{S}_3\text{-DETA}$ [148]. Various co-doping strategies in heterojunctions have also been brought forward theoretically and experimentally for enhanced photocatalytic activity promoting the interlayer charge transfer, utilizing interfacial coupling Z-scheme charge migration pathway to decrease the recombination along with formation of charge-trapping sites in the forbidden region in the study of (Cr, B) co-doped $g\text{-C}_3\text{N}_4/\text{BiVO}_4$ Z-scheme heterostructure by Wang et al. [149]. Zhao et al. [150] have investigated the photocatalytic mechanism of (F, Ti) co-doped heptazine/triazine-based $g\text{-C}_3\text{N}_4$ heterostructure using hybrid DFT. They have found narrowing of calculated band gap which is advantageous for absorbing visible spectrum of irradiated light resulting in an obvious red shift of optical absorption edge [150], while in another study, spin-polarized DFT+U method is used to check the photocatalytic

performance of (Cu, N) co-doped $\text{TiO}_2/\text{g-C}_3\text{N}_4$ heterostructure resulting in reduction of band gap as compared to $\text{TiO}_2(1\ 0\ 1)$ surface and induction of impurity states of N and Cu appearing in the band gap region of $\text{TiO}_2/\text{g-C}_3\text{N}_4$ leading to reduction of photon excitation energy [151].

1.4 ROLE OF CHARGE TRANSFER IN ENHANCING PHOTOCATALYTIC ACTIVITY

Charge transfer plays a very important role in understanding the photocatalytic reaction. Apart from the separation of electron–hole pair, transfer of electron from VB to CB, the distribution of charges over the surface and formation of active site for redox reaction is also highly dependent on charge transfer mechanism. Various attempts have been made to explain the formation of charge transfer channel in $\text{g-C}_3\text{N}_4$ after modification by doping, loading and heterostructure formation. It is seen that the overpotential of HER and OER depends on the bonding between intermediates (OH, O, OOH, H_2O and H) and reaction site. More electronegative atom on the surface of the photocatalyst participates more actively in the redox reaction and gives low value of overpotential as compared to the other atoms of the photocatalyst surface [152–155]. In the case of P- and S-doped $\text{g-C}_3\text{N}_4$, a charge transfer channel via the N–S–N–C–N–P pathway is suggested to enhance the photocatalytic activity [127]. In the study of TM doping in $\text{g-C}_3\text{N}_4$, transition metal atom is considered as regulator to adjust the electronegativity of the active site and hence the reduction in overpotential is reported [127]. The charge transfer path by the Co and B doping in $\text{g-C}_3\text{N}_4$ as mentioned in Figure 1.7 and Co-B together through a charge transfer channel as marked by the red arrow from neighbouring N to C and then the most electronegative

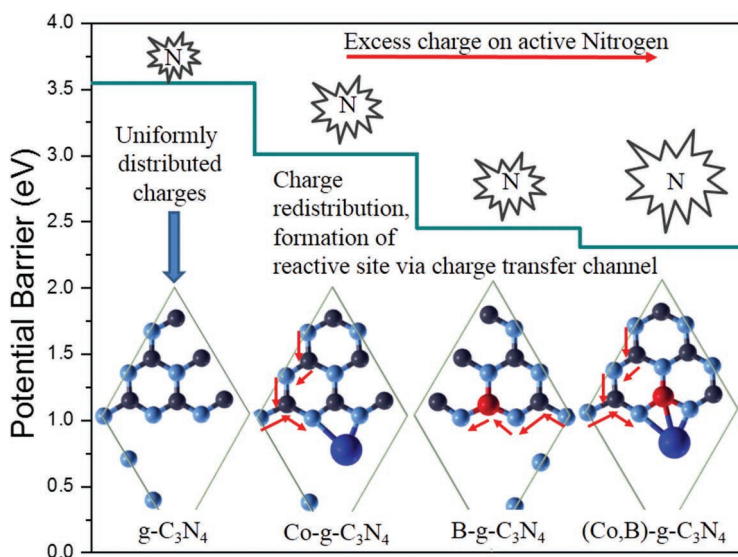


FIGURE 1.7 Role of electronegativity and charge transfer channel in pristine, B-doped, Co-loaded and (Co,B)- $\text{g-C}_3\text{N}_4$ monolayer for decrement of a potential barrier in OER [94].

N [94] make it most suitable for redox reactions with reduction in potential barrier to overcome the prohibitive overpotential [152] as compared to pristine g-C₃N₄.

1.5 CONCLUSION

Carbon nitride is considered as the most popular, stable, low-cost, metal-free photocatalyst under visible light, but due to its high charge carrier recombination, various successful attempts have been made to enhance the photocatalytic efficiency by anion doping, cation doping, anion–cation co-doping, formation of heterostructure, or loading of co-catalyst to form Schottky barrier and heterojunctions as reviewed in this chapter. Effects of various functionalization methods on band edges, optical properties, overall charge distribution on the surface of g-C₃N₄ and effect on overpotential have also been discussed in terms of HER, OER and CO₂RR. For better understanding of optical properties, studies based on excitonic effects are highly required in this field. For better understanding of reaction mechanism, nudged elastic band method is also highly required for functionalized g-C₃N₄ especially to determine the role of charge carrier transfer on adsorption of an intermediate molecule and to have some elaborative insights to reduce the barrier height of rate-determining reaction.

REFERENCES

1. Mao, S. S., & Shen, S. (2013). Catalysing artificial photosynthesis. *Nature Photonics*, 7(12), 944–946.
2. Cox, N., Pantazis, D. A., Neese, F., & Lubitz, W. (2015). Artificial photosynthesis: Understanding water splitting in nature. *Interface Focus*, 5(3), 20150009–20150018.
3. Whang, D. R., & Apaydin, D. H. (2018). Artificial photosynthesis: Learning from nature. *ChemPhotoChem*, 2(3), 148–160.
4. Xu, Y., Li, A., Yao, T., Ma, C., Zhang, X., Shah, J.H., & Han, H. (2017). Strategies for efficient charge separation and transfer in artificial photosynthesis of solar fuels. *Chemistry Sustainability Energy Materials*, 10(22), 4277–4305.
5. Handoko, A. D., Li, K., & Tang, J. (2013). Recent progress in artificial photosynthesis: CO₂ photoreduction to valuable chemicals in a heterogeneous system. *Current Opinion in Chemical Engineering*, 2(2), 200–206.
6. Alotaibi, B., Fan, S., Wang, D., Ye, J., & Mi, Z. (2015). Wafer-level artificial photosynthesis for CO₂ reduction into CH₄ and CO using GaN nanowires. *ACS Catalysis*, 5(9), 5342–5348.
7. Liu, Q., Yuan, J., Gan, Z., Liu, C., Li, J., Liang, Y., & Chen, R. (2020). Photocatalytic N₂ reduction: Uncertainties in the determination of ammonia production. *ACS Sustainable Chemistry Engineering*, 9(1), 560–568.
8. Ren, H., Koshy, P., Chen, W. F., Qi, S., & Sorrell, C. C. (2017). Photocatalytic materials and technologies for air purification. *Journal of Hazardous Materials*, 325, 340–366.
9. Mamaghani, A. H., Haghighat, F., & Lee, C. S. (2017). Photocatalytic oxidation technology for indoor environment air purification: The state-of-the-art. *Applied Catalysis B: Environmental*, 203, 247–269.
10. Shen, W., Zhang, C., Li, Q., Zhang, W., Cao, L., & Ye, J. (2015). Preparation of titanium dioxide nano particle modified photocatalytic self-cleaning concrete. *Journal of Cleaner Production*, 87, 762–765.
11. Hüskén, G., Hunger, M., & Brouwers, H. J. H. (2009). Experimental study of photocatalytic concrete products for air purification. *Building and Environment*, 44(12), 2463–2474.

12. Auvinen, J., & Wirtanen, L. (2008). The influence of photocatalytic interior paints on indoor air quality. *Atmospheric Environment*, 42(18), 4101–4112.
13. Hochmannova, L., & Vytrasova, J. (2010). Photocatalytic and antimicrobial effects of interior paints. *Progress in Organic Coatings*, 67(1), 1–5.
14. Idris, A. M., Liu, T., Shah, J. H., Zhang, X., Ma, C., Malik, A. S., Jin, A., Rasheed, S., Sun, Y., Li, C., & Han, H. (2020). A novel double perovskite oxide semiconductor Sr_2CoWO_6 as bifunctional photocatalyst for photocatalytic oxygen and hydrogen evolution reactions from water under visible light irradiation. *Solar RRL*, 4(3), 1900456–1900466.
15. Idris, A. M., Liu, T., Hussain Shah, J., Han, H., & Li, C. (2020). $\text{Sr}_2\text{CoTaO}_6$ double perovskite oxide as a novel visible-light-absorbing bifunctional photocatalyst for photocatalytic oxygen and hydrogen evolution reactions. *ACS Sustainable Chemistry Engineering*, 8(37), 14190–14197.
16. Abanades, S. (2019). Metal oxides applied to thermochemical water-splitting for hydrogen production using concentrated solar energy. *Chemical Engineering*, 3(3), 63–90.
17. Chen, Y., Feng, X., Liu, Y., Guan, X., Burda, C., & Guo, L. (2020). Metal oxidebased tandem cells for self-biased photoelectrochemical water splitting. *ACS Energy Letters*, 5(3), 844–866.
18. Geiss, O., Cacho, C., Barrero-Moreno, J., & Kotzias, D. (2012). Photocatalytic degradation of organic paint constituents-formation of carbonyls. *Building and Environment*, 48, 107–112.
19. Kandavelu, V., Kastien, H., & Thampi, K. R. (2004). Photocatalytic degradation of isothiazolin-3-ones in water and emulsion paints containing nanocrystalline TiO_2 and ZnO catalysts. *Applied Catalysis B: Environmental*, 48(2), 101–111.
20. Barka, N., Qourzal, S., Assabbane, A., Nounah, A., & Ait-Ichou, Y. (2010). Photocatalytic degradation of an azo reactive dye, Reactive Yellow 84, in water using an industrial titanium dioxide coated media. *Arabian Journal of Chemistry*, 3(4), 279–283.
21. Jain, R., & Shrivastava, M. (2008). Photocatalytic removal of hazardous dye cyanosine from industrial waste using titanium dioxide. *Journal of Hazardous Materials*, 152(1), 216–220.
22. Monga, D., & Basu, S. (2019). Enhanced photocatalytic degradation of industrial dye by g- $\text{C}_3\text{N}_4/\text{TiO}_2$ nanocomposite: Role of shape of TiO_2 . *Advanced Powder Technology*, 30(5), 1089–1098.
23. Mishra, A., Mehta, A., Kainth, S., & Basu, S. (2018). Effect of g- C_3N_4 loading on TiO_2 /Bentonite nanocomposites for efficient heterogeneous photocatalytic degradation of industrial dye under visible light. *Journal of Alloys and Compounds*, 764, 406–415.
24. Akhavan, O., & Ghaderi, E. (2010). Self-accumulated Ag nanoparticles on mesoporous TiO_2 thin film with high bactericidal activities. *Surface and Coatings Technology*, 204(21–22), 3676–3683.
25. Lee, H. S., Im, S. J., Kim, J. H., Kim, H. J., Kim, J. P., & Min, B. R. (2008). Polyamide thin-film nanofiltration membranes containing TiO_2 nanoparticles. *Desalination*, 219(1–3), 48–56.
26. Pal, B., & Sharon, M. (2000). Photodegradation of polyaromatic hydrocarbons over thin film of TiO_2 nanoparticles; a study of intermediate photoproducts. *Journal of Molecular Catalysis A: Chemical*, 160(2), 453–460.
27. Wang, G., Ling, Y., Wang, H., Yang, X., Wang, C., Zhang, J. Z., & Li, Y. (2012). Hydrogen-treated WO_3 nanoflakes show enhanced photostability. *Energy Environmental Science*, 5(3), 6180–6187.
28. Kim, J., Lee, C. W., & Choi, W. (2010). Platinized WO_3 as an environmental photocatalyst that generates OH radicals under visible light. *Environmental Science Technology*, 44(17), 6849–6854.
29. Kwon, Y. T., Song, K. Y., Lee, W. I., Choi, G. J., & Do, Y. R. (2000). Photocatalytic behavior of WO_3 -loaded TiO_2 in an oxidation reaction. *Journal of Catalysis*, 191(1), 192–199.

30. Tian, C., Zhang, Q., Wu, A., Jiang, M., Liang, Z., Jiang, B., & Fu, H. (2012). Cost effective large-scale synthesis of ZnO photocatalyst with excellent performance for dye photodegradation. *Chemical Communications*, 48(23), 2858–2860.
31. Yang, L. Y., Dong, S. Y., Sun, J. H., Feng, J. L., Wu, Q. H., & Sun, S. P. (2010). Microwave-assisted preparation, characterization and photocatalytic properties of a dumbbell-shaped ZnO photocatalyst. *Journal of Hazardous Materials*, 179(1–3), 438–443.
32. Chen, X., Wu, Z., Liu, D., & Gao, Z. (2017). Preparation of ZnO photocatalyst for the efficient and rapid photocatalytic degradation of azo dyes. *Nanoscale Research Letters*, 12(1), 1–10.
33. Cheng, L., Xiang, Q., Liao, Y., & Zhang, H. (2018). CdS-based photocatalysts. *Energy Environmental Science*, 11(6), 1362–1391.
34. Fard, N. E., Fazaali, R., & Ghiasi, R. (2016). Band gap energies and photocatalytic properties of CdS and Ag/CdS nanoparticles for Azo dye degradation. *Chemical Engineering Technology*, 39(1), 149–157.
35. Shah, E., & Soni, H. P. (2013). Inducing chirality on ZnS nanoparticles for asymmetric aldol condensation reactions. *RSC Advances*, 3(38), 17453–17461.
36. Chen, D., Huang, F., Ren, G., Li, D., Zheng, M., Wang, Y., & Lin, Z. (2010). ZnS nano-architectures: Photocatalysis, deactivation and regeneration. *Nanoscale*, 2(10), 2062–2064.
37. Lashgari, H., Boochani, A., Shekaari, A., Solaymani, S., Sartipi, E., & Mendi, R.T. (2016). Electronic and optical properties of 2D graphene-like ZnS: DFT calculations. *Applied Surface Science*, 369, 76–81.
38. Riaz, S., Ashraf, M., Hussain, T., Hussain, M. T., & Younus, A. (2019). Fabrication of robust multifaceted textiles by application of functionalized TiO₂ nanoparticles. *Colloids and Surfaces A: Physicochemical and Engineering Aspects*, 581, 123799–123811.
39. Yuzer, B., Guida, M., Ciner, F., Aktan, B., Aydin, M. I., Meric, S., & Selcuk, H. (2016). A multifaceted aggregation and toxicity assessment study of sol–gel-based TiO₂ nanoparticles during textile wastewater treatment. *Desalination and Water Treatment*, 57(11), 4966–4973.
40. Zhan, X., Luo, Y., Wang, Z., Xiang, Y., Peng, Z., Han, Y., Zhang, H., Chen, R., Zhou, Q., Peng, H., & Huang, H. (2022). Formation of multifaceted nano-groove structure on rutile TiO₂ photoanode for efficient electron-hole separation and water splitting. *Journal of Energy Chemistry*, 65, 19–25.
41. Ma, Y., Wong, C. P., Zeng, X. T., Yu, T., Zhu, Y., & Shen, Z. X. (2009). Pulsed laser deposition of ZnO honeycomb structures on metal catalyst prepatterned Si substrates. *Journal of Physics D: Applied Physics*, 42(6), 065417.
42. Catlow, C. R. A., French, S. A., Sokol, A. A., Al-Sunaidi, A. A., & Woodley, S. M. (2008). Zinc oxide: A case study in contemporary computational solid state chemistry. *Journal of Computational Chemistry*, 29(13), 2234–2249.
43. Liebig, J. V. (1834). About some nitrogen compounds. *Annales Pharmaceutiques Francaises*, 10(10), 10.
44. Liu, A. Y., & Cohen, M. L. (1989). Prediction of new low compressibility solids. *Science*, 245(4920), 841–842.
45. Liu, A. Y., & Wentzcovitch, R. M. (1994). Stability of carbon nitride solids. *Physical Review B*, 50(14), 10362–10365.
46. Teter, D. M., & Hemley, R. J. (1996). Low-compressibility carbon nitrides. *Science*, 271(5245), 53–55.
47. Alves, I., Demazeau, G., Tanguy, B., & Weill, F. (1999). On a new model of the graphitic form of C₃N₄. *Solid State Communications*, 109(11), 697–701.
48. Matar, S. F., & Mattesini, M. (2001). Ab initio search of carbon nitrides, isoelectronic with diamond, likely to lead to new ultra hard materials. *Comptes Rendus de l'Acad'emie des Sciences-Series IIC-Chemistry*, 4(4), 255–272.

49. Komatsu, T. (2001). Prototype carbon nitrides similar to the symmetric triangular form of melon. *Journal of Materials Chemistry*, 11(3), 802–803.
50. Xu, Y., & Gao, S. P. (2012). Band gap of C_3N_4 in the GW approximation. *International Journal of Hydrogen Energy*, 37(15), 11072–11080.
51. Kroke, E., Schwarz, M., Horath-Bordon, E., Kroll, P., Noll, B., & Norman, A. D. (2002). Tri-s-triazine derivatives. Part I. From trichloro-tri-s-triazine to graphitic C_3N_4 structures. *New Journal of Chemistry*, 26(5), 508–512.
52. Nabok, D., Puschnig, P., & Ambrosch-Draxl, C., (2008). Cohesive and surface energies of π -conjugated organic molecular crystals: A first-principles study. *Physical Review B*, 77(24), 245316–245319.
53. Inada, Y., Amaya, T., Shimizu, Y., Saeki, A., Otsuka, T., Tsuji, R., Seki, S., & Hirao, T. (2013). Nitrogen-doped graphitic carbon synthesized by laser annealing of Sumanenemone Imine as a bowl-shaped π -conjugated molecule. *Chemistry–An Asian Journal*, 8(11), 2569–2574.
54. Xia, P., Cheng, B., Jiang, J., & Tang, H. (2019). Localized π -conjugated structure and EPR investigation of g- C_3N_4 photocatalyst. *Applied Surface Science*, 487, 335–342.
55. Raza, W., Bahnemann, D., & Muneer, M. (2017). Efficient visible light driven, mesoporous graphitic carbon nitride based hybrid nanocomposite: With superior photocatalytic activity for degradation of organic pollutant in aqueous phase. *Journal of Photochemistry and Photobiology A: Chemistry*, 342, 102–115.
56. Chen, F., Yang, Q., Wang, Y., Zhao, J., Wang, D., Li, X., Guo, Z., Wang, H., Deng, Y., Niu, C., & Zeng, G. (2017). Novel ternary heterojunction photocatalyst of Ag nanoparticles and g- C_3N_4 nanosheets co-modified $BiVO_4$ for wider spectrum visible-light photocatalytic degradation of refractory pollutant. *Applied Catalysis B: Environmental*, 205, 133–147.
57. Tuna, O., & Simsek, E. B. (2020). Synergic contribution of intercalation and electronic modification of g- C_3N_4 for an efficient visible light-driven catalyst for tetracycline degradation. *Journal of Environmental Chemical Engineering*, 8(5), 104445–104455.
58. Jiang, L. L., Wang, Z. K., Li, M., Zhang, C. C., Ye, Q. Q., Hu, K. H., Lu, D. Z., Fang, P. F., & Liao, L. S. (2018). Passivated perovskite crystallization via g- C_3N_4 for high-performance solar cells. *Advanced Functional Materials*, 28(7), 1705875.
59. Zhang, X., Wang, H., Wang, H., Zhang, Q., Xie, J., Tian, Y., Wang, J., & Xie, Y. (2014). Single-layered graphitic- C_3N_4 quantum dots for two-photon fluorescence imaging of cellular nucleus. *Advanced Materials*, 26(26), 4438–4443.
60. Sun, B., Lu, N., Su, Y., Yu, H., Meng, X., & Gao, Z. (2017). Decoration of TiO_2 nanotube arrays by graphitic- C_3N_4 quantum dots with improved photoelectrocatalytic performance. *Applied Surface Science*, 394, 479–487.
61. Su, Y., Sun, B., Chen, S., Yu, H., & Liu, J. (2017). Fabrication of graphitic- C_3N_4 quantum dots coated silicon nanowire array as a photoelectrode for vigorous degradation of 4-chlorophenol. *RSC Advances*, 7(24), 14832–14836.
62. Zhao, Y., Zhao, F., Wang, X., Xu, C., Zhang, Z., Shi, G., & Qu, L. (2014). Graphitic carbon nitride nanoribbons: Graphene-assisted formation and synergic function for highly efficient hydrogen evolution. *Angewandte Chemie International Edition*, 53(50), 13934–13939.
63. Tahir, M., Cao, C., Mahmood, N., Butt, F. K., Mahmood, A., Idrees, F., Hussain, S., Tanveer, M., Ali, Z., & Aslam, I. (2014). Multifunctional g- C_3N_4 nanofibers: A template-free fabrication and enhanced optical, electrochemical, and photocatalyst properties. *ACS Applied Materials Interfaces*, 6(2), 1258–1265.
64. Wang, S., Li, C., Wang, T., Zhang, P., Li, A., & Gong, J. (2014). Controllable synthesis of nanotube-type graphitic C_3N_4 and their visible-light photocatalytic and fluorescent properties. *Journal of Materials Chemistry A*, 2(9), 2885–2890.

65. Wang, Y., Wang, H., Chen, F., Cao, F., Zhao, X., Meng, S., & Cui, Y. (2017). Facile synthesis of oxygen doped carbon nitride hollow microsphere for photocatalysis. *Applied Catalysis B: Environmental*, 206, 417–425.
66. Sun, J., Zhang, J., Zhang, M., Antonietti, M., Fu, X., & Wang, X. (2012). Bioinspired hollow semiconductor nanospheres as photosynthetic nanoparticles. *Nature Communications*, 3(1), 1–7.
67. Feng, L. L., Zou, Y., Li, C., Gao, S., Zhou, L. J., Sun, Q., Fan, M., Wang, H., Wang, D., Li, G. D., & Zou, X. (2014). Nanoporous sulfur-doped graphitic carbon nitride micro-rods: A durable catalyst for visible-light-driven H_2 evolution. *International Journal of Hydrogen Energy*, 39(28), 15373–15379.
68. You, Z., Su, Y., Yu, Y., Wang, H., Qin, T., Zhang, F., Shen, Q., & Yang, H. (2017). Preparation of g- C_3N_4 nanorod/ $InVO_4$ hollow sphere composite with enhanced visible-light photocatalytic activities. *Applied Catalysis B: Environmental*, 213, 127–135.
69. Tahir, B., Tahir, M., & Amin, N. A. S. (2017). Photo-induced CO_2 reduction by CH_4/H_2O to fuels over Cu-modified g- C_3N_4 nanorods under simulated solar energy. *Applied Surface Science*, 419, 875–885.
70. Tahir, M., Cao, C., Butt, F. K., Butt, S., Idrees, F., Ali, Z., Aslam, I., Tanveer, M., Mahmood, A., & Mahmood, N. (2014). Large scale production of novel g- C_3N_4 micro strings with high surface area and versatile photodegradation ability. *CrystEngComm*, 16(9), 1825–1830.
71. Narkbuakaew, T., & Sujaridworakun, P. (2020). Synthesis of Tri-S-triazine based g- C_3N_4 photocatalyst for cationic rhodamine B degradation under visible light. *Topics in Catalysis*, 63(11), 1086–1096.
72. Ravichandran, D., Akilan, R., Vinnarasi, S., Shankar, R., & Manickam, S. (2021). Tuning the reactivity of tri-s-triazine, trinitro-tri-s-triazine and ternary tri-s-triazine graphitic C_3N_4 quantum dots through H-functionalized and B-doped complexes: A density functional study. *Chemosphere*, 272, 129901–129910.
73. Zhu, B., Zhang, J., Jiang, C., Cheng, B., & Yu, J. (2017). First principle investigation of halogen-doped monolayer g- C_3N_4 photocatalyst. *Applied Catalysis B: Environmental*, 207, 27–34.
74. Devthade, V., Kulhari, D., & Umare, S. S. (2018). Role of precursors on photocatalytic behavior of graphitic carbon nitride. *Materials Today: Proceedings*, 5(3), 9203–9210.
75. Thorat, N., Borade, S., Varma, R., Yadav, A., Gupta, S., Fernandes, R., Sarawade, P., Bhanage, B. M., & Patel, N. (2021). High surface area Nanoflakes of P- g- C_3N_4 photocatalyst loaded with Ag nanoparticle with intraplanar and interplanar charge separation for environmental remediation. *Journal of Photochemistry and Photobiology A: Chemistry*, 408, 113098–113109.
76. Varma, R., Chaurasia, S., Patel, N., & Bhanage, B. M., 2020. Interplay of adsorption, photo-absorption, electronic structure and charge carrier dynamics on visible light driven photocatalytic activity of Bi_2MoO_6/rGO (0D/2D) heterojunction. *Journal of Environmental Chemical Engineering*, 8(6), 104551.
77. Gupta, S., Patel, M.K., Miotello, A., & Patel, N. (2020). Metal boride-based catalysts for electrochemical water-splitting: A review. *Advanced Functional Materials*, 30(1), 1906481–1906508.
78. Roselin, L. S., Patel, N., & Khayyat, S. A. (2019). Codoped g- C_3N_4 nanosheet for degradation of organic pollutants from oily wastewater. *Applied Surface Science*, 494, 952–958.
79. Thorat, N., Yadav, A., Yadav, M., Gupta, S., Varma, R., Pillai, S., Fernandes, R., Patel, M., & Patel, N. (2019). Ag loaded B-doped-g- C_3N_4 nanosheet with efficient properties for photocatalysis. *Journal of Environmental Management*, 247, 57–66.

80. Jaiswal, R., Patel, N., Dashora, A., Fernandes, R., Yadav, M., Edla, R., Varma, R. S., Kothari, D. C., Ahuja, B. L., & Miotello, A. (2016). Efficient Co-B-codoped TiO₂ photocatalyst for degradation of organic water pollutant under visible light. *Applied Catalysis B: Environmental*, 183, 242–253.
81. Patel, N., Dashora, A., Jaiswal, R., Fernandes, R., Yadav, M., Kothari, D. C., Ahuja, B. L., & Miotello, A. (2015). Experimental and theoretical investigations on the activity and stability of substitutional and interstitial boron in TiO₂ photocatalyst. *The Journal of Physical Chemistry C*, 119(32), 18581–18590.
82. Zhao, Z., & Liu, Q. (2007). Mechanism of higher photocatalytic activity of anatase TiO₂ doped with nitrogen under visible-light irradiation from density functional theory calculation. *Journal of Physics D: Applied Physics*, 41(2), 025105.
83. Yang, J., Wang, D., Zhou, X., & Li, C. (2013). A theoretical study on the mechanism of photocatalytic oxygen evolution on BiVO₄ in aqueous solution. *Chemistry*, 19(4), 1320–1326.
84. Fu, C.F., Wu, X., & Yang, J. (2018). Material design for photocatalytic water splitting from a theoretical perspective. *Advanced Materials*, 30(48), 1802106–1802116.
85. Pang, R., Yu, L. J., Wu, D. Y., Mao, B. W., & Tian, Z. Q. (2013). Surface electron–hydrogen ion-pair bound to silver and gold cathodes: A density functional theoretical study of photocatalytic hydrogen evolution reaction. *Electrochimica Acta*, 101, 272–278.
86. Yu, K. M. K., Curcic, I., Gabriel, J., & Tsang, S. C. E. (2008). Recent advances in CO₂ capture and utilization. *Chemistry Sustainability Energy Materials*, 1(11), 893–899.
87. Takanabe, K. (2017). Photocatalytic water splitting: Quantitative approaches toward photocatalyst by design. *ACS Catalysis*, 7(11), 8006–8022.
88. Kamat, P. V. (2012). Manipulation of charge transfer across semiconductor interface. A criterion that cannot be ignored in photocatalyst design. *The Journal of Physical Chemistry Letters*, 3(5), 663–672.
89. Acar, C., Dincer, I., & Zamfirescu, C. (2014). A review on selected heterogeneous photocatalysts for hydrogen production. *International Journal of Energy Research*, 38(15), 1903–1920.
90. Ding, K., Chen, B., Li, Y., Zhang, Y., & Chen, Z. (2014). Comparative density functional theory study on the electronic and optical properties of BiMO₄ (M= V, Nb, Ta). *Journal of Materials Chemistry A*, 2(22), 8294–8303.
91. Nørskov, J. K., Bligaard, T., Logadottir, A., Kitchin, J. R., Chen, J. G., Pandelov, S., & Stimming, U. (2005). Trends in the exchange current for hydrogen evolution. *Journal of the Electrochemical Society*, 152(3), J23.
92. Gao, G., Jiao, Y., Ma, F., Jiao, Y., Waclawik, E., & Du, A. (2015). Metal-free graphitic carbon nitride as mechano-catalyst for hydrogen evolution reaction. *Journal of Catalysis*, 332, 149–155.
93. Rossmeisl, J., Logadottir, A., & Nørskov, J. K. (2005). Electrolysis of water on (oxidized) metal surfaces. *Chemical Physics*, 319(1–3), 178–184.
94. Bhagat, B.R., & Dashora, A. (2021). Understanding the synergistic effect of Co loading and B-doping in g-C₃N₄ for enhanced photocatalytic activity for overall solar water splitting. *Carbon*, 178, 666–677.
95. Lingampalli, S. R., Ayyub, M. M., & Rao, C. N. R. (2017). Recent progress in the photocatalytic reduction of carbon dioxide. *ACS Omega*, 2(6), 2740–2748.
96. Nørskov, J. K., Rossmeisl, J., Logadottir, A., Lindqvist, L. R. K. J., Kitchin, J. R., Bligaard, T., & Jonsson, H. (2004). Origin of the overpotential for oxygen reduction at a fuel-cell cathode. *The Journal of Physical Chemistry B*, 108(46), 17886–17892.
97. Hernández-Alonso, M. D., Fresno, F., Suárez, S., & Coronado, J. M. (2009). Development of alternative photocatalysts to TiO₂: Challenges and opportunities. *Energy Environmental Science*, 2(12), 1231–1257.

98. Mills, A., & Le Hunte, S. (1997). An overview of semiconductor photocatalysis. *Journal of Photochemistry and Photobiology A: Chemistry*, 108(1), 1–35.
99. Lu, S., Li, C., Li, H. H., Zhao, Y. F., Gong, Y. Y., Niu, L. Y., Liu, X. J., & Wang, T. (2017). The effects of nonmetal dopants on the electronic, optical and chemical performances of monolayer g-C₃N₄ by first-principles study. *Applied Surface Science*, 392, 966–974.
100. Ling, F., Li, W., & Ye, L. (2019). The synergistic effect of non-metal doping or defect engineering and interface coupling on the photocatalytic property of g-C₃N₄: First-principle investigations. *Applied Surface Science*, 473, 386–392.
101. Wang, Y., Tian, Y., Yan, L., & Su, Z. (2018). DFT study on sulfur-doped g-C₃N₄ nanosheets as a photocatalyst for CO₂ reduction reaction. *The Journal of Physical Chemistry C*, 122(14), 7712–7719.
102. Zhu, Y. P., Ren, T. Z., & Yuan, Z. Y. (2015). Mesoporous phosphorus-doped g-C₃N₄ nanostructured flowers with superior photocatalytic hydrogen evolution performance. *ACS Applied Materials Interfaces*, 7(30), 16850–16856.
103. Arumugam, M., Tahir, M., & Praserttham, P. (2022). Effect of nonmetals (B, O, P, and S) doped with porous g-C₃N₄ for improved electron transfer towards photocatalytic CO₂ reduction with water into CH₄. *Chemosphere*, 286, 131765–131775.
104. Lu, S., Chen, Z.W., Li, C., Li, H. H., Zhao, Y. F., Gong, Y. Y., Niu, L. Y., Liu, X. J., Wang, T., & Sun, C. Q. (2016). Adjustable electronic performances and redox ability of a g-C₃N₄ monolayer by adsorbing nonmetal solute ions: A first principles study. *Journal of Materials Chemistry A*, 4(38), 14827–14838.
105. Kong, L., Mu, X., Fan, X., Li, R., Zhang, Y., Song, P., Ma, F., & Sun, M. (2018). Site-selected N vacancy of g-C₃N₄ for photocatalysis and physical mechanism. *Applied Materials Today*, 13, 329–338.
106. Cui, J., Liang, S., Wang, X., & Zhang, J. (2015). First principle modelling of oxygen doped monolayer graphitic carbon nitride. *Materials Chemistry and Physics*, 161, 194–200.
107. Zhu, B., Zhang, J., Jiang, C., Cheng, B., & Yu, J. (2017). First principle investigation of halogen-doped monolayer g-C₃N₄ photocatalyst. *Applied Catalysis B: Environmental*, 207, 27–34.
108. Luo, Y., Wang, J., Yu, S., Cao, Y., Ma, K., Pu, Y., Zou, W., Tang, C., Gao, F., & Dong, L. (2018). Nonmetal element doped g-C₃N₄ with enhanced H₂ evolution under visible light irradiation. *Journal of Materials Research*, 33(9), 1268–1278.
109. Zhu, Z., Tang, X., Wang, T., Fan, W., Liu, Z., Li, C., Huo, P., & Yan, Y. (2019). Insight into the effect of co-doped to the photocatalytic performance and electronic structure of g-C₃N₄ by first principle. *Applied Catalysis B: Environmental*, 241, 319–328.
110. Tong, T., He, B., Zhu, B., Cheng, B., & Zhang, L. (2018). First-principle investigation on charge carrier transfer in transition-metal single atoms loaded g-C₃N₄. *Applied Surface Science*, 459, 385–392.
111. Hussain, T., Vovusha, H., Kaewmaraya, T., Karton, A., Amornkitbamrung, V., & Ahuja, R. (2018). Graphitic carbon nitride nano sheets functionalized with selected transition metal dopants: An efficient way to store CO₂. *Nanotechnology*, 29(41), 415502–415600.
112. Bai, K., Cui, Z., Li, E., Ding, Y., Zheng, J., Zheng, Y., & Liu, C. (2020). Adsorption of alkali metals on graphitic carbon nitride: A first-principles study. *Modern Physics Letters B*, 34(32), 2050361–2050372.
113. Li, J., Cui, W., Sun, Y., Chu, Y., Cen, W., & Dong, F. (2017). Directional electron delivery via a vertical channel between g-C₃N₄ layers promotes photocatalytic efficiency. *Journal of Materials Chemistry A*, 5(19), 9358–9364.

114. Xiong, T., Cen, W., Zhang, Y., & Dong, F. (2016). Bridging the g-C₃N₄ interlayers for enhanced photocatalysis. *ACS Catalysis*, 6(4), 2462–2472.
115. Jiang, J., Cao, S., Hu, C., & Chen, C. (2017). A comparison study of alkali metal doped g-C₃N₄ for visible-light photocatalytic hydrogen evolution. *Chinese Journal of Catalysis*, 38(12), 1981–1989.
116. Nguyen, T. T. H., Le, M. C., & Ha, N. N. (2021). Understanding the influence of single metal (Li, Mg, Al, Fe, Ag) doping on the electronic and optical properties of g-C₃N₄: A theoretical study. *Molecular Simulation*, 47(1), 10–17.
117. Zhang, W., Cho, H. Y., Zhang, Z., Yang, W., Kim, K. K., & Zhang, F. (2016). First-principles calculation the electronic structure and the optical properties of Mn decorated g-C₃N₄ for photocatalytic applications. *Journal of the Korean Physical Society*, 69(9), 1445–1449.
118. Zhang, W., Zhang, Z., Kwon, S., Zhang, F., Stephen, B., Kim, K. K., Jung, R., Kwon, S., Chung, K. B., & Yang, W. (2017). Photocatalytic improvement of Mn adsorbed g-C₃N₄. *Applied Catalysis B: Environmental*, 206, 271–281.
119. Hu, S., Ma, L., You, J., Li, F., Fan, Z., Lu, G., Liu, D., & Gui, J. (2014). Enhanced visible light photocatalytic performance of g-C₃N₄ photocatalysts co-doped with iron and phosphorus. *Applied Surface Science*, 311, 164–171.
120. Hu, J., Zhang, P., An, W., Liu, L., Liang, Y., & Cui, W. (2019). In-situ Fe-doped g-C₃N₄ heterogeneous catalyst via photocatalysis-Fenton reaction with enriched photocatalytic performance for removal of complex wastewater. *Applied Catalysis B: Environmental*, 245, 130–142.
121. Tonda, S., Kumar, S., Kandula, S., & Shanker, V. (2014). Fe-doped and-mediated graphitic carbon nitride nanosheets for enhanced photocatalytic performance under natural sunlight. *Journal of Materials Chemistry A*, 2(19), 6772–6780.
122. Li, Z., Kong, C., & Lu, G. (2016). Visible photocatalytic water splitting and photocatalytic two-electron oxygen formation over Cu-and Fe-doped g-C₃N₄. *The Journal of Physical Chemistry C*, 120, 56–63.
123. Zhao, X., Wang, L., & Pei, Y. (2021). Single metal atom catalyst supported on g-C₃N₄ for formic acid dehydrogenation: A combining density functional theory and machine learning study. *The Journal of Physical Chemistry C*, 125, 22513–22521.
124. Yang, C., Zhao, Z., & Liu, Q. (2021). Mechanistic insight into the dispersion behaviour of single platinum atom on monolayer g-C₃N₄ in single-atom catalysts from density functional theory calculations. *Applied Surface Science*, 566, 150697.
125. Li, H., Wu, Y., Li, L., Gong, Y., Niu, L., Liu, X., Wang, T., Sun, C., & Li, C. (2018). Adjustable photocatalytic ability of monolayer g-C₃N₄ utilizing single-metal atom: Density functional theory. *Applied Surface Science*, 457, 735–744.
126. Ma, Z., Cui, Z., Lv, Y., Sa, R., Wu, K., & Li, Q. (2020). Three-in-one: Opened charge-transfer channel, positively shifted oxidation potential, and enhanced visible light response of g-C₃N₄ photocatalyst through K and S Co-doping. *International Journal of Hydrogen Energy*, 45(7), 4534–4544.
127. Hu, C., Hung, W. Z., Wang, M. S., & Lu, P. J. (2018). Phosphorus and sulphur codoped g-C₃N₄ as an efficient metal-free photocatalyst. *Carbon*, 127, 374–383.
128. Chu, Y. C., Lin, T. J., Lin, Y. R., Chiu, W. L., Nguyen, B. S., & Hu, C. (2020). Influence of P, S, O-Doping on g-C₃N₄ for hydrogel formation and photocatalysis: An experimental and theoretical study. *Carbon*, 169, 338–348.
129. Liu, Q., Shen, J., Yu, X., Yang, X., Liu, W., Yang, J., Tang, H., Xu, H., Li, H., Li, Y., & Xu, J. (2019). Unveiling the origin of boosted photocatalytic hydrogen evolution in simultaneously (S, P, O)-Codoped and exfoliated ultrathin g-C₃N₄ nanosheets. *Applied Catalysis B: Environmental*, 248, 84–94.
130. Cao, S., Huang, Q., Zhu, B., & Yu, J. (2017). Trace-level phosphorus and sodium co-doping of g-C₃N₄ for enhanced photocatalytic H₂ production. *Journal of Power Sources*, 351, 151–159.

131. Long, D., Chen, W., Zheng, S., Rao, X., & Zhang, Y. (2020). Barium-and phosphorus-codoped g-C₃N₄ microtubes with efficient photocatalytic H₂ evolution under visible light irradiation. *Industrial Engineering Chemistry Research*, 59(10), 4549–4556.
132. Wang, J. C., Hou, Y., Feng, F. D., Wang, W. X., Shi, W., Zhang, W., Li, Y., Lou, H., & Cui, C. X. (2021). A recyclable molten-salt synthesis of B and K co-doped g-C₃N₄ for photocatalysis of overall water vapor splitting. *Applied Surface Science*, 537, 148014–148022.
133. Handoko, A. D., Steinmann, S. N., & Seh, Z. W. (2019). Theory-guided materials design: Two-dimensional MXenes in electro-and photocatalysis. *Nanoscale Horizons*, 4(4), 809–827.
134. Low, J., Jiang, C., Cheng, B., Wageh, S., Al-Ghamdi, A. A., & Yu, J. (2017). A review of direct Z-scheme photocatalysts. *Small Methods*, 1(5), 1700080.
135. Jiang, L., Yuan, X., Zeng, G., Liang, J., Wu, Z., & Wang, H. (2018). Construction of an all-solid-state Z-scheme photocatalyst based on graphite carbon nitride and its enhancement to catalytic activity. *Environmental Science: Nano*, 5(3), 599–615.
136. Zhang, W., Mohamed, A. R., & Ong, W. J. (2020). Z-Scheme photocatalytic systems for carbon dioxide reduction: Where are we now? *Angewandte Chemie International Edition*, 59(51), 22894–22915.
137. Sun, Y., Meng, X., Dall'Agnese, Y., Dall'Agnese, C., Duan, S., Gao, Y., Chen, G., & Wang, X. F. (2019). 2D MXenes as co-catalysts in photocatalysis: Synthetic methods. *Nano-Micro Letters*, 11(1), 1–22.
138. Liu, J. H., Kan, X., Amin, B., Gan, L. Y., & Zhao, Y. (2017). Theoretical exploration of the potential applications of Sc-based MXenes. *Physical Chemistry Chemical Physics*, 19(48), 32253–32261.
139. Ran, J., Gao, G., Li, F. T., Ma, T. Y., Du, A., & Qiao, S. Z. (2017). Ti₃C₂ MXene co-catalyst on metal sulfide photo-absorbers for enhanced visible-light photocatalytic hydrogen production. *Nature Communications*, 8(1), 1–10.
140. Liu, X., Kang, W., Qi, L., Zhao, J., Wang, Y., Wang, L., Wang, W., Fang, L., & Zhou, M. (2021). Two-dimensional g-C₃N₄/Ti₂CO₂ heterostructure as a direct Z-scheme photocatalyst for water splitting: A hybrid density functional theory investigation. *Physica E: Low-Dimensional Systems and Nanostructures*, 134, 114872–114878.
141. Liu, N., Lu, N., Su, Y., Wang, P., & Quan, X. (2019). Fabrication of g-C₃N₄/Ti₃C₂ composite and its visible-light photocatalytic capability for ciprofloxacin degradation. *Separation and Purification Technology*, 211, 782–789.
142. Ling, C., Shi, L., Ouyang, Y., & Wang, J. (2016). Searching for highly active catalysts for hydrogen evolution reaction based on O-terminated MXenes through a simple descriptor. *Chemistry of Materials*, 28(24), 9026–9032.
143. Li, J., Zhao, L., Wang, S., Li, J., Wang, G., & Wang, J. (2020). In situ fabrication of 2D/3D g-C₃N₄/Ti₃C₂ (MXene) heterojunction for efficient visible-light photocatalytic hydrogen evolution. *Applied Surface Science*, 515, 145922–145930.
144. He, F., Zhu, B., Cheng, B., Yu, J., Ho, W., & Macyk, W. (2020). 2D/2D/0D TiO₂/g-C₃N₄/Ti₃C₂ MXene composite S-scheme photocatalyst with enhanced CO₂ reduction activity. *Applied Catalysis B: Environmental*, 272, 119006–119017.
145. Tang, Q., Sun, Z., Deng, S., Wang, H., & Wu, Z. (2020). Decorating g-C₃N₄ with alkalized Ti₃C₂ MXene for promoted photocatalytic CO₂ reduction performance. *Journal of Colloid and Interface Science*, 564, 406–417.
146. Bai, Y., Ye, L., Wang, L., Shi, X., Wang, P., Bai, W., & Wong, P. K. (2016). g-C₃N₄/Bi₂O₃I₂ heterojunction with I₃/I redox mediator for enhanced photocatalytic CO₂ conversion. *Applied Catalysis B: Environmental*, 194, 98–104.
147. Jiang, Z., Wan, W., Li, H., Yuan, S., Zhao, H., & Wong, P. K. (2018). A hierarchical Z scheme α -Fe₂O₃/g-C₃N₄ hybrid for enhanced photocatalytic CO₂ reduction. *Advanced Materials*, 30(10), 1706108–1706.

148. Huo, Y., Zhang, J., Dai, K., Li, Q., Lv, J., Zhu, G., & Liang, C. (2019). All-solid state artificial Z-scheme porous g-C₃N₄/Sn₂S₃-DETA heterostructure photocatalyst with enhanced performance in photocatalytic CO₂ reduction. *Applied Catalysis B: Environmental*, 241, 528–538.
149. Wang, Q., Lin, Y., Li, P., Ma, M., Maheskumar, V., Jiang, Z., & Zhang, R. (2021). An efficient Z-scheme (Cr, B) codoped g-C₃N₄/BiVO₄ photocatalyst for water splitting: A hybrid DFT study. *International Journal of Hydrogen Energy*, 46(1), 247–261.
150. Zhao, Y., Lin, Y., Wang, G., Jiang, Z., Zhang, R., & Zhu, C. (2019). Photocatalytic water splitting of (F, Ti) codoped heptazine/triazine based g-C₃N₄ heterostructure: A hybrid DFT study. *Applied Surface Science*, 463, 809–819.
151. Zhao, Y., Lin, Y., Wang, G., Jiang, Z., Zhang, R., & Zhu, C. (2018). Electronic and optical performances of (Cu, N) codoped TiO₂/g-C₃N₄ heterostructure photocatalyst: A spin-polarized DFT+ U study. *Solar Energy*, 162, 306–316.
152. Wirth, J., Neumann, R., Antonietti, M., & Saalfrank, P. (2014). Adsorption and photocatalytic splitting of water on graphitic carbon nitride: A combined first principles and semiempirical study. *Physical Chemistry Chemical Physics*, 16(30), 15917–15926.
153. Pan, J., Wang, P., Wang, P., Yu, Q., Wang, J., Song, C., Zheng, Y., & Li, C. (2021). The photocatalytic overall water splitting hydrogen production of g-C₃N₄/CdS hollow core-shell heterojunction via the HER/OER matching of Pt/MnO_x. *Chemical Engineering Journal*, 405, 126622–126641.
154. Xiang, Q., Li, F., Zhang, D., Liao, Y., & Zhou, H. (2019). Plasma-based surface modification of g-C₃N₄ nanosheets for highly efficient photocatalytic hydrogen evolution. *Applied Surface Science*, 495, 143520–143531.
155. Zhou, X., Zhao, C., Chen, J., & Chen, L. (2021). Influence of B, Zn, and B-Zn doping on electronic structure and optical properties of g-C₃N₄ photocatalyst: A first-principles study. *Results in Physics*, 26, 104338–104351.

See discussions, stats, and author profiles for this publication at: <https://www.researchgate.net/publication/361460815>

Charge Transfer Mediated Hydrogen Evolution Reaction Over Co Loaded g-C₃N₄

Conference Paper · June 2022

CITATIONS

0

READS

62

2 authors:



Brajesh Rajesh Bhagat

The Maharaja Sayajirao University of Baroda

20 PUBLICATIONS 94 CITATIONS

[SEE PROFILE](#)



Alpa Dashora

The Maharaja Sayajirao University of Baroda

98 PUBLICATIONS 1,580 CITATIONS

[SEE PROFILE](#)

Charge Transfer Mediated Hydrogen Evolution Reaction Over Co Loaded g-C₃N₄

B.R. Bhagat^{1*} and Alpa Dashora¹

¹Department of Physics, Faculty of Science, The Maharaja Sayajirao University of Baroda, Vadodara, 390002

*Corresponding author: *bhagatbrajesh1996@gmail.com*

Abstract

Highly photoactive transition metal decorated graphitic carbon nitride (g-C₃N₄) possess greater visible spectra absorption and large photo-generated charge separation attributing to formation of intermediate in narrowed forbidden region. Site dependent study of hydrogen evolution reaction (HER) using adsorption of H-molecule along with water molecule and role of charge transfer mechanism are reported for Co decorated g-C₃N₄ (Co-C₃N₄) using density functional theory. Adsorption of water molecule with H-atom over bay-Carbon (C_b) atom in Co-C₃N₄ shows 5.6, 7.3 and 4.6 fold decrease in overpotential than pristine g-C₃N₄, H-atom adsorbed at C_b and H-atom adsorbed at corner-Carbon (C_c) atom, respectively. Significant change in potential barrier is attributed to π -delocalization and charge transfer among H-atom and the C atom of Co-C₃N₄ for enhanced photocatalytic activity.

Introduction

Current scenario directs us for the design and development of photocatalyst, materials utilizing solar spectrum in visible region for energy conversion and pollutant degradation by increasing the reaction kinetics. Polymorphic and ecofriendly g-C₃N₄ has recently established itself as emerging photocatalyst with high absorption efficiency, lamellar structure for large surface area and wide band gap to accommodate various cationic, anionic and co-ionic functionalization. Increment in reaction sites as modification over the π -conjugated system has been observed to increase lifetime of photo-generated charge carrier [1].

Transition metal is widely utilized for doping and decoration in the tri-s-triazine based g-C₃N₄ and have reported enhancement in the visible absorption region as narrowing of band gap result into the red shift, while formation of intermediate impurity states has reduced the recombination rate along with increasing charge separation as deep trap sites provide metastable state for longer lifetime for charge carriers.

Theoretical and experimental studies performed on Co-doping, Co-loading and Co-embedded heptazine based g-C₃N₄ system showed 3 times higher hydrogen evolution rate than pure, decrease in band gap value upto 0.72 eV with built in electric field for suppression of recombination rate and emphasis on Co (3d)- N (2p) interaction for red shift and improved photoelectric property of g-C₃N₄ [2-4].

Despite extensive research with cation doped g-C₃N₄, thorough study on the role of charge transfer and its impact on rate determining step still lacks.

Methodology

For the present work, Quantum Espresso code was used for structural optimization and study of electronic property using 5X5X1 MP **k** point grid with convergence threshold of 10⁻⁶ Ry and kinetic energy cutoff of 60 Ry. van der Waals (Grimme-D2) corrections are also included for accurate calculations. [5-7].

Results and Discussion

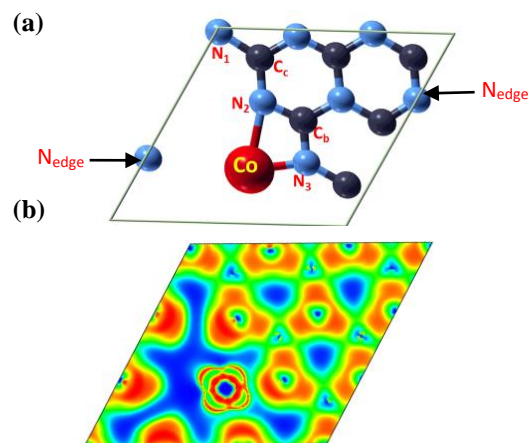


Fig. 1. (a) Optimized Structure and (b) Electron Localization function (ELF) for Co-C₃N₄. In ELF, red-green-blue denotes covalent-metallic-ionic bonding.

Relaxed structure of Co-C₃N₄, as presented in Fig. 1 (a) shows formation of chemical bond between Co-N₂/N₃ explains the decrement of charge on N₂/N₃ from Table 1. while change in C_b/C_c/N₁ signify charge redistribution over the plane, as seen from Fig. 1(b), weak binding for Co-N₂/N₃ activates edge N (N_{edge}) along with delocalization as N-C π -

hybridization is affected due to creation of charge transfer pathway [3].

Volmer-Heyrovsky mechanism for HER directs us for the conversion of electron-proton pair into H_2 molecule through H^* formation which require feasible adsorption-desorption process. Water molecule in vicinity of H provides polar interaction making it electrophilic to maintain weak binding strength. Therefore, it's important to consider different sites for adsorption along with number of H_2O molecule to simulate and study experimental conditions for efficient computation and high quantum yield.

Calculated value of adsorption energy (E_{ads}) for H atom adsorbed on C_b site ($H-C_b$), on C_c site ($H-C_c$), also for H atom with water molecule at C_b site (H_3O-C_b) and same at C_c site (H_3O-C_c) on $Co-C_3N_4$ are -1.23, -0.91, -0.35 and 0.09 eV, respectively. The charge is reduced on the C atom on which H adsorption takes place (C_b and C_c) respect to the corresponding C atom in $Co-C_3N_4$. For H_3O-C_b , after optimization, H atom gets attached to the Co atom while for H_3O-C_c , H atom is attached to the N_{edge} and H_2O molecule drift away. Co-H and Co- N_{edge} interaction result in $0.20e^-$ increment and $0.37e^-$ decrement over H atom affecting adsorption strength of the system. This charge compensation through formed channel is verified by the decrement and increment of $0.4e^-$ and $0.33e^-$ from C_b and N_3 for respective cases.

$$\Delta G_{H^*} = \Delta E_{H^*} + 0.35 \quad a)$$

Using Eq. a), free energy change (ΔG_{H^*}) is calculated and plotted in Fig. 2. The value of ΔG_{H^*} for H_3O-C_b was found to be 0.12 eV to be least while, positive E_{ads} for H_3O-C_c eliminate its occurring probability. Large value for H adsorption in $H-C_b$ and $H-C_c$ is attributed to C_b/C_c -H bonding with $0.16e^-$ charge decrement on H atom and strong binding that would make desorption process endothermic.

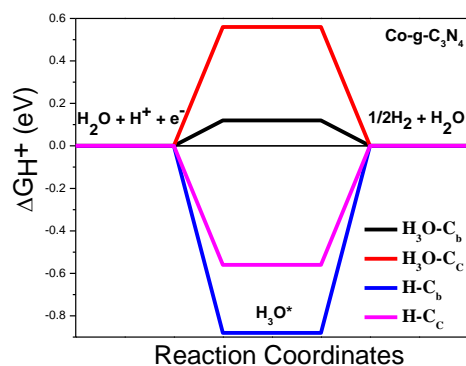


Fig. 2. Gibbs free energy plot for hydrogen evolution reaction with H^* and H_3O^* intermediate.

Table 1. Löwdin charge difference for H and H_3O adsorption .

| | Co | C _b | C _c | N ₁ | N ₂ | N ₃ |
|----------------|------|----------------|----------------|----------------|----------------|----------------|
| Co- C_3N_4 | -.46 | .38 | .31 | -.03 | -.29 | -.27 |
| H- C_b | -.42 | .23 | .38 | -.08 | -.33 | -.31 |
| H- C_c | -.46 | .35 | .23 | -.05 | -.35 | -.30 |
| H_3O - C_b | -.44 | .40 | .39 | -.05 | -.28 | -.23 |
| H_3O - C_c | -.47 | .29 | .32 | -.07 | -.22 | -.33 |

Conclusion

Systematic study of charge migration over the surface for Co decorated g- C_3N_4 is performed along with consideration of electron accumulation centers as adsorption site for isolated hydrogen atom and hydronium molecule as intermediate in hydrogen evolution reaction. Interaction of metal-nitrogen through p_π - d_π coupling, formation of charge transfer channels and activation of multiple sites over the surface is observed.

Further investigation of reduction reaction over bay and corner carbon atom despite their low electronegative nature in the polymeric layer showed strong adsorption that results in reduction of barrier height of reaction. Large electron transfers between H-Co and hydrogen bonding between H_2O - N_{edge} plays crucial role in considering water molecule as necessary requisite for simulating experimental type situation.

Acknowledgement

Authors would acknowledge UGC-Start up grant from financial assistance and AD is grateful to University grants commission, India for financial support under faculty recharge programme.

References

1. T. Tong, B. He, B. Zhu, B. Cheng and L. Zhang, *Appl. Surf. Sci.* **459**, 385-392 (2018).
2. P.W. Chen, K. Li, Y.X. Yu and W.D. Zhang, *Appl. Surf. Sci.* **392**, 608-615 (2017).
3. B.R. Bhagat and A. Dashora, *Carbon*, **178**, 666-677 (2021).
4. Z. Zhu, X. Tang, T. Wang, W. Fan, Z. Liu, C. Li, P. Huo and Y. Yan, *Appl. Catal. B* **241**, 319-328 (2019).
5. J.P. Perdew, K. Burke, M. Ernzerhof, *Phys. Rev. Lett.* **77**, 3865 (1996).
6. S. Grimme, *J. Comput. Chem.* **27**, 1787-1799 (2006).
7. P. Hohenberg, W. Kohn, *Phys. Rev.* **136**, B864 (1964).